

Sub-Micron Nano-Composite CoC Hall Sensors by Focused Electron-Beam Induced Deposition for Microbead Detection

THÈSE N° 4944 (2011)

PRÉSENTÉE LE 25 FÉVRIER 2011

À LA FACULTÉ SCIENCES ET TECHNIQUES DE L'INGÉNIEUR
LABORATOIRE D'OPTIQUE APPLIQUÉE PROF. SALATHÉ
PROGRAMME DOCTORAL EN SCIENCE ET GÉNIE DES MATÉRIAUX

ÉCOLE POLYTECHNIQUE FÉDÉRALE DE LAUSANNE

POUR L'OBTENTION DU GRADE DE DOCTEUR ÈS SCIENCES

PAR

Laurent BERNAU

acceptée sur proposition du jury:

Prof. P. Stadelmann, président du jury
Prof. P. Hoffmann, Dr I. Utke, directeurs de thèse
Prof. J. M. De Teresa, rapporteur
Prof. C. Hagen, rapporteur
Dr R. Wepf, rapporteur



ÉCOLE POLYTECHNIQUE
FÉDÉRALE DE LAUSANNE

Suisse
2011

Résumé

Dans les systèmes intégrés d'analyse biomoléculaire des billes superparamagnétiques de dimension micrométrique sont utilisées comme marqueurs moléculaires. Leur localisation dans des circuits fluidiques intégrés nécessite des capteurs magnétiques de haute précision et de dimensions inférieures au micromètre. La présente thèse a pour objectif l'étude de la réalisation et de la caractérisation de capteurs magnétiques réalisés par déposition induite par faisceau d'électrons focalisé (Focused Electron Beam Induced Deposition, FEBID). Dans cette technique, un faisceau d'électrons finement focalisé est utilisé pour irradier de manière sélective une surface sur laquelle des molécules fonctionnelles ont été adsorbées. La dissociation par impact électronique de ces molécules adsorbées conduit à la déposition à la surface d'un matériau non volatil, tandis que des fragments volatils désorbent et sont pompés vers le vide. Nous avons étudié la déposition induite par faisceau d'électrons focalisé du métal carbonyle $\text{Co}_2(\text{CO})_8$. Le dépôt est constitué d'un matériau nanocomposite CoC, dans lequel des nanocristaux de dimensions 2-3nm sont entourés d'une matrice carbonacée. Ce matériau possède des caractéristiques magnétiques intéressantes, en ce qu'il exhibe un effet Hall extraordinaire (Extraordinary Hall Effect, EHE) augmenté par une dispersion électronique aux interfaces, ce qui lui confère une haute sensibilité au champ magnétique. Cette propriété, alliée à la possibilité de structurer le matériel dans le domaine nanométrique grâce à l'utilisation de faisceaux focalisés fait de ce matériau une option de choix pour la réalisation de capteurs magnétiques de haute résolution et de faible dimension (inférieure au micromètre).

Néanmoins, un contrôle précis de la composition du dépôt est nécessaire, étant admis que la résolution en terme de champ magnétique est hautement dépendante de celle-ci. Nous présentons pour la première fois le contrôle précis de la composition de dépôts obtenus à partir de $\text{Co}_2(\text{CO})_8$ en utilisant la fréquence d'un faisceau d'électrons pulsé en tant que paramètre de contrôle. Cette variation est expliquée par la co-déposition d'hydrocarbonés provenant de la chambre à vide. Un modèle analytique inédit est proposé qui permet

la description du processus de déposition induite par électrons en présence de deux espèces adsorbées. Le modèle analytique permet une prédiction des paramètres permettant une fenêtre de variation compositionnelle large pour tout système de deux espèces adsorbées. Le modèle est appliqué au système composé du complexe $\text{Co}_2(\text{CO})_8$ et d'hydrocarbonés. Nous démontrons qu'il permet une description *quantitative* des variations observées en terme de composition.

Le matériau nanocomposite CoC est étudié et caractérisé en appliquant un modèle de courbe de Langevin au signal Hall. Nous démontrons que cette approche permet l'estimation de la taille moyenne des nanocristaux, ce qui en fait une méthode de nanocaractérisation du matériau. Une relation linéaire entre la résistivité électrique et la résistivité Hall à saturation est démontrée. De manière empirique, une résolution optimisée en terme de champ magnétique est trouvée pour les matériaux présentant une concentration d'environ 65 pc. atomiques de cobalt, ce qui représente un compromis entre une haute sensibilité magnétique et une résistivité électrique suffisante.

Enfin, nous démontrons la détection d'une microbille superparamagnétique en utilisant le capteur magnétique CoC. Grâce à une installation de nanomanipulation inédite, nous démontrons la capacité du capteur à mesurer la distance entre une microbille et le capteur.

Mots clés: Processus par faisceau d'électrons focalisés • effet Hall extraordinaire • matériau nanocomposite • système à deux espèces adsorbées • chimie des surfaces

Abstract

In order to track single superparamagnetic microbeads serving as markers in biomolecular assays, high-sensitivity, sub-micron magnetic sensors which can be integrated onto Lab-on-a-chip platforms are needed. This thesis studies the realization and characterization of such magnetic sensors using Focused Electron Beam Induced Deposition (FEBID) of Cobalt in a High Vacuum (HV) Scanning Electron Microscope (SEM). In FEBID, a finely focused electron beam is used to selectively irradiate a surface where functional precursor molecules are adsorbed. Electron-impact dissociation of the adsorbates lead to non-volatile fragments being deposited at the point of irradiation, while volatile fragments desorb and are pumped away. We have investigated FEBID of Dicobalt octacarbonyl $[\text{Co}_2(\text{CO})_8]$. The deposit consists of a nanocomposite CoC material, where Co nanocrystals 2-3nm in size are embedded in a carbonaceous matrix. This material exhibits a scattering enhanced Extraordinary Hall Effect (EHE) which allows for high magnetic sensitivities. Combined with the inherent nanometric resolution of the deposition process, this makes this nanocomposite CoC material the material of choice for the deposition of small (sub-micron), high-sensitivity magnetic sensors.

However, the magnetic field resolution is found to be highly dependent on the exact composition of the deposition process. We report for the first time the controlled tuning of the composition of deposits from $\text{Co}_2(\text{CO})_8$ using the electron beam pulse time as the process parameter. We explain the tunability in terms of co-deposition of chamber background hydrocarbons. A novel, general model describing the electron-induced deposition in terms of surface adsorbate densities in the presence of two adsorbate species is presented. The analytical model allows to describe the conditions for a broad tunable composition window for any two-adsorbate system. The model is applied to the two-adsorbate system consisting of $\text{Co}_2(\text{CO})_8$ and HV chamber background hydrocarbons and we show that it allows for a *quantitative* description of the compositional variations.

The CoC nanocomposite material is studied and characterized using a

Langevin fit of the Hall signal. We show that this approach yields insight into the nanocrystal mean size, providing a nanocharacterization method of the material. A linear dependency between the electrical resistivity and the Hall resistivity at saturation is found. Empirically, the material is found to exhibit an optimum in terms of magnetic field resolution at around 65at.% Co, corresponding to a trade-off between magnetic field sensitivity and electrical resistivity.

Finally, we demonstrate single superparamagnetic bead detection using a sub-micron, CoC Hall sensor. Using a novel nanomanipulation setup providing a magnetic coil integrated into a SEM, we show the bead tracking capacities of these sensors.

Keywords: Focused Electron Beam Induced Processing (FEBIP) • Extraordinary Hall Effect (EHE) • nanocomposite material • two-adsorbate system • surface chemistry

Acknowledgments

This thesis represents the work of four years of research conducted at the Laboratory for Mechanics of Materials and Nanostructures of the Swiss Federal Laboratory for Materials Science and Technology (EMPA) in Thun. This PhD was supported by funding under the European Commission's 6th Framework Programme, New and Emerging Science and Technologies, Project BioNano-Switch and by partial funding under European Cooperation in Science and Technology (COST).

This PhD was made possible by the support I have received from many people during the last four years. I would like to express my gratitude towards them and apologize to those that I may forget to mention.

First of all, I would like to thank Prof. Patrik Hoffmann, head of the Nanoresearch Group at EPFL and of the Laboratory for Advanced Materials Processing at EMPA, for accepting to become my thesis director and for his guidance. I would like to thank Dr. Johann Michler, head of the Laboratory for Mechanics of Materials and Nanostructures, for giving me the opportunity to work in his laboratory. I'm profoundly indebted to my thesis co-director Dr. Ivo Utke for the quality of the guidance and support he has provided me throughout this PhD thesis, for the trust he has shown and for giving me the feeling that his door was opened whenever I would need scientific or personal advice.

Then, I'm very grateful towards Dr. Mihai Gabureac with whom I had both the chance and the pleasure to collaborate during this time, for sharing his scientific knowledge with me. He has taught me two basic experimental virtues: patience and meticulousness.

I gratefully acknowledge helpful support from Dr. Giovanni Boero from the Microsystem Design Group at EPFL for his help with the magnetic experiments and their interpretation. I would like to thank Prof. Petra Swiderek at the Institute for Applied and Physical Chemistry at the University of Bremen who has received me in her laboratory during a research stay, as well as Dr. Mohamed Nejib Hedhili for the introduction to the HREELS setup and for the group members in Bremen who have been of great support (Jan,

Thorben, Ute, Alena). I thank Prof. Michael Allan of the Department of Chemistry of the University of Fribourg for providing us with the precursor used in the HREELS study and for helpful advice. I am indebted to Dr. Maria-Cristina Timirgaziu and Martin Purrucker for their kind support and informative discussion in the mathematic derivation of the analytical model proposed.

When I started this PhD, several people introduced me to the existing setups at EMPA, allowing me to start my first experiments. I would like to thank my former colleagues Vinzenz Friedli, Samuel Hoffmann, Hiroyuki Miyazoe and Gerhard Bürki for their patient introduction to the world of scanning electron microscopes, FEBID and nanomanipulation. I have enjoyed to be allowed to work with Dr. Nicula Radu and Dr. Manuela Stir on a side project. I gratefully acknowledge Dr. James Whitby and Dr. Chris Bradbury for the scientific and english input they provided while proof-reading our publication manuscripts. I'd like to thank the interns who have participated in this research: Chong, Tiphaine, Adam, Hirokazu, Sandra, Ollie. Several people have provided support in the mechanical lab (Anton Böll), for informatics (Christian Kauer), for the administrative tasks (Katrín Gurtner and Eveline Straubhaar at EMPA, Erika Menamkat at EPFL).

I'd like to thank Laetitia, Simona, Mikhael, Karolina, Martin and Jessica for the cordiality in the offices we've been sharing. They and a lot of people have contributed to the good atmosphere at EMPA which only makes sound scientific work possible. Thank you Adrien, Fred, Kilian, Rejin, Marion, Max, Jamil, Barbara, Bill, Sid, Pierre and all other group members.

I'd like to thank my parents, Monique and Werner Bernau, for their continuous support during my studies and, together with my brother and sister, Vianney and Laetitia, for their encouragement during this PhD project. Finally, I thank Evelyne for being who she is and for her patience and love.

Contents

Résumé	i
Abstract	iii
Acknowledgments	v
1 Introduction	1
1.1 Motivation	1
1.2 Structure and content of the thesis	3
2 Background	5
2.1 Focused electron-beam induced deposition	5
2.1.1 Electron-substrate interactions and principles of FEBID	5
2.1.2 FEBID of Cobalt - literature results	9
2.1.3 FEBID rate model in the presence of a single adsorbate species	16
2.2 Magnetic microsensors for bead sensing	22
2.2.1 Magnetic properties of superparamagnetic microbeads .	22
2.2.2 Magnetic field generated by a microbead	25
2.2.3 Figures of merit for magnetic microsensors used for microbead detection	29
2.2.4 The Hall effect in ferromagnetic materials	32
2.2.5 Magnetic microsensors for single-bead detection	34
3 Experimental setups	39
3.1 Focused particle beam processing and characterisation	39
3.1.1 Electron microscope Hitachi S-3600	39
3.1.2 Gas injection system	41
3.1.3 Tescan dual-beam microscope	44
3.1.4 Electron microscope Hitachi S-4800	44
3.1.5 Atomic force microscope Topometrix Explorer	44

3.2	Lithography	44
3.3	Electrical and magnetic characterisation	46
3.4	Bead detection setup	48
4	Tuning the composition of nano-composite Cobalt-Carbon deposits	53
4.1	Introduction	53
4.2	Experiment	55
4.3	Experimental results	57
4.3.1	Composition	57
4.3.2	Deposition rates	59
4.4	Analytical two-adsorbate model	60
4.4.1	Deposition rates in the two-adsorbate model	60
4.4.2	Composition of the deposit in the two-adsorbate model	65
4.4.3	Application of the model to the experimental system	68
4.4.4	Estimation of molecule parameters using the single-adsorbate model	69
4.4.5	Application of the model to the experimental system	78
4.5	Conclusions	80
5	Magnetic sensing properties	81
5.1	Introduction	81
5.2	Experiment	82
5.3	Hall curve analysis	83
5.3.1	Methodology	83
5.3.2	Saturation field	89
5.3.3	Extraordinary Hall resistivity at saturation	92
5.4	Sensor performance	94
5.5	Conclusion	98
6	Single-bead detection using FEBID Co-C Sensor	99
6.1	Introduction	99
6.2	Experimental setup	100
6.2.1	Sensors and microbeads	100
6.2.2	Magnetic fields	101
6.2.3	Hall signal recovery using Lock-in amplification	102
6.3	Ex-situ single-bead detection	104
6.3.1	Detection scheme	104
6.3.2	Results	105
6.3.3	Discussion	108
6.4	In-situ single-bead detection	113

6.4.1	Detection scheme	113
6.4.2	Results and discussion	115
6.5	Conclusion	118
7	Conclusion	119
7.1	Contributions of this thesis	120
7.2	Future research perspectives	121
A	Thermal decomposition of $\text{Co}_2(\text{CO})_8$ by electron-beam induced heating	123
A.1	Introduction	123
A.2	Experimental results	124
A.3	Heat transfer model	124
A.4	Conclusion	128
B	HREELS study of electron-induced dissociation of Tetrakis-trifluorophosphine platinum ($\text{Pt}(\text{PF}_3)_4$)	129
B.1	Introduction	129
B.2	Tetrakis-trifluorophosphine platinum	130
B.3	Experimental setup	131
B.4	HREEL spectra of unirradiated adsorbates	132
B.4.1	Identification of fundamental modes	132
B.4.2	Assessment of substrate coverage	134
B.4.3	Confirmation of excess PF_3 removal	134
B.5	$\text{Pt}(\text{PF}_3)_4$ dissociation	136
B.6	Conclusions	138
C	Preliminary HREELS study of the electron-induced dissociation of Cobalt-tri(carbonyl)-nitrosyl ($\text{Co}(\text{CO})_3\text{NO}$)	141
C.1	Cobalt-tri(carbonyl)-nitrosyl $\text{Co}(\text{CO})_3\text{NO}$	141
C.2	HREEL spectra of unirradiated adsorbates	142
C.3	$\text{Co}(\text{CO})_3\text{NO}$ dissociation	144
C.4	Conclusions	145
	Bibliography	147
	Nomenclature	165
	List of publications	167
	Curriculum vitae	169

Chapter 1

Introduction

1.1 Motivation

In the last decade of the twentieth century, progress in micro- and nanostructuring techniques has allowed the design and implementation of various single molecule micromanipulation techniques [1–11]. Compared to bulk assays which measure average responses of biophysical processes, single-molecule studies allow measuring individual stochastic processes and gaining knowledge of activity distribution of individual processes [12]. Single-molecule assays rely on the use of polymer beads of micrometric dimensions, both as a marker for the molecule's location and as a force transducer. The use of microbeads exhibiting magnetization under an external field is popular, as it allows manipulation using magnetic field gradients [13].

However, magnetic sensors allowing the read-out of the precise magnetic marker position regardless of the high external magnetic fields in play are required, in order to integrate such assays into lab-on-a-chips platforms. This thesis addresses this issue by reporting successful integration of a sub-micron sized Hall sensor into a microfluidic platform by using local deposition of a novel nanocomposite Co-C material, which exhibits outstanding magnetic flux resolution properties. This opens the possibility to integrate high magnetic flux resolution Hall sensors onto a single platform for parallel read-out of single-molecule assays (see figure 1.1).

The technology used to deposit this high sensitivity material in sub-micron size and varied geometries is the focused electron-beam induced deposition (FEBID) of Cobalt. In FEBID, a volatile compound containing the material to be deposited is adsorbed on a surface and decomposed locally using a highly focused electron-beam, leaving a solid deposit containing the desired material on the surface, whereas the released, volatile chemical lig-

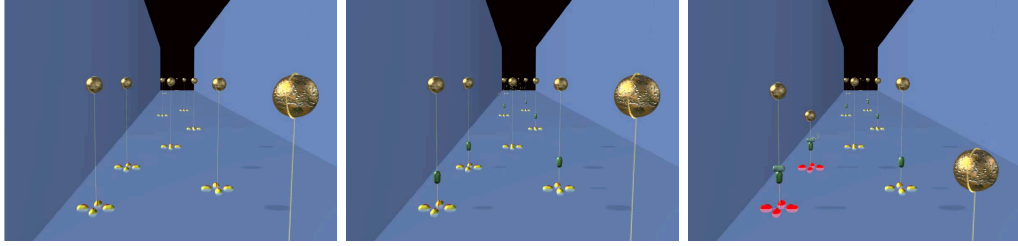


Figure 1.1: *Principle of a microfluidic molecular detector based on a molecular motor. a) DNA strands are fixed on top of micromagnetic sensors in a microfluidic channel. The free ends of the DNA strands are bound to superparamagnetic microbeads. A magnetic field with a field gradient in the vertical direction is used to both magnetize the beads and to provide an upward-directed force to “stretch” the DNA strands. b) A molecular motor (an enzyme known as DNA translocase) is flushed through the microchannel and attaches selectively to the DNA strands. c) The presence of the molecule of interest to be detected activates the molecular motor, initiating the shortening of the DNA strand. This triggered movement brings the superparamagnetic beads closer towards the magnetic sensors at the bottom of the microfluidic channel. The (physical) response of the sensor is used as a signal for the presence of the analyte of interest, thus providing a highly sensitive transducer. Source: [14]*

ands desorb to the vacuum [15–17]. Hence, FEBID represents a minimally invasive, maskless lithography technique, which allows depositing nanometric structures at any location on a given substrate.

This is an asset when it comes to the integration of micromagnetic sensors into microfluidic channels. The ability to deposit the sensor at any location on a 3-D prestructured substrate means that an entire microfluidic platform can be fabricated, including thermal treatment steps that would otherwise be incompatible with the magnetic sensing material, *before* actually carrying out the sensor fabrication step.

Also, it is known that FEBID of metals leads to metallic nanocrystals embedded in a carbonaceous matrix [18, 19]. This represents a novel nanocomposite material with properties outperforming the properties of the bulk material in terms of sensitivity to the magnetic field, as has been suggested in [20]. In this thesis, the properties of this novel, Cobalt:Carbon nanocomposite material are analyzed and discussed in depth.

Hence, FEBID represents the technology of choice for the deposition of submicron-sized structures exhibiting high sensitivity to the magnetic field, provided one is able to control precisely the growth dynamics and the composition of the deposit. Indeed, although FEBID is a well-known technique,

allowing to deposit three-dimensional structures with high precision, the composition of the obtained deposits is often a challenge, either because the deposited material does not exhibit the necessary purity or because no control on the composition is available [21]. This thesis addresses this issue by proposing a entirely novel approach to the control of the composition of any FEBID process by using a two-adsorbate environment, applicable in its generality to any particle induced fabrication process relying on surface-adsorbed reactants.

We believe this thesis to be of high interest for the biomolecular community, providing them with an integrated sensor for bead sensing and tracking; for the micromagnetic sensors field, as we demonstrate a sensor fabricated in a *single-step* process exhibiting high resolution to local magnetic flux changes; for the FEBID community, as the two-adsorbate model proposed in this thesis allows reproducible control of the composition of composite deposits.

1.2 Structure and content of the thesis

This thesis has the following general structure: after two introductory chapters presenting the background of the thesis and the experimental setup used, the results of this thesis project are articulated in four chapters.

- In the first part of chapter 2, we introduce the FEBID process and give a historical review of the literature on FEBID of Cobalt. Also, we introduce the model used for the description in the FEBID process as proposed in the literature.
- In the second part of chapter 2, the magnetic formalism and phenomena used for the discussion of the magnetic properties of the material are introduced. Also, we compare Hall sensors to alternative sub-micron magnetic sensors.
- In chapter 3, the experimental setups used throughout this thesis are described.
- In chapter 4, we propose and discuss a novel approach to control the composition of any FEBID process by using a two-adsorbate environment, allowing to tune the deposit composition. We found a way to control the metallic content of the deposit using the *pulse period* of the electron-beam, decorrelating the composition from the electron beam current as in previous studies. This tunability is explained by introducing a novel, analytical model which explains for the first time the

evolution of FEBID processes when two adsorbates are present at the substrate surface. The model is validated by experimental evidence.

- In chapter 5, we investigate the magnetic properties of the deposited nanocomposite material. Various Hall sensors have been deposited by both FEBID and FIBID. Their magnetic properties are presented and are discussed in the light of an original Langevin fit of the Hall signal under increasing magnetic field. As shall be shown, this procedure allows the correlation of saturation properties, Hall effect and transport properties on composition and nanostructure, which are discussed in depth.
- In chapter 6, we report true single-bead detection using the obtained Hall elements. A novel, in-situ nanomanipulation setup allows the precise positioning of a microbead at any position with respect to the sensor surface under SEM visual feedback. We show that the magnetic flux resolution obtained by the use of the nanocomposite CoC material are not only sufficient to detect the presence or absence of a single micrometric superparamagnetic bead, but also to allow tracking its distance to the sensor surface.

Finally, the thesis ends with concluding remarks in chapter 7.

Chapter 2

Background

2.1 Focused electron-beam induced deposition

2.1.1 Electron-substrate interactions and principles of FEBID

Focused electron-beam induced deposition (FEBID) is a technique to perform deposition of material on surfaces on the nano-scale [15–17]. A selected, volatile *precursor* compound is introduced into a vacuum chamber, where it adsorbs on a surface. A focused electron-beam is irradiating the surface, leading to local dissociation of the adsorbed precursor molecule. Two products are formed: a non-volatile, functional product, which forms the *deposit* on the surface, and volatile by-products, which eventually desorb and are pumped away (see figure 2.1).

Ever since the use of electron beams in vacuum environments, deposition of undesired contamination from background chamber pressure hydrocarbons is reported [22–27]. Later on, several materials were found to be deposited by FEBID using the appropriate precursor molecules. Presently, of high industrial interest is the deposition of SiO₂ for mask-repair applications [28] and the deposition of high-density carbon for high-aspect-ratio AFM tips [29]. Especially, FEBID can be employed to obtain *metallic* nanostructures, which can be used to define local electric connections. The available metallic precursors are numerous. A widely studied metallic precursor is Tungsten carbonyl [30]. Metallic deposits interesting by their conductivity include Pt [31] and Au [32]. Deposition of various ferromagnetic metals has been investigated, such as Iron [33–35], Nickel [36] or Cobalt [19, 37–39]. The range of elements accessible for FEB induced deposition is shown in figure

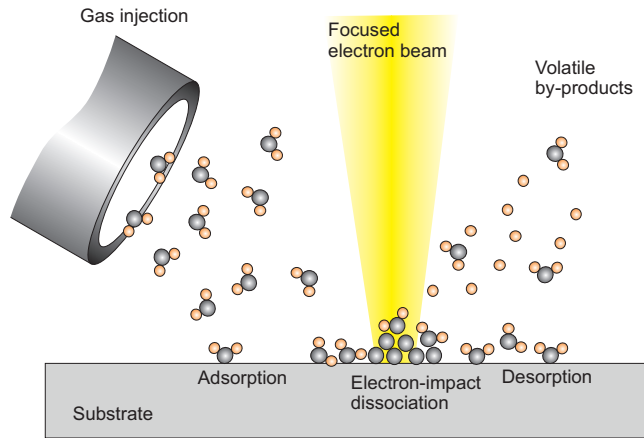


Figure 2.1: *FEBID principle.* Volatile precursor molecules are delivered to the vicinity of a substrate, where they (reversibly) adsorb. Under electron irradiation, some molecules are locally decomposed. The non-volatile part is deposited onto the surface, whereby volatile by-products desorb and are pumped away.

2.2. An overview of available precursors is found in [15] or [16].

FEBID is usually carried out in scanning electron microscopes (SEM). Resolutions obtained depend primarily on the diameter of the electron-beam, which is given by the electron source, the electron optics, the beam current and acceleration voltage employed [42]. Other parameters limit the resolution of the deposition, namely the substrate on which deposition takes place, the aspect ratio of the deposit [43] and the rate at which deposition takes place [44]. Best resolution obtained so far for FEBID deposits carried out in a SEM is 3nm full-width at half-maximum (FWHM) (in [45], using a 30kV, 5pA beam on a carbon membrane). Using a STEM microscope, sub-nanometric resolution was achieved (in [46], using a 200kV, 40pA beam on a Si_3N_4 membrane).

The FEBID process depends heavily on the physics of electron-matter interaction. In the following, we introduce the scattered electron distribution in a material under focused electron irradiation (see figure 2.3). An in-depth description of these interactions, which represents also the basics of scanning electron microscope imaging, can be found in [42, 47]. The focused electron-beam delivers a number of *primary electrons* (PE) showing an energy distribution closely centered around a energy defined as the primary electron energy E_0 . The radial electron distribution within the beam shows a Gaussian profile. When the electrons enter the substrate, multiple scattering occurs. Elastic scattering deflects the impinging electrons and some of them eventually are escaping back through the surface as *backscattered*

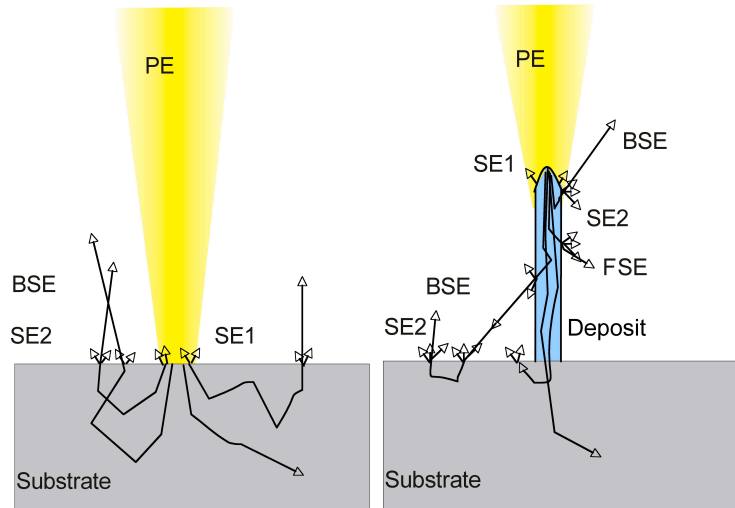


Figure 2.3: Schematic representation of electron interactions with solids. a) Impinging primary electrons (PE) are elastically and inelastically scattered. Some of the electrons might escape as high-energy back-scattered electrons (BSE). Scattering of the PE close to the surface excites low-energy electrons, some of which escape as secondary electrons (SE1). Similarly, scattering of BSE in vicinity of the surface might lead to secondary electron (SE2) emission. Note that in the presence of a thick surface (with respect to the electron path), most of the electrons are absorbed in the substrate. The scattering trajectories shown here are just exemplar; trajectory densities have to be calculated using Monte-Carlo simulation (see figure 2.4). b) In the case of a high aspect-ratio deposit, electrons can be scattered out of the deposit towards the substrate (forward-scattered electrons, FSE). Interaction of these electrons with the substrate generates in turn BSE and SE2 within a radius depending on the deposit height.

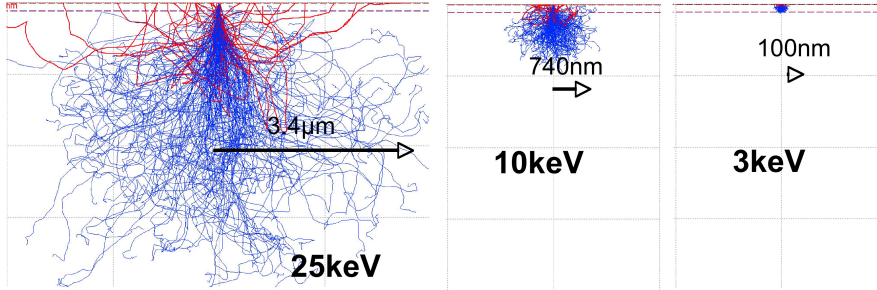


Figure 2.4: Simulated electron trajectories within a Si substrate covered with 150nm SiO₂. Monte Carlo simulations [40] for 25keV, 10keV and 3keV PE energies. Thin lines show absorbed PE, thick lines show electrons escaping as BSE. 200 trajectories are shown for each energy. The radius of the interaction volume is calculated using the formula in [41]. In the case of 3keV PE, the entire interaction volume is within the SiO₂ layer.

section $\sigma(E)$. The dissociation cross-section is a function of the energy of the dissociating electron and is generally believed to peak for low electron energies. Close to the point of impingement, the high density of primary electrons and SE1 lead to high deposition rates. Outside of the beam, BSE and SE2 lead to a low-profile deposit known as the halo, the diameter of which is defined by the escape width of backscattered electrons (see figure 2.3a).

In the case of high aspect-ratio deposits, like pillars, there is a probability that some of the impinging electrons are scattered and leave the deposit through the side walls. These electrons are known as *forward scattered electrons* (FSE). The interaction of the FSE with the substrate lead to a broadening of the halo, depending on the deposit height, as shown in figure 2.3b.

An example of structures realized by FEBID is shown in figure 2.6. Pillars and planar deposits are shown. In the case of planar deposits, the thickness of the deposit, as well as that of the halo, as estimated by the contrast on the SEM image, is found to depend on the overall electron dose delivered to the deposit. In the case of the pillar deposits, the overall dose determines the pillar height. Furthermore, it is apparent that higher deposits lead to a broadening of the halo by forward scattered electrons.

2.1.2 FEBID of Cobalt - literature results

With the discovery of the giant magnetoresistive effect (GMR) by Fert and Gruenberg in the late 1980ies [49, 50], deposition of ferromagnetic thin-films

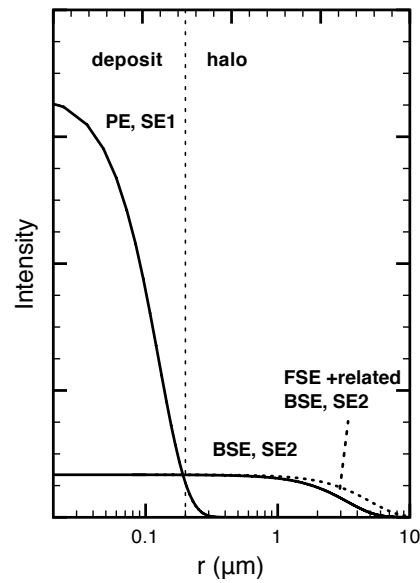


Figure 2.5: *Electron distribution for a Gaussian-shaped 25keV, 210nm FWHM electron-beam impinging on a Si substrate. Inside the Gaussian shaped beam, PE and the SE1 generated by them are in majority. Electron dissociation by the PE and the SE1 defines the actual deposit. Electron scattering in the substrate leads to BSE crossing the interface back to the vacuum outside the beam radius. The BSE and the SE2 generated by them lead to a thin halo around the deposit. In the case of a high aspect ratio deposit, electron can be forward-scattered out of the deposit (see figure 2.3). These FSE, along with the BSE and SE2 generated by them, lead to a broadening of the halo dependent on the deposit height.*

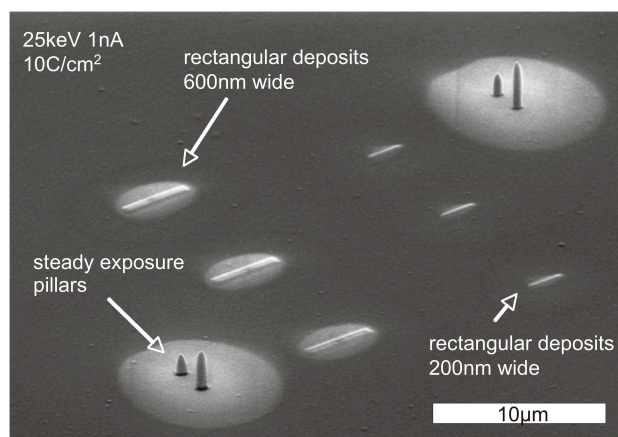


Figure 2.6: Example of deposits obtained by FEBID. Pillars obtained by steady exposure (60s and 120s) and rectangles obtained by raster-scanning the beam over a surface (with a dose of $10\text{C}/\text{cm}^2$) are shown. A halo is visible around the deposits, resulting from SE escape in the case of the rectangular deposits. Forward-scattered electrons increase the diameter of the halo in the case of the pillar deposits.

became a point of focus for top-notch research. For this reason, cobalt deposition of surface-adsorbed molecules by CVD was extensively studied throughout the 1990ies. CVD from various precursors is reported, including $\text{Co}_2(\text{CO})_8$ [51, 52], $\text{HCo}(\text{CO})_4$ [51], $\text{Co}(\text{C}_5\text{H}_5)_2$, $\text{Co}(\text{C}_5\text{H}_5)(\text{CO})_2$, $\text{CoCF}_3(\text{CO})_4$ [52], $\text{CoNO}(\text{CO})_3$ [53], $\text{Co}(\text{acac})_2$ [54], and, in [55], $\text{Co}_3(\text{CO})_9\text{CCl}$, $\text{Co}_3(\text{CO})_9\text{CH}$, $\text{Co}_2(\text{CO})_6(\text{HC}\equiv\text{Ph})$, $\text{Co}_2(\text{CO})_6(\text{HC}\equiv\text{C}^t\text{Bu})$, where “Ph” denotes a phenyl group (C_6H_5 -), “acac” is acetylacetonate ($\text{C}_5\text{H}_7\text{O}_2^-$) and “ $t\text{Bu}$ ” is the tertiary butyl group ($[\text{CH}_3]_3\text{C}$ -). It was found that some of them dissociate readily under temperature [56]. FEBID puts the following restrictions, some of which are conflicting, to the choice of molecules. The precursor compound has to be stable at room temperature, but exhibit a high cross-section for electron-impact dissociation. The precursor compound has to be volatile at room temperature in order to leave the unirradiated parts of the surface, but the sticking coefficient and the surface residence time have to be high enough, so that the hitting of an adsorbed molecule by an impinging electron is a likely event. The vapor pressure of the compound is important as it determines the amount of molecules that will evaporate and be transported to the point of electron irradiation by the gas injection system [15]. Finally, the electron-impact dissociation of the compound ideally has to yield a material with a high Co content. For this reason, the deposition of local Cobalt-containing structures using focused particle beams is reported

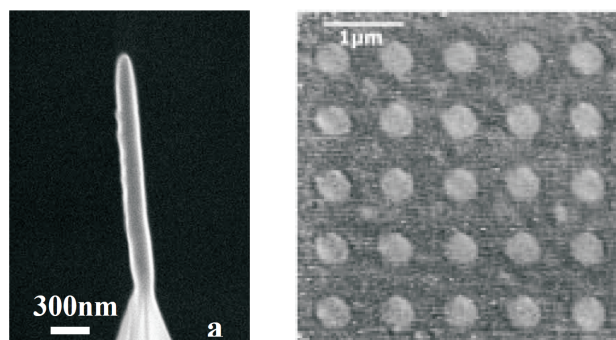


Figure 2.7: *High aspect-ratio Cobalt tip obtained by focused electron-beam induced deposition of Cobalt carbonyl (left). The tips are grown on standard SPM tips and provide a MFM resolution of 40nm. From [38]. Array of 150nm dots obtained by focused ion-beam induced deposition of Cobalt carbonyl (right). The dots exhibit ferromagnetic behaviour. From [58].*

with the compounds dicobalt octacarbonyl $\text{Co}_2(\text{CO})_8$ and Cobalt tricarbonyl nitrosyl $\text{Co}(\text{CO})_3\text{NO}$.

In 2001, deposition of Cobalt-containing tips for magnetic force measurements (MFM) purposes was presented by Utke et al. [38, 57]. High aspect-ratio tips with apex diameters down to 50nm were deposited on top of prefabricated Silicon SPM tips using a focused electron-beam and the precursor dicobalt octacarbonyl. The dependence of the tip diameter on the beam size was shown [57]. A Cobalt concentration of 34at.% was measured by Auger electron spectroscopy, leading to a resistivity four orders of magnitude higher than pure Cobalt. The characteristic deposit structure, consisting of Cobalt nanocrystals embedded in a carbonaceous matrix, was shown by TEM diffraction on deposits realized across carbon TEM-grids. A deposition pathway including tetra-cobalt dodeka-carbonyl ($\text{Co}_4(\text{CO})_{12}$) as an intermediate product was proposed [38]. Finally, the obtained purity proved sufficient to record MFM images with a resolution of 40nm [57].

A year later, successful deposition by focused ion-beam dissociation of $\text{Co}_2(\text{CO})_8$ is reported by Lapicki et al. [58, 59]. The authors used the term ion-beam induced chemical vapor deposition (IBICVD) as a synonym for FIBID. Arrays of 100-150nm-sized dots were deposited on carbon membranes [58] and the deposits were shown to exhibit a measurable ferromagnetic behavior [59].

A more detailed study of the electron-beam induced deposition of Cobalt was published by Lau et al. [37], who investigated the deposition of Cobalt pillars by FEBID. Cobalt contents between 30 and 50 at.% are reported. The

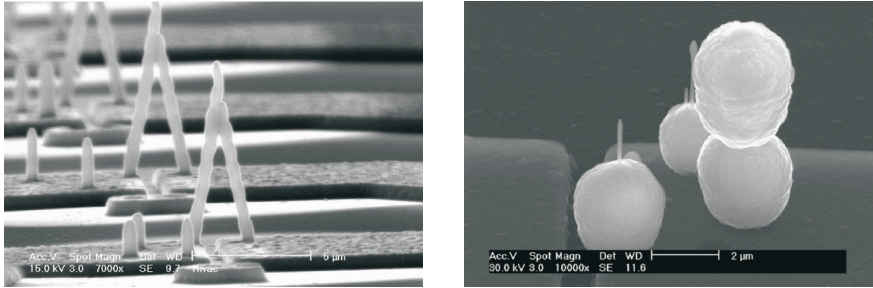


Figure 2.8: *FEBID of Cobalt carbonyl resulting in arch structures bridging two electrodes (left). The setup allows for simple two-point electrical characterisation of the deposit’s resistivities. Thermal decomposition of Cobalt carbonyl nitrosyl ($\text{CoNO}(\text{CO})_3$, right) using the focused electron beam as a heating source. Auto-catalytic growth beyond a certain tip height is reported, leading to these ball-like structures. From [37].*

authors studied the growth characteristics in terms of height and diameter growth rates of the deposited pillars. The resistivity of the deposits was assessed using a two-electrode setup, connected by a FEBID “arch” across them. Resistivities down to $160 \mu\Omega\text{cm}$ were measured, 26 times the value for bulk Cobalt ($\rho_{\text{Co}}=6.2\mu\Omega\text{cm}$). The electric resistivity was found to scale inversely with the beam current used during deposition, and could be reduced by thermally annealing the structures after the deposition by passing electrical currents of up to some μA through them. Whereas these results were obtained for the precursor dicobalt octacarbonyl, the authors also investigated Cobalt tricarbonyl nitrosyl as a precursor. Thermal decomposition of the latter precursor by electron-beam heating was reported. Finally, the authors proposed the use of Cobalt deposits as a template for the local growth of carbon nanotubes (CNT). This idea was realized in 2009 by Ervin et al. [60] who demonstrated selective CNT growth at the locations where previous Cobalt FEBID from $\text{Co}(\text{CO})_3\text{NO}$ had been carried out.

However, understanding the exact deposit structure and its dependence on the composition had yet to be investigated. In [18], Utke et al. report Cobalt concentrations between 12 and 80 at.%, depending on the electron beam current used for the deposition (20pA to $\geq 10\text{nA}$). The nanocomposite CoC structure of the deposit was confirmed. Thermal decomposition of $\text{Co}_2(\text{CO})_8$ was shown to occur for irradiation currents $\geq 3\mu\text{A}$ on a Si substrate, leading to the formation of polycrystalline balls much larger than the beam diameter. As the onset of thermal decomposition depends on the height of the deposit, the thermal conductivity of the deposit could be estimated to

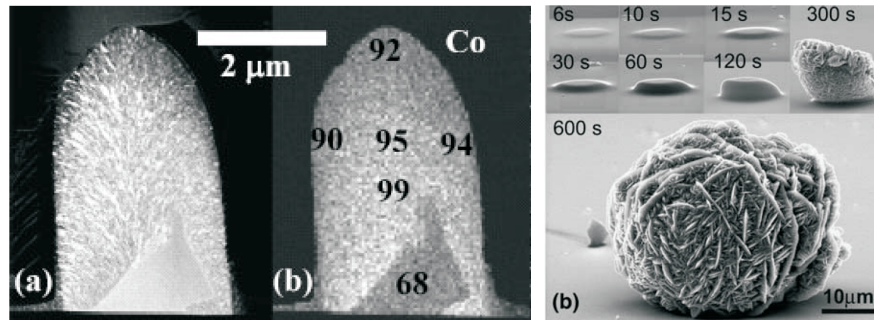


Figure 2.9: Cross-section of FEBID pillar from $\text{Co}_2(\text{CO})_8$ (left). A Cobalt-poor core and a Cobalt-rich crust can be distinguished. From [18]. Thermal decomposition of $\text{Co}_2(\text{CO})_8$ under $3 \mu\text{A}$ irradiation. As the pillar grows higher, dissipation of the thermal excitation by the electron-beam to the substrate is reduced, leading to an enhanced local heating. From [19].

$0.2\text{W}/\text{cm}\cdot\text{K}$. In [19], cross-sections of Co-deposits were investigated, pillars were grown and sliced by FIB-milling, allowing insight in the inside structure of Co-FEBID deposits. During initial deposition, a homogeneous nanocomposite core structure (Co nanocrystals in carbonaceous matrix) was shown to be formed, whereas a distinct, Cobalt-rich sub-structure (“crust”) was shown to develop as the aspect ratio of the deposit increases.

Another series of publications dealt with the mechanical properties of the Co-C deposits. In [39], the density of Co-FEBID structures was assessed by electron-beam induced deposition on atomic force microscopy (AFM) cantilevers. It was shown that the deposit’s density scales linearly with the Cobalt content, being in the order of $4.2\text{g}/\text{cm}^3$ and $7.2\text{g}/\text{cm}^3$ for Cobalt contents of 30 and 70at.%, respectively. The tensile strength of the Co-C deposits was measured to be in the range of 1GPa in [61].

An important application for Cobalt deposits was shown in [20], where Boero et al. demonstrated a nano-Hall sensor realized by FEBID of Cobalt carbonyl. A cross-shaped deposit was realized between predefined Gold electrodes, thus defining a Hall structure. The device showed an active area of $(500\text{nm})^2$, a sensitivity to the magnetic field of between 0.8 and $1.2\text{V}/\text{AT}$ and a resolution of about $10\mu\text{T}/\text{Hz}(1/2)$. While the resistivity of the deposited material was measured to be two orders of magnitude higher than that of pure Cobalt, the device exhibited a high extraordinary Hall effect (EHE), up to saturation fields of about 1T, making them very interesting candidates for high-resolution, sub-micron magnetic sensing devices. Furthermore, for some of the experimental devices, quite high sensitivities ($3\text{V}/\text{AT}$) to in-plane magnetic fields were recorded.

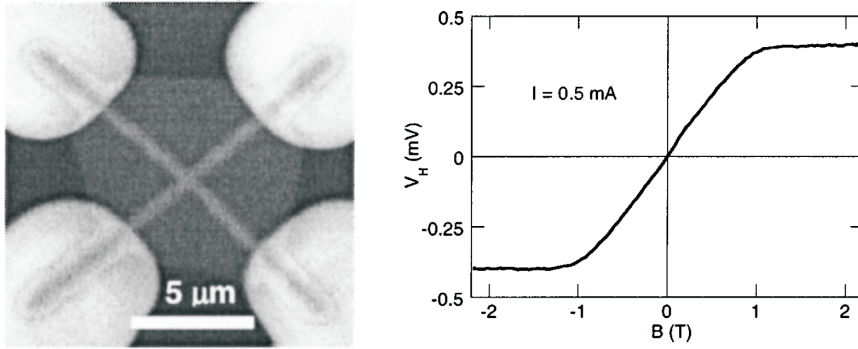


Figure 2.10: Submicrometer Hall sensor fabricated by FEBID of $\text{Co}_2(\text{CO})_8$ (left) and measured voltage response to a perpendicular external magnetic field (right). The sensitivity to the magnetic field, given by the slope of the response at low fields, is about $1.2\Omega/\text{T}$. From [20]

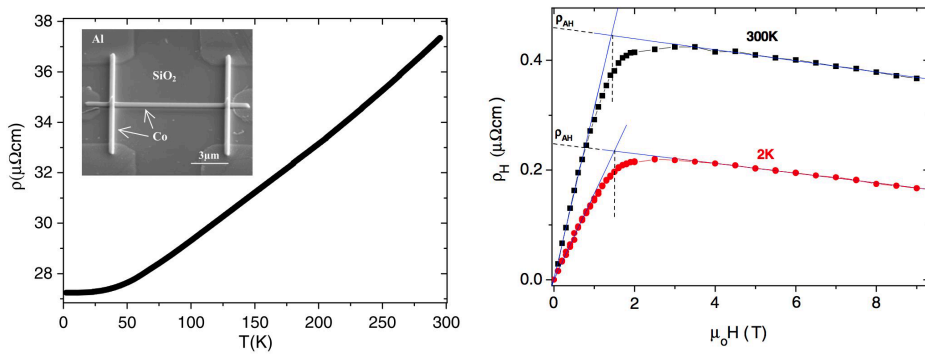


Figure 2.11: Electrical (left) and Hall resistivity (right) of almost pure (around 95at.%) Co-FEBID structures. ρ_{AH} is the extraordinary Hall resistivity. From [62]

The electric transport properties under magnetic field have been investigated in-depth by the group of de Teresa et al. [62] The authors report purities of Co-FEBID structure of $\geq 90\text{at.}\%$. These pure deposits showed an electrical resistivity only a factor 7 above bulk value. Accordingly, metallic behaviour under temperature variation was found, whereas semiconducting behaviour was shown for deposits with Cobalt contents of $80\text{at.}\%$. From low-temperature measurements, the mean free path of electrons in the structure was found to be in the same order as the grain-size of the deposit (4nm), pointing to a scattering mainly at the grain boundaries. The investigated structures showed a magnetoresistance of $0.65\text{-}0.7\%$., proving collective alignment of the magnetic domains in the polycrystalline deposit under the applied external field. In further works [63, 64], the authors studied the behaviour of domain walls in the structures and found good agreement with (pure) Cobalt deposits obtained by electron-beam lithography (EBL).

Finally, the importance of FEB induced heating during deposition from $\text{Co}_2(\text{CO})_8$, which decomposes spontaneously already a few tens of degrees above room temperature, was evidenced by the same group in [65], where the authors report experimental deposition on a substrate mounted on a hot plate. A clear relation between deposit composition and substrate temperature was monitored, allowing the use of lower currents for the deposition of high-purity Co structures.

2.1.3 FEBID rate model in the presence of a single adsorbate species

When an electron beam hits a surface on which molecules are adsorbed, dissociation of the surface-adsorbed molecule can occur, leading to the growth of a deposit. In terms of a generic chemical reaction, this is expressed as:



where A is the adsorbate species, D_A is the non-volatile, deposited reaction product and V_A represents the volatile reaction product which desorbs to the vacuum. One approach to a quantitative description of this phenomenon lies in using computer simulation techniques based on Monte-Carlo (MC) algorithms [66, 67]. The advantages to this approach are manifold. These simulations allow to explain the mechanisms of radial growth of pillar structures [68] or prediction of the ultimate resolution of the FEBID process [69, 70]. In a recent effort, the precursor parameters (surface diffusion coefficient, sticking probability, surface residence time) for tungsten carbonyl $\text{W}(\text{CO})_6$ were retrieved by fitting a MC simulation to an array of experimental data [71].

Another approach lies in the derivation of an analytical description, which allows the prediction of general deposition regimes and fundamental scaling laws [44]. Both approaches are complementary. In the following, we focus on the analytical approach as we introduce a general analytical model of the FEBID process in the presence of a single adsorbate species and show the solution for this model when using pulsed electron beams.

Several analytical models to FEBID were developed, trying to explain the growth in a quantitative manner [72–74]. In a general way, the growth rate of the deposit as a function of the distance r from the axis of the electron beam is expressed as [15, 67, 75]:

$$R(r) = Vn(r) \int_0^{E_0} \sigma(E)f(E, r) dE \approx Vn(r)\sigma(E_0)f(r) \quad (2.2)$$

where V is the volume of the decomposed molecule, $n(r)$ is the number of adsorbed molecules per surface unit, $\sigma(E)$ is the energy dependent electron impact dissociation cross section, E_0 is the energy of the incident primary electrons and $f(E, r)$ is the energy dependent electron flux containing the contributions of the primary electron flux and the fluxes of emitted secondary and backscattered electron with their respective energy spectra. The term $f(E, r)$ can be estimated performing MC simulations of electron scattering and the resulting energy loss and trajectories. However, the precise solution of equation 2.2 necessitates knowledge of the energy dependent electron impact dissociation cross section $\sigma(E)$, which is generally unknown for the electron energies involved in FEBID. As a consequence, a simplified expression is introduced in equation 2.2, where the term $\int_0^{E_0} \sigma(E)f(E, r) dE$ is approximated by the term $\sigma(E_0)f(r)$. Here, $\sigma(E_0)$ represents an effective dissociation cross-section for the specific primary electron energy [44]. The values of $\sigma(E_0)$ are generally known to decrease with increasing PE energy (within the energy range used for FEBID, i.e. $1\text{keV} \leq E_0 \leq 200\text{keV}$) and have been determined for some molecules [30, 74, 76].

The spatial electron distribution $f(r)$ is a convolution of the Gaussian distribution of primary electrons with the distribution of emitted electrons (BSE+SE). It has been stated that when discussing equation (2.2) in terms of full width at half maximum of the deposit, this distribution can be reasonably approximated by the Gaussian PE distribution [44]. In the case of linear or planar deposits such as those investigated in this thesis, one is not so much interested in the exact nature of the distribution convolution, but in the deposition dynamics on a specific substrate under irradiation at an PE energy

E_0 . For this reason, we will approximate the term $f(r)$ by the impinging primary electron flux $f_{PE}(r)$. To this extent, the effective dissociation cross-section $\sigma(E_0)$ might include a hidden, substrate-specific dependency (BSE and SE yield).

We now turn to the expression of the adsorbate surface density $n(r)$. Neglecting surface diffusion, the number of adsorbed molecules per surface unit $n(r)$ can be expressed using the following adsorption rate [74]:

$$\frac{\partial n}{\partial t} = sJ \left(1 - \frac{n}{n_{ML}}\right) - \frac{n}{\tau} - \sigma f n \quad (2.3)$$

Here, J is the flux of precursor molecules impinging on the substrate from the gas phase, n_{ML} is the maximum monolayer density, s is the sticking probability and τ is the mean residence time before the molecule desorbs spontaneously. The term $(1 - n/n_{ML})$ limits the maximum surface coverage to one monolayer. n/τ and $\sigma f n$ are the spontaneous desorption rate and the rate of adsorbate dissociation by the electron beam. An analytical solution for the steady state (i.e. for an irradiation time $t \rightarrow \infty$) can be derived for equation (2.3), leading to the relation:

$$R(r) = n(r)V\sigma f(r) = \frac{sJ}{sJ/n_0 + 1/\tau + \sigma f(r)}V\sigma f(r) = n_d V\sigma f(r) \quad (2.4)$$

where n_d corresponds to the depleted, steady-state surface adsorbate density (see figure 2.12, dotted line).

However, when depositing linear (1D) or planar (2D) structures, such as current lines or nano-Hall plates, the beam is raster-scanned over a surface, which requires differentiating between periods of time when a certain pixel is exposed to an electron flux (irradiation), leading to a time-dependent decrease of the number of surface adsorbed molecules, and period of times where the pixel is not irradiated and the number of surface adsorbed molecules increases through refreshment (replenishment). The solution for the surface adsorbed density in the center of such a pulsed beam is expressed as [15]:

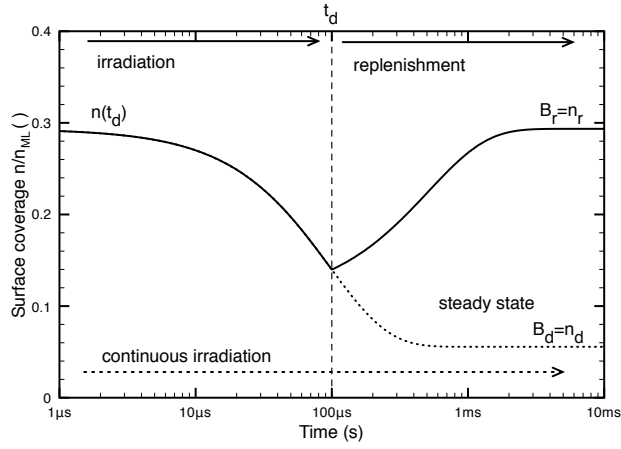


Figure 2.12: Surface coverage, corresponding to the adsorbate density normalized to the monolayer adsorbate density, of $\text{Co}_2(\text{CO})_8$ molecules under pulsed electron irradiation. n_r represents the surface adsorbate density at equilibrium between adsorption and spontaneous (thermal) desorption. $n_d = \lim_{t_d \rightarrow \infty} n(t_d)$ is the steady state surface adsorbate density corresponding to the equilibrium between adsorption on one side and spontaneous desorption and electron-impact adsorbate dissociation on the other side corresponding to full depletion (dotted line). Parameters used: $\sigma = 4.95e-3 \text{ nm}^2$, $\tau = 720 \mu\text{s}$, $n_0 = 2.6 \text{ nm}^{-2}$, $J = 1.5e17 \text{ cm}^{-2} \text{ s}^{-1}$ and $f = 1.7e20 \text{ cm}^{-2} \text{ s}^{-1}$.

$$n(t) = C \cdot \exp[-k \cdot t] + B \quad (2.5a)$$

$$k = \begin{cases} k_d = sJ/n_{ML} + 1/\tau + \sigma f \\ k_r = sJ/n_{ML} + 1/\tau \end{cases} \quad (2.5b)$$

$$B = \begin{cases} B_d = n_d = sJ / (sJ/n_{ML} + 1/\tau + \sigma f) \\ B_r = n_r = sJ / (sJ/n_{ML} + 1/\tau) \end{cases} \quad (2.5c)$$

$$C = \begin{cases} C_d = (n_r - n_d) [\exp(-k_r t_r) - 1] [\exp(-k_r t_r) \exp(-k_d t_d) - 1]^{-1} \\ C_r = (n_d - n_r) [\exp(-k_d t_d) - 1] [\exp(-k_r t_r) \exp(-k_d t_d) - 1]^{-1} \end{cases} \quad (2.5d)$$

We denote the electron pulse duration as the dwell time t_d . During the irradiation ($t < t_d$, subscripts d), the number of surface adsorbed molecules inside the beam falls exponentially, as dissociative depletion occurs. After irradiation ($t > t_d$, subscripts r), the surface sites are filled again by replenishment. The time evolution of surface adsorbed molecules is shown exemplarily in figure 2.12 for FEBID of Cobalt carbonyl. The surface adsorbate density decreases with irradiation time ($t_d \rightarrow \infty$), to eventually reach the depleted steady state n_d . If the beam is blanked and replenishment is allowed to take place, a replenished state n_r is reached. The rate at which depletion and replenishment occur is described by k_d and k_r which are the rate constants of the depletion and replenishment processes (in units of s^{-1}).

We now introduce the dissociation yield Y , describing the dissociative events per primary electron during the irradiation period t_d , i.e. the yield of the chemical reaction introduced in (2.1). The yield is given by integration of the surface adsorbate densities $n(t)$ over the dwell time t_d and multiplication with the effective dissociation cross-section σ :

$$Y = \sigma \int_0^{t_d} n(t) dt / t_d \quad (2.6)$$

The unitless yield Y is a description of the probability for an impinging primary electron to lead to the dissociation of an adsorbed molecule. For short dwell times ($t_d \rightarrow 0$) and full replenishment of the surface between irradiations, the yield is limited by the electron flux (and the process regime is hence called electron-limited) and the yield is maximized. For longer dwell times, depletion occurs (as shown in figure 2.12) and the yield decreases accordingly. Multiplication of the yield with the electron flux f and the

volume of the decomposed molecule V leads to the general expression of the deposition rate using a pulsed electron beam [15, 30, 77]:

$$R = V\sigma f \left(\frac{(n_r - n_d) [1 - \exp(-k_r t_r)] [1 - \exp(-k_d t_d)]}{k_d t_d \exp(-k_r t_r) \exp(-k_d t_d)} + n_d \right) \quad (2.7)$$

where t_r is the refresh time, i.e. the time elapsing between two subsequent irradiations. The condition for full adsorbate replenishment is fulfilled for $k_r t_r \gg 1$, i.e. when the time between electron pulses is much larger than $1/k_r$, the rate constant of the replenishment process. In this case, equation (2.7) simplifies to:

$$R = V\sigma f \left[(n_r - n_d) \frac{1 - \exp(-k_d t_d)}{k_d t_d} + n_d \right] \quad (2.8)$$

2.2 Magnetic microsensors for bead sensing

In biosensor technology, there are numerous ways to track the presence and measure the concentration of a specific biochemical species (biomolecular recognition). The use of magnetic labels is advantageous in many respects for the tracking of the biomolecule of interest [78–80]: it is possible to manipulate the analytes attached to the superparamagnetic beads, using the bead as a force transducer; in most biological samples, there is no magnetic background, so that the measurement technique does not interfere with the sample; very small amounts of analytes can be reliably detected, whereas other detection schemes (e.g. fluorescent labels) require a certain concentration threshold to be reached.

Superparamagnetic bead detection imposes severe constraints on the sensor to be operated. They must exhibit sizes of similar order of magnitude as the magnetic label, i.e. in or below the micrometer size range (see table 2.1 for bead sizes); they must exhibit a sensitivity sufficient to detect the small magnetic field induced by the magnetized bead; they require saturation fields sufficiently high as not to saturate under the external field required to magnetize the microbeads.

In this section, we introduce the formalism used for the estimation of the magnetic field produced by a magnetized superparamagnetic microbead. This magnetic field is highly localized. Several physical principles make it possible to realize micromagnetic sensors with sensitivities sufficient to measure the magnetic field produced by several or just one single such superparamagnetic bead. These principles and sensors are presented for comparison.

2.2.1 Magnetic properties of superparamagnetic microbeads

Superparamagnetic microbeads consist of FeO_x superparamagnetic nanoparticles embedded in a non-magnetic polymer matrix. The nanoparticle consisting of the ferromagnetic material are sufficiently small in size ($<30\text{nm}$ for magnetite Fe_3O_4) that thermal agitation overcomes the remanent magnetisation at zero field [81, 82]. Thermal fluctuation aligns the direction of magnetisation of the individual nanoparticles randomly, so that the overall bead's magnetisation is averaged to zero. For this reason, the superparamagnetic beads do not exhibit ferromagnetic behaviour in the absence of an external field at room temperature. However, in the presence of an external magnetic field, the magnetizations in the individual nanoparticles are aligned in the field direction, so that the overall magnetic induction in the bead is then orders of magnitude higher than the one obtained in the case of paramagnetic

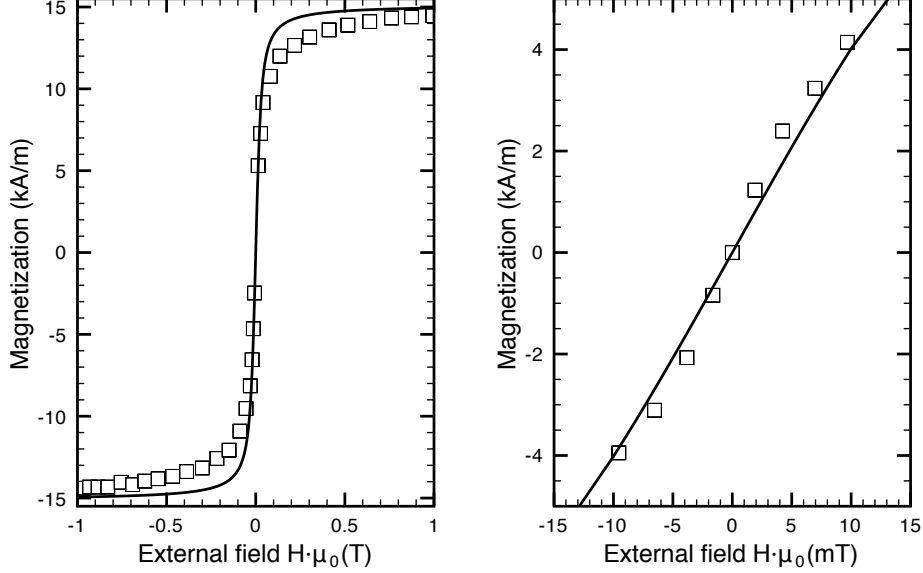


Figure 2.13: Magnetization versus applied field for a Dynabead M-280. Experimental values are reproduced from VSM measurements published in [83]. The magnetic susceptibility χ is obtained from the linear fit around 0. Inserting χ into a Langevin model curve (equation (2.14)) one obtains the model magnetization curve shown.

materials. This makes these beads interesting in molecular research: the zero-remanence allows for bead separation and prevents clustering in fluidic environment, while the high magnetisation under external field allows for magnetic signal detection and magnetic handling of the beads. The possibility to functionalize the surface of the beads with adequate biomolecules allows for the fixation of various molecules to the microbead [13].

The response of any material to an external magnetic field is governed by its magnetic susceptibility χ , which describes the relation between the magnetisation M of the material and the external field H and hence represents a material property:

$$\vec{M} = \chi \vec{H} \quad (2.9)$$

The magnetic induction B is then given by:

$$\vec{B} = \mu_0(\vec{H} + \vec{M}) \quad (2.10)$$

where $\mu_0 = 4\pi \times 10^{-7} \text{H} \cdot \text{m}^{-1}$ is the permeability of vacuum. In SI units, the magnetic field H and the magnetisation M are expressed in A/m ; the units

for the magnetic induction B is the Tesla ($1T = 1Vs/m^2$). The magnetic moment, used as a measure of the “strength” of a magnetic source, is then given by the product of the magnetisation M and the volume of the bead V_{bead} :

$$\vec{m} = V_{bead} \cdot \vec{M} \quad (2.11)$$

In the case of superparamagnetism, χ is a function of the applied field $\chi = f(H)$. The magnetisation can be found by taking the potential energy U_H of any magnetic moment m_p making an angle θ with regard to the external field H , given by [84]:

$$U = -\vec{m}_p \cdot \mu_0 \vec{H} = -m_p \cdot \mu_0 H \cdot \cos \theta \quad (2.12)$$

where m_p is the individual particle’s magnetic moment. By averaging $\cos \theta$ over the Boltzmann distribution, one finds the fraction of the total magnetization that has been aligned by the external field. This is expressed by the Langevin function:

$$L(H) = \coth(m_p \mu_0 H / kT) - \frac{kT}{m_p \mu_0 H} \quad (2.13)$$

where k is the Boltzmann constant and T is the temperature. Hence, the magnetisation M of a superparamagnetic material as a function of the applied field H is described as:

$$M(H) = M_{sat} \cdot L(\alpha \mu_0 H) = M_{sat} \cdot \left[\coth(\alpha \mu_0 H) - \frac{1}{\alpha \mu_0 H} \right] \quad (2.14)$$

where M_{sat} denotes the magnetization at saturation, including demagnetization effects:

$$\lim_{H \rightarrow \infty} M(H) = M_{sat} \quad (2.15)$$

α is a factor describing the thermodynamic arrangement of the nano-particles:

$$\alpha = \frac{m_p}{kT} \quad (2.16)$$

The corresponding low-field susceptibility can be calculated by derivation of the Langevin function and is given by [84]:

$$\lim_{H \rightarrow 0} \frac{dM(H)}{dH} = \frac{M_{sat} \cdot \alpha \cdot \mu_0}{3} = \chi \quad (2.17)$$

Saturation magnetisations, low-field susceptibility and magnetic moments at saturation obtained for a selection of commercially available microbeads

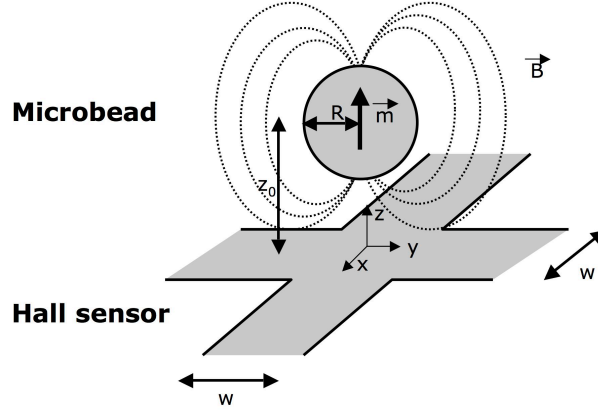


Figure 2.14: Schematic representation of the bead detection geometry. A microbead with radius R is located above a sensor with a quadratic active area of width w . The distance between the center of the bead and the surface of the sensor is z_0 . The magnetic moment \vec{m} of the microbead generates a magnetic field \vec{B} .

are shown in table 2.1. A typical microbead response to an external field is shown in figure 2.13. Experimental points are taken from [83] and compared with a Langevin model curve. Clearly, it appears in figure 2.13a that the Langevin function is only approximating the magnetization values obtained experimentally and found in literature. A more detailed study of an individual superparamagnetic bead response is found in [85]. Rather than taking the Langevin function of mono-disperse, single size magnetic nanoparticles, the authors implement a distribution function describing the magnetic moment distribution of the nanoparticles. However, the behaviour at low-field (2.13b) is well described by the linear part of the simple Langevin function.

2.2.2 Magnetic field generated by a microbead

A microbead exhibiting a magnetic moment \vec{m} produces a magnetic field, which is described using the magnetic dipole model[86]:

$$\vec{B} = \frac{\mu_0}{4\pi} \frac{3(\vec{m} \cdot \vec{r})\vec{r} - \vec{m}r^2}{r^5} \quad (2.18)$$

where $\vec{r} = [x, y, z]$ denotes the vector from the dipole center to a point in space. The magnetic field in any point $[x, y, z]$ is defined in amplitude and direction and as such is a vector field. We now consider the geometry

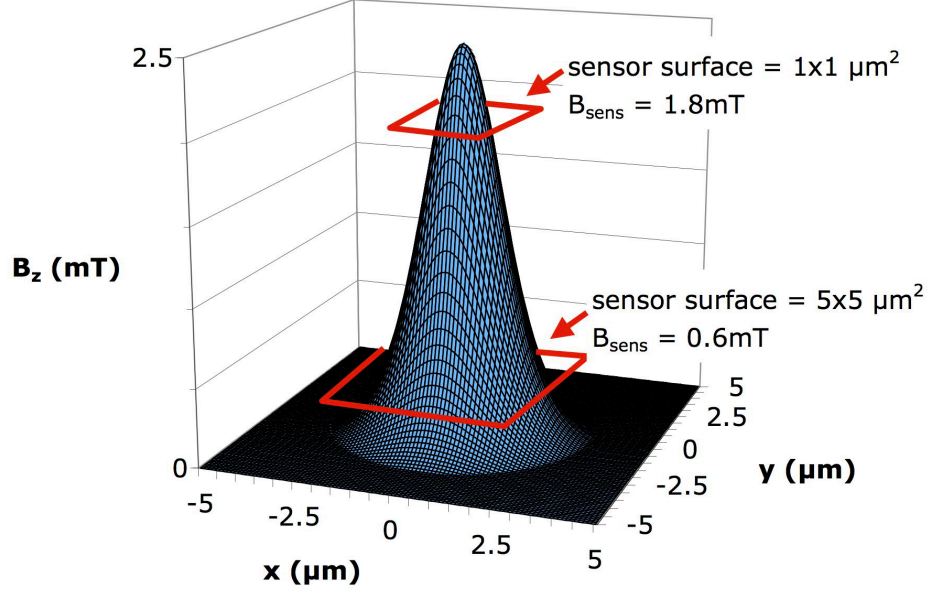


Figure 2.15: Vertical magnetic field component B_z from a typical microbead (Dynabead M-280) at saturation ($R=1.4\mu\text{m}$, $m=1.7\times 10^{-13}\text{Am}^2$) suspended $1\mu\text{m}$ above the xy -plane. B_z is calculated according to equation (2.19). The schematically drawn slices represent active areas of $1\times 1\mu\text{m}^2$ and $5\times 5\mu\text{m}^2$ and are drawn at the values corresponding to the averaged bead field B_{sens} , calculated with equation (2.20)

shown in figure 2.14. As the Hall sensor is sensitive only to the out-of-plane component of the magnetic field, we assume a bead magnetization $\vec{m} = [0, 0, m]$ perpendicular to the sensor area. The magnetic field in the direction parallel to the magnetisation is then given by:

$$\begin{aligned} B_z &= \vec{B}([0, 0, m]) \cdot [0, 0, 1] \\ &= \frac{\mu_0 m}{4\pi} \frac{2z^2 - x^2 - y^2}{(x^2 + y^2 + z^2)^{5/2}} \end{aligned} \quad (2.19)$$

The magnetic field produced by a micron-sized magnetic dipole, such as a magnetized microbead, is highly localized in space, as can be seen in figure 2.15, showing the perpendicular magnetic field component B_z for a Dynabead M-280 ($R=1.4\mu\text{m}$). The bead field is maximum in the axis of the magnetization, and decays rapidly in the radial direction, over a distance which is in the order of magnitude of the bead radius R .

The magnetic field induces changes in the resistivity of the Hall sensor

(see section 2.2.4). Hence, the sensor output will conceptually represent a convolution of the current densities through the Hall element with the distribution $B_z(\vec{r})$ given by equation (2.19). As a consequence, the magnetic field as measured by the sensor represents an average of the magnetic field $B_z(\vec{r})$ over the active area $w \times w$ of the sensor. For this reason, in order to obtain an estimate of the field strength influencing the sensor, B_z is averaged over the sensor area using a weighted integral. In the case of a quadratic Hall plate of width w , sensitive only to a field perpendicular to its surface, and for a magnetic moment \vec{m} directed in the same direction, i.e. perpendicular to the sensor surface, the measurable field at distance z_0 between the sensor and the center of the microbead is expressed as:

$$B_{sens} = \frac{1}{w^2} \iint_{-w/2}^{w/2} B_z(x, y, z_0) dx dy \quad (2.20)$$

Due to the spatially inhomogeneous character of the magnetic field $B_z(\vec{r})$, the averaged magnetic field B_{sens} is highly dependent on the sensor width w . This is schematically represented in figure 2.15. Weighted integration over a smaller sensor surface yields higher values for the sensed field B_{sens} as compared to larger sensor surfaces, which encloses also parts of the space where the values of the magnetic field $B_z(\vec{r})$ induced by the microbead are low. The bead field as seen by the sensor B_{sens} is shown in figure 2.16 for a typical microbead and for different sensor sizes. It is apparent that B_{sens} rapidly decreases and vanishes within a scale corresponding roughly to the bead size. For sensor widths above the size of the microbead, the measurable signal rapidly decreases over orders of magnitude. For this reason, the possibility to obtain magnetic sensors with small active areas, i.e. in the order or smaller than the bead diameter, is crucial to enhance the response to the magnetic field of a microbead.

For sensor dimensions much smaller than the microbead dimensions, i.e. when the condition $w \ll R$ is verified, the integration in equation (2.20) is done over $x, y \ll z_0$ and the bead field as seen by the sensor can be approximated by the dipolar bead field (equation (2.19)). Providing absolute centering of the dipole ($x = y = 0$), equation (2.20) simplifies to:

$$B_{sens} = \frac{\mu_0 m}{2\pi z^3} \quad (2.21)$$

The maximal bead field is measured when the bead lays centered on the sensor surface: $B_{sens,max} = B_{sens}(0, 0, d/2)$, where d is the bead diameter. In figure 2.16, the dependency of the bead field as measured by the sensor on the distance between the bead and the sensor surface is illustrated. It can be

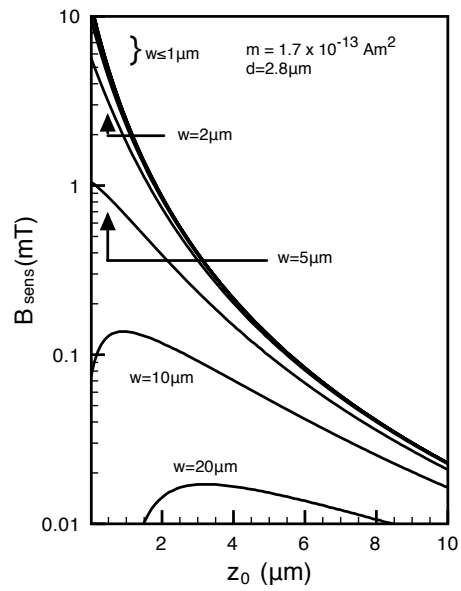


Figure 2.16: *Bead field B_{sens} averaged over the sensor active area according to equation (2.20) for various sensors widths. z is expressed as the bead surface to sensor surface distance, i.e. accounting for an offset of $d/2$.*

Table 2.1: Selection of commercially available microbeads and their properties. χ represents the low-field magnetic susceptibility. Sources: [83], [87], [85].

Bead, producer	diameter μm	M_{sat} kA/m	χ	m_{sat} Am^2
Dynabeads M-280, Dynal	2.8	15.1	0.5	1.7×10^{-13}
Dynabeads M-450, Dynal	4.4	31.4	1.6	1.4×10^{-12}
Myone, Dynal	1.0	40.0	1.4	2.1×10^{-14}
Micromer-M, Micromod	2.0	4.0	0.3	1.7×10^{-14}
Nanomag-D, Micromod	0.25	20	6.0	1.4×10^{-15}
Sigma Bead, Sigma	1.2	49.4	0.81	4.4×10^{-14}

noted that the decrease of magnetic flux in the sensor plane with the bead distance z follows a z^{-3} trend for small sensors, as obtained by derivation of equation (2.19). Hence, beneath the importance of having an active area of the sensor in the same order as the bead diameter, minimizing the distance between the microbead and the sensor surface is necessary in order to obtain a good magnetic signal allowing for single-bead detection.

2.2.3 Figures of merit for magnetic microsensors used for microbead detection

In section 2.2.2, we have shown that the width of a sensor is determinant for the ability of the sensor to detect the highly localized field of a microbead. In this section, we discuss the additional figures of merit for magnetic microsensors in microbead detection applications. They are: the sensitivity to the magnetic field S_I , the minimum detectable field B_{min} and the minimum detectable change in the magnetic flux Φ_{min} .

Sensitivity to the magnetic field

A magnetic sensor is basically a transducer which allows the translation of the local magnetic field B into a voltage signal U using a transfer function S . As from sensor theory, the transfer function $S = S(B)$ is itself dependent on the local magnetic field, as the sensor can be linear over a certain field range, and saturate for field values above a certain threshold. In a very general way, we can express the transducer function of the magnetic sensor by the equation $U = S(B) \cdot B$.

The Hall sensors presented in this thesis, as well as the magnetic microsensors discussed in section 2.2.5 are resistive elements. A sensing current

I_{meas} is passed through the sensing material of which the microsensor consists. Under the local magnetic field, the electrical resistivity of the material is modified (by physical effects introduced in sections 2.2.4 and 2.2.5) which leads to a variation of the sensor voltage U . Denoting the variation of the electrical resistivity induced by the magnetic field by $\rho_B(B)$, the sensor response can be expressed using Ohm's law:

$$U = \rho_B(B) \frac{l}{wt} I_{meas} \quad (2.22)$$

where l , w , t are the geometrical dimensions (length, width, thickness) of the sensing element. From this equation, we see that the sensor output of the resistive sensor is proportional to the measurement current I_{meas} . For this reason, the transfer function $S(B)$ is generally expressed as the current-corrected magnetic sensitivity $S_I(B) = S(B)/I_{meas}$ in units of Ω/T .

The function $S_I(B)$ is a continuous function of the applied field B and as such has a maximum, which lies around zero field or around a certain bias field in practice. In the case of the magnetic sensors introduced in the next sections, the sensors exhibit a field range over which $S_I(B)$ is constant (which corresponds to a linear sensor range). For high fields, $S_I(B)$ tends to vanish, as the sensor saturates. For this reason, we will discuss the field sensitivity $S_I(B)$ in term of the maximum field sensitivity $S_I = \max(S_I(B))$ in the following. S_I is given as the sensor signal U per magnetic signal B and measurement current I_{meas} :

$$S_I = \frac{U}{B \cdot I_{meas}} \quad (2.23)$$

The field sensitivity S_I is a constant and describes the ability of the micromagnetic sensor to transduce the magnetic field into an electrical signal at a certain measurement current I_{meas} . The higher S_I , the higher the voltage output from the sensor for a change in B .

Increasing the sensing current I_{meas} in equation (2.22) increases the output signal linearly. However, beyond a certain threshold, thermal heating of the sensor occurs and the measurement drifts. We call I_{max} the maximum DC current I_{meas} which can be passed through the sensor before thermal drift occurs. Therefore, the transfer function S has a maximum at $S_{max} = S_I I_{max}$.

S_I depends on the sensor geometry, as opposed to the magnetic resistivity $\rho_B(B)$, which depends solely on the sensing material. However, S_I is a generally accepted descriptor of the sensitivity of magnetic sensors and as such is used to compare the sensitivity to the magnetic field in the following sections.

Minimum detectable field

We now turn to a second figure of merit describing the ability of a microsensor to discriminate small magnetic field changes, which is the resolution of the sensor. Assuming noise-free amplification, the resolution of the sensor is ultimately limited by the noise generated in the sensor itself. The microsensors used for microbead detection are resistive sensors and as such subjected to different sources of electrical noise.

Electronic noise in sensors arises from various sources. Due to the quantum mechanical distribution of the charge carriers, in a AC current, a shot noise is measurable. When measuring at frequencies lower than a specific corner frequency, a $1/f$ noise of yet unknown origin is present. Finally, thermal noise (also referred to as *Johnson* noise) is generated by the thermal activation of the charge carrier in a conductor and is expressed using:

$$\frac{V_{thermal}}{\sqrt{\Delta f}} = \sqrt{4k_B T R} \quad (2.24)$$

where k_B is Boltzmann's constant, T is the temperature, R is the resistance of the conductor and Δf is the measurement bandwidth. Thermal noise depends on the resistance of the conductor and the temperature and represents the ultimate limit below which electronic noise cannot be minimized.

For this reason, the ultimate resolution of a micromagnetic sensor is limited by thermal noise. We introduce B_{min} as the minimum detectable field, corresponding to the magnetic field inducing a voltage response of amplitude corresponding to thermal noise, using the maximum allowable bias current I_{meas} :

$$B_{min} = \frac{V_{thermal}}{S_{max}} = \frac{\sqrt{4k_B T R \Delta f}}{S_I I_{max}} \quad (2.25)$$

Minimum detectable change in magnetic flux

We have introduced B_{min} as the sensor resolution, i.e. the minimum detectable change of magnetic field as seen by the sensor when operated in the white noise regime. However, we have seen in section 2.2.2 that the magnetic field generated by a microbead is highly inhomogeneous in space and that hence the magnetic field as seen by the sensor, B_{sens} is rapidly decreasing for increasing sensor width w . For this reason, we introduce a figure of merit taking into account the ability of the sensor to detect changes in the magnetic field of a highly *localized* dipole. The minimum detectable change in

magnetic flux Φ_{min} is given by:

$$\Phi_{min} = B_{min} \times A \quad (2.26)$$

where A is the active area of the sensor. Φ_{min} is the relevant figure of merit when discussing the detection of localized and close magnetic dipoles with a highly inhomogeneous field distribution on the Hall sensor active area, such as in the case of microbead detection using a micromagnetic sensor.

In the following, we introduce the Hall effect (section 2.2.4) and other physical effects used for microbead detection (section 2.2.5). A comparison of published microsensor results in terms of the introduced figures of merit is given in table 2.2.

2.2.4 The Hall effect in ferromagnetic materials

In this section, we introduce the Hall effect in matter. The *ordinary Hall effect* is general and present in any current carrying material subjected to a magnetic field. The *extraordinary Hall effect* is specific to ferromagnetic materials.

Ordinary Hall effect

When a current flows through a conductor placed in a magnetic field, the charge carriers are subjected to the Lorentz force, like any charge moving through a magnetic field:

$$\vec{F} = q(\vec{E} + \vec{v} \times \vec{B}) \quad (2.27)$$

where \vec{F} is the Lorentz force, q is the charge, \vec{E} is the electric field, \vec{v} is the charge carrier velocity and \vec{B} is the magnetic field. For $\vec{B} \perp \vec{v}$, equation (2.27) translates to $E - vB = 0$. Expressing the current density j as $j = nev$, with n being the number of charge carriers and e the elementary charge, one obtains $E = \frac{1}{nq}jB$. In the case of a square plate geometry of width w and thickness t , the voltage across the plate can be expressed as $U_H = wE$ and the current as $I_{meas} = jwt$. Thus, the current through the plate builds up a voltage given by:

$$\begin{aligned} U_H &= \frac{I_{meas}B}{tne} = I_{meas} \cdot B \cdot \frac{R_0}{t} = I_{meas} \frac{\rho_{OHE}}{t} \\ R_0 &= (ne)^{-1} \\ \rho_{OHE} &= R_0 \cdot B \end{aligned} \quad (2.28)$$

This effect is known as the *ordinary Hall effect* (OHE) [88]; accordingly, R_0 represents the ordinary Hall constant (in $\Omega\text{m}/\text{T}$) and ρ_{OH} the ordinary Hall resistivity (in Ωm). R_0 corresponds to the general resistivity change under magnetic field ρ_B introduced in section 2.2.3. As the ordinary Hall effect is generated by the Lorentz force, perpendicular both to the electrical current and the magnetic field, Hall sensors are sensitive only to the magnetic field B perpendicular to the Hall sensor surface. As the Hall effect is inversely proportional to the charge carrier density n , the ordinary Hall effect is pronounced in semi-conductors [89]. In a metal, the OHE is comparatively small.

Extraordinary Hall effect

In ferromagnetic materials, spin-orbit coupling leads to spin-dependent scattering of the charge-carriers which is proportional to the material magnetization. This gives rise to the *extraordinary Hall effect* (EHE) [90], also referred to as the *anomalous* or *spontaneous* Hall effect [91]. Consequently, in a ferromagnet the Hall effect can be separated into two distinct contributions [92]:

$$\rho_H = \rho_{OHE} + \rho_{EHE} = \mu_0(R_O H_z + R_S M_z) \quad (2.29)$$

where R_S denotes the extraordinary Hall coefficient and μ_0 is the free space permeability ($\mu_0=4\pi 10^{-7} \text{ m kg s}^{-2} \text{ A}^{-2}$). M_z is the magnetisation along the field direction and varies with the applied field H . While the ordinary Hall effect is classical, the spontaneous Hall effect is quantum mechanical in its origin [93].

The extraordinary Hall effect depends on the magnetization M of the sensor material and not on the field H [94]. Experimental and theoretical work have shown that the extraordinary Hall coefficient is linked to the longitudinal (electrical) resistivity ρ by:

$$\rho_{EHE} \propto \rho^n \quad (2.30)$$

where n is a factor accounting for the predominant scattering mechanism in the material. The factor n was measured to 1.94 for iron and 1.42 for nickel [95]. In the case of multiple scattering mechanisms involved, equation (2.30) is sometimes also expressed as [96]:

$$\rho_{EHE} = \alpha\rho + \beta\rho^2 \quad (2.31)$$

where α and β are coefficients corresponding to the scattering mechanisms involved [92, 97].

Table 2.2: Comparison of micromagnetic sensors used for single-bead detection. S_I is the sensitivity to the magnetic field as expressed in equation (2.23). B_{min} represents the minimum detectable field (equation (2.25)) and Φ_{min} is the minimum detectable change in magnetic flux (equation (2.26)). Φ_{min} is expressed in units of the magnetic flux quantum $\phi_0 = h/2e = 2.07 \times 10^{-15} \text{Tm}^2$. The sensor principles are Giant Magnetoresistance (GMR), Spin-Valve (SV), Planar Hall effect (PHE) and Hall sensors (Hall) (see section 2.2.5).

Reference	Type	Size μm^2	S_I V/AT	B_{min} nT/Hz ^{1/2}	Φ_{min}/Φ_0
[98]	GMR	0.15×2	8500	30	4×10 ⁻⁶
[99]	SV	2.5×80	20000	0.2	1.6×10 ⁻⁵
[100]	PHE	10×10	30	6	3×10 ⁻⁴
[101]	TMR	2×6	4000	50	3×10 ⁻⁴
[102]	TMR	2×15	7400	2.8	4×10 ⁻⁵
[102]	SV	2.5×40	6800	0.97	4.7×10 ⁻⁵
[103]	Hall	1×1	2750	51	2.5×10 ⁻⁵

The extraordinary Hall effect is the physical phenomenon behind the high sensitivity to the magnetic field of the novel Co:C material investigated in this thesis. As such, the extraordinary Hall effect is introduced in depth in Chapter 5, where the magnetic properties of our sensors are discussed.

2.2.5 Magnetic microsensors for single-bead detection

Micromagnetic sensors have widely been investigated for the detection of magnetic microbeads. As the magnetic moment of such particles is small, there have been several attempts to fabricate high-sensitivity, low-detection-limit sensors. In the following, we review the physical phenomena used to realise such devices.

Micro Hall sensors for bead detection applications

The challenge in realising micro Hall sensors lies in the judicious choice of an appropriate material and in the process of structuring this material in micrometric or near sub-micrometric dimensions. The straightforward way to do so is to use well-established photolithographic processes, as the semiconducting materials exhibit a high ordinary Hall resistivity. Using standard CMOS technology, Hall probes with dimensions of $2.4\mu\text{m} \times 2.4\mu\text{m}$ have been realised, exhibiting a sensitivity of 180V/AT and a magnetic field resolution

of 300nT at 1Hz [104]. CMOS Hall probes have successfully been shown to enable detection of single superparamagnetic microbeads [105]. Alternately, using sputtering and lift-off of Ni, sensors having an active area down to $1 \times 1 \mu\text{m}^2$ have been deposited on cantilevers, with a resolution of $1 \mu\text{T}/\text{Hz}^{1/2}$ in the thermal noise frequency range [106]. Taking advantage of the high Hall coefficient of Indium antimonide thin-films, another group patterned such a film by wet chemical etching, obtaining sensor dimensions of $5 \times 5 \mu\text{m}^2$, a sensitivity of 150V/AT and minimal field resolution of $150 \text{nT}/\text{Hz}^{1/2}$ [107].

Another approach lies in the structuration of metals, semi-metals or semi-conductors by focused ion beam milling (FIB). Active areas down to $100 \times 100 \text{nm}^2$ can be achieved by this technique [108]. Materials investigated so far include Gold and Gallium arsenide [108], Bismuth [109] and Indium antimonide [110]. The semiconductor-based Hall sensors show high sensitivity due to the lower charge carrier concentration in the material but exhibit a minimal detectable field around $1 \mu\text{T}/\text{Hz}^{1/2}$ due to contamination doping during the FIB processing. Single bead detection was shown using an InSb sensor structured by e-beam lithography [111].

Finally, fabrication of submicrometer Hall sensors by Focused Electron-Beam Induced Deposition (FEBID) was first investigated in 2005. Using a Cobalt carbonyl precursor, Hall devices with an active area of $300 \times 300 \text{nm}^2$ were deposited and characterised. A sensitivity of 0.9V/AT and a minimal field detection of $10 \mu\text{T}/\text{Hz}^{1/2}$ above 1kHz ($200 \mu\text{T}/\text{Hz}^{1/2}$ at 1Hz) was achieved, with some variance in both sensitivity and electric resistivity [20].

Planar Hall effect sensors

Planar Hall effect (PHE) sensors rely on the intrinsic magnetisation of the sensor material in a specific direction. They hence use ferromagnetic materials exhibiting a preferred direction of magnetisation. When a planar external magnetic field is applied, the sensor shows an anisotropic magnetoresistance (AMR), which means that the resistivity of the material is dependent on the angle between the measurement current and the intrinsic magnetisation [93]. The effect is the result of the electron's mean free path dependency on the angle between the electron's velocity and the magnetization of the material [79].

Planar Hall effect sensors have been investigated as a tool to detect the presence of superparamagnetic beads in biomolecular assays. Hall crosses with an active area of $20 \times 20 \mu\text{m}^2$ were made of Nickel, exhibiting a sensitivity of 7mV/T [112]. Deposition of $\text{Ni}_{80}\text{Fe}_{20}$ and subsequent patterning by ion-beam milling down to $10 \times 10 \mu\text{m}^2$ active area, yielded PHE sensors with a sensitivity of 30V/AT and a minimal field resolution of about $2 \mu\text{T}$

[87, 100]. Use of such sensors for bead counting in microfluidic chips was also investigated [113] and single-bead detection was shown [114]

Spin-valve sensors

Spin-valve magnetic sensors consist of two ferromagnetic layers separated by a spacer layer. One of the layers has its magnetisation pinned using an antiferromagnetic material deposited on top of it, whereas the second is left free to move with the measured external field [115]. The resistance then depends on the relative orientation of the magnetisation between the pinned and the free layer, as the charge carrying electrons travelling parallel to the stack have to reorient their spin upon scattering events, thus increasing the energy loss in conductance with increasing angle.

Spin-valve sensors have demonstrated their ability to detect single magnetic microbeads [99, 116–119] in biosensor applications [120, 121]. Sensitivity reaches values up to 16kV/AT, with a resolution limit of 10nT [122]. While those sensors thus have a very high sensitivity and high resolution, their relatively low saturation value (some mT) prohibits their use in combination with a high external magnetic field such as that produced by magnetic tweezers.

Giant Magnetoresistance sensors

The giant magnetoresistive effect (GMR) is based on antiferromagnetic coupling between magnetic layers separated by thin spacer layers [49]. By tuning the layer thicknesses, the resistance becomes strongly dependent on the relative orientation of magnetisation between the layers, as the spin-polarised current can only be accepted into bands of identical spins in adjacent layers.

Sub-micron GMR sensors were obtained by e-beam lithography and etching of commercially available GMR multilayers. They showed a sensitivity of about 6.5kV/AT, a saturation field of 30mT and widths down to 100nm. However, due to structural changes during the etching process, the setup is rather noisy with a minimal resolution of 12 μ T/Hz^{1/2} [98]. Single-bead detection of 1 μ m superparamagnetic beads was presented using a 3 μ m-wide GMR strip [123], as well as bead-counting with smaller (300nm) beads [124].

Magnetic tunnel junctions

Magnetic tunnel junctions (MTJ) are based on the tunnel magnetoresistance (TMR) effect [125]. Two ferromagnetic layers are separated by a thin layer (in the scale of a few nanometers), which consists of an *insulating* material (in contrast to GMR-based sensors, where the spacer layer is conducting and

serves the purpose to tune the magnetic coupling into an antiferromagnetic state). Electrons can tunnel through the insulating barrier, but the probability they do is highly dependent on the relative alignment of the magnetization in the two ferromagnetic layers. The junction hence exhibits a strong resistive response to the magnetic field. Single-bead detection using MTJ has been demonstrated in [101]. Saturation fields as high as 50mT for sensor sizes as low as $400 \times 100 \text{nm}^2$ were achieved [126].

Chapter 3

Experimental setups

3.1 Focused particle beam processing and characterisation

3.1.1 Electron microscope Hitachi S-3600

Focused electron beam induced deposition was carried out inside a Hitachi S-3600 electron microscope (see figure 3.1). The microscope is equipped with a tungsten filament. Acceleration voltage range is 0.5 to 30kV. At $E_0 = 25\text{keV}$, beam currents of up to 12nA were achieved. A picoammeter (Keithley Instruments 6485 picoammeter) connected to the stage was used in conjunction with a home-made Faraday cup on the sample holder in order to measure the beam current. During processing on the chip, the picoammeter was used to monitor the evolution of the beam current [127]. The beam full-width at half maximum (FWHM) was calibrated at different excitation energies and beam currents under best-focus conditions using BeamMetr [128].

The S-3600 was operated in high vacuum (HV) mode, provided by an oil diffusion pump backed by a rotary roughing pump. Background pressures down to 5×10^{-6} mbar were routinely obtained.

A lithography system (XENOS XeDraw 2, XENOS Semiconductor Technologies GmbH, Stuttgart, Germany) was attached to the SEM, allowing to scan the beam in arbitrary geometries and velocities on the substrate. This system was used for the definition of the deposit's shape in focused electron-beam induced deposition. The minimum dwell time was 250ns. A beam blanker unit placed in the electron column was accessible by the lithography system, allowing to define arbitrary refresh times.

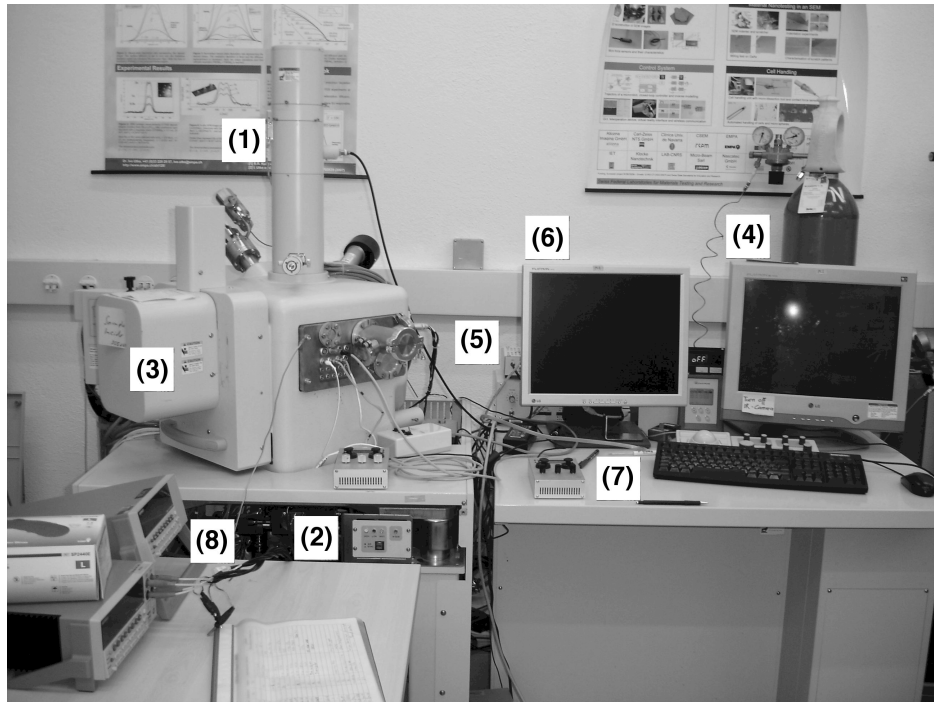


Figure 3.1: *Electron microscope Hitachi S-3600. (1) Electron column. (2) Vacuum unit with oil diffusion pump. (3) Sample tray. (4) SEM PC. (5) Lithography system. (6) Lithography PC. (7) 3-axis piezo control for gas injection system (GIS). (8) Picoammperemeter for stage current monitoring.*

3.1.2 Gas injection system

A home-made gas injection system (GIS) was mounted in the SEM main chamber in order to controllably deliver a reproducible flux of precursor molecules onto the substrate surface. The GIS is depicted in figure 3.2. A three-axis piezo actuator (SmarAct GmbH, Oldenburg, Germany) was used to approach the GIS to the substrate with nanometer precision. Using these actuators and vision feedback, the nozzle was positioned $100\mu\text{m}$ in horizontal and $\approx 50\mu\text{m}$ in vertical direction from the sample. Contact between the GIS and the sample were both monitored using imaging feedback from the SEM and as a leakage current on the substrate-connected picoammeter. The GIS itself consists of a 5mm long, $600\mu\text{m}$ diameter nozzle directed at an angle of 35° to the substrate. A metal tubing connects the nozzle to an in-chamber Teflon reservoir used for solid and some low-vapour pressure liquid precursors. High vapour pressure liquid precursors could be connected by means of a vacuum feedthrough connected to a flexible silicon tube fitted to the GIS nozzle head. Individual sets of GIS components were used for each precursor in order to avoid contamination.

For FEBID of Co-C material, the precursor Dicobalt-octacarbonyl ($\text{Co}_2(\text{CO})_8$, CAS number 10210-68-1, Merck Chemicals) was used. $\text{Co}_2(\text{CO})_8$ is a dark-red polycrystalline solid with a vapor pressure of about 10 Pa at room temperature [52]. Cobalt carbonyl decomposes thermally at 52°C [56]. Due to its sensitivity to humidity, the precursor was filled into the reservoir inside a glove-box. As $\text{Co}_2(\text{CO})_8$ is known to spontaneously decompose to tetracobalt-dodekacarbonyl $[\text{Co}(\text{CO})_3]_4$ [56]. For this reason, it is usually stored in an hexane atmosphere. However, this proved to be a source for unwanted carbon co-deposition during FEBID. For this reason, $\text{Co}_2(\text{CO})_8$ stabilized in an Ar atmosphere was used.

The precursor flux was estimated from mass loss measurements. They are reported in figure 3.3. The flux appears to be constant in the time frame used for experimentation (30-300 minutes). The hexane-stabilized precursor however results in a much higher apparent precursor flux, which we attribute to a substantial hydrocarbon flux leaving the reservoir.

To estimate the effective precursor flux impinging on the deposition locus on the substrate, the precursor flux at the nozzle exit and the nozzle-substrate geometry was fed into a Monte-Carlo simulation software [129]. Roughly, the surface impinging flux at the point of irradiation was found to correspond to 1/10 of the molecular flux at the nozzle exit.

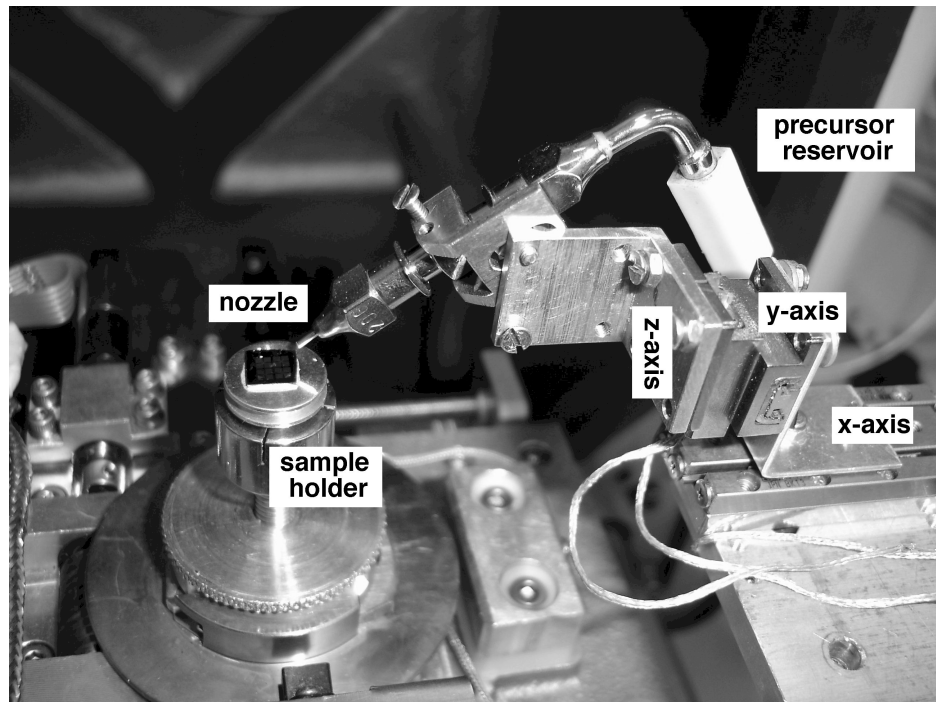


Figure 3.2: Gas injection system used for FEBID experiments. A three-axis piezo slip-stick actuator provides positioning decoupled from the stage. Nozzle inner-diameter was $600\mu\text{m}$.

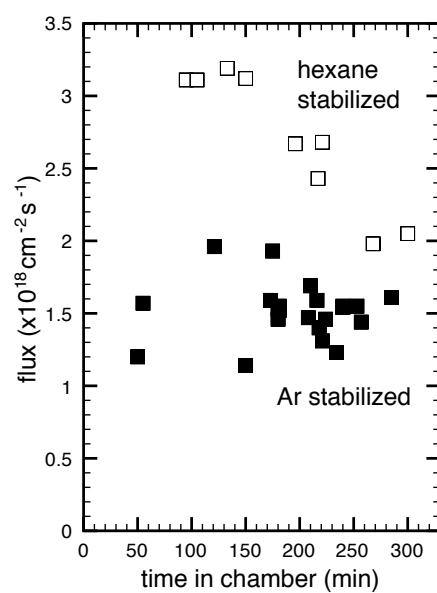


Figure 3.3: Precursor fluxes at nozzle exit versus time in SEM chamber, for hexane- and Argon-stabilized $\text{Co}_2(\text{CO})_8$. The fluxes are estimated from mass loss measurements. The nozzle inner-diameter was $600\mu\text{m}$.

3.1.3 Tescan dual-beam microscope

For focused ion-beam processing, a Tescan dual beam Lyra microscope was used (figure 3.4a). The microscope is equipped with a FEB and a FIB at an angle of 55° , allowing imaging of the ion-induced surface changes (deposition, milling) using the electrons. The electron source is a tungsten-filament. A liquid Ga source is used for the ion beam. The ion beam was operated at 30keV, and the ion current was tunable between some pA and several μA . A 6-sample rotary sample revolver allowed parallel treatment of several samples. The tescan dual-beam microscope was operated in HV conditions, using a turbomolecular pump to reach chamber pressures of 10^{-6} mbar routinely.

An in-house gas injection system similar to the one described above for FEBID was mounted inside the chamber to allow Focused Ion Beam Induced Deposition (FIBID) (figure 3.4b). Gas feed-throughs allowed the use of high-vapour pressure, liquid precursors. Beam control was provided through the manufacturers proprietary lithography interface (DrawBeam, Tescan, Czech Republic), with nominal dwell times down to 80ns. We also used the ion-beam in the absence of precursor gases. The focused ion beam was used to mill away superfluous material, in order to reduce the dimensions of the structures down to 100nm.

3.1.4 Electron microscope Hitachi S-4800

A high-resolution Hitachi S-4800 SEM was used for the characterization of the deposits. A cold-cathode field emission gun (FEG) allowed for high-resolution SEM. The microscope is equipped with an EDX-detector allowing chemical analysis of the deposits.

3.1.5 Atomic force microscope Topometrix Explorer

For the assessment of the deposit height, an atomic force microscope was used. The Topometrix Explorer was operated both in contact and non-contact mode. The $100\mu\text{m} \times 100\mu\text{m} \times 12\mu\text{m}$ x/y/z-piezo scan unit allowed imaging of broader structures while providing a nanometric z-resolution as assessed by measurements on a calibration sample. Data treatment was done using the software WSXM [130].

3.2 Lithography

Gold electrodes providing electrical contact to the subsequent FEB induced deposits were fabricated on Si/SiO₂ substrates by conventional lithography,

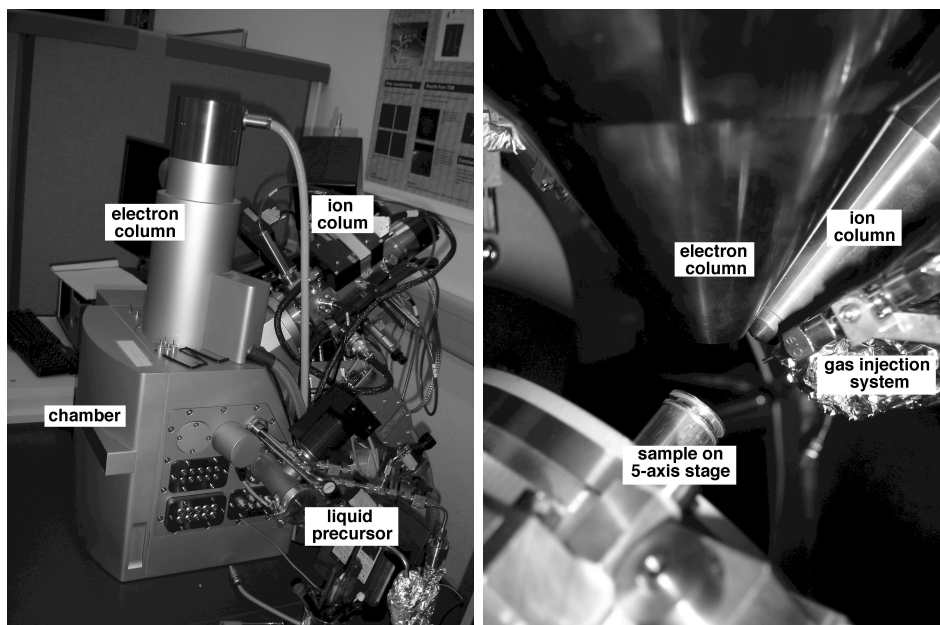


Figure 3.4: *Tescan Lyra Dual Beam Microscope (left) and in-chamber view showing the configuration of the electron column, the ion column, the gas injection system and the sample.*

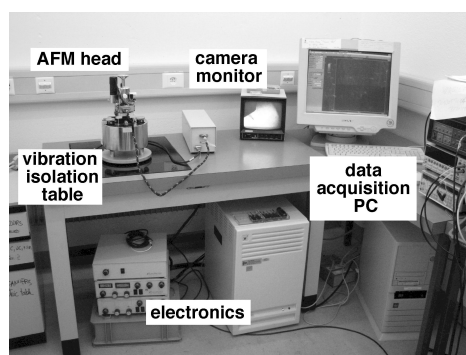


Figure 3.5: *Topometrix Explorer AFM setup. The AFM can be operated in both non-contact and contact mode.*

sputtering and lift-off. The process flow is shown in figure 3.6. A two-step process was implemented, using optical lithography to define the contact pads and electron beam lithography (EBL) to structure gold electrodes only 1-2 μm apart.

First, a Si wafer with a 200nm thermal oxide layer was diced to 7 \times 7mm² chips. The chips were cleaned in acetone and isopropanol and blown dry using nitrogen. Optical lithography was applied to define 2 \times 2mm² contact pads. To this mean, a sandwich layer PMMA/SU8 was spin-coated onto the chips, where the PMMA layer way used as a contact layer to ease the subsequent lift-off and the negative SU8 resin was the optically sensitive layer. Exposition was carried out using a commercial 14 μm resolution UV exposure system. After development, physical vapour deposition (PVD) was used to sputter a 10nm Cr or Pt / 150nm Au bilayer, where the Cr or Pt was used as a contact layer. Finally, the structures were lifted off in a acetone bath.

In a second step, EBL was carried out in a Hitachi S-3600 to structure electrodes convergent to a single point on the substrate, with a gap of 1-2 μm between. The positive PMMA resin was applied on the chip and the openings to be dissolved were irradiated using a 25keV, 100pA-1nA electron beam. After development, a second PVD step was carried out. Lift-off allowed to free the structured electrodes. The resolution for this step was in the order of 600nm.

3.3 Electrical and magnetic characterisation

For the electrical characterisation, a Keithley 2400 SourceMeter was used to measure the deposit resistance in both 2-point and 4-point mode. For the Hall sensors, the lithographically defined electrodes allowed only 2-point measurements. However, we conducted separate measurements on dedicated 4-point electrodes interconnected by a FEB induced deposit and determined the contact resistance to be in the order of 20 Ω , which compares to a deposit resistance of $\geq 100\Omega$ for all Hall sensors investigated. For this reason, we assume the error induced by the use of 2-point measurement for the resistance is limited to $\leq 20\%$.

The magnetic characterisation was carried out at EPFL in the microsystems design group. The Hall sensors were mounted on a specially designed PCB and mechanically positionned in the gap of a high-power magnetic coil delivering DC fields in the -2T/+2T range. The Hall sensor was biased using a voltage source and the Hall voltage was recorded at constant current as the DC field was swept.

The FEB induced deposits have sizes in the micrometer range and need

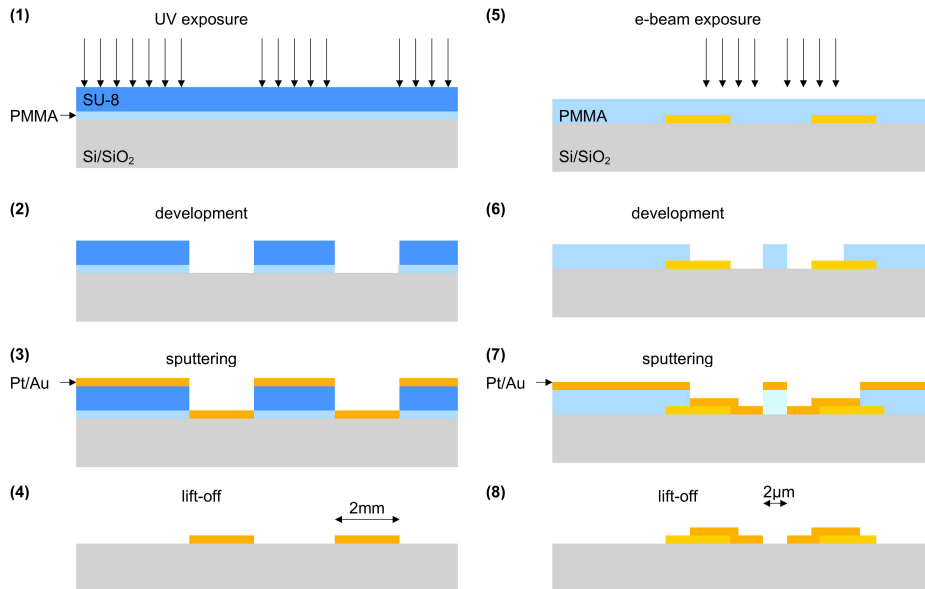


Figure 3.6: Operation flow for the lithographic structuration of Au electrodes for subsequent FEBID of CoC Hall sensors. A two-step process was implemented, allowing the rapid structuration of macroscopic $2 \times 2 \text{ mm}^2$ pads (UV lithography, steps 1-4) while providing fine electrodes only $2 \mu\text{m}$ apart in the center of the structure (e-beam lithography, steps 5-8).

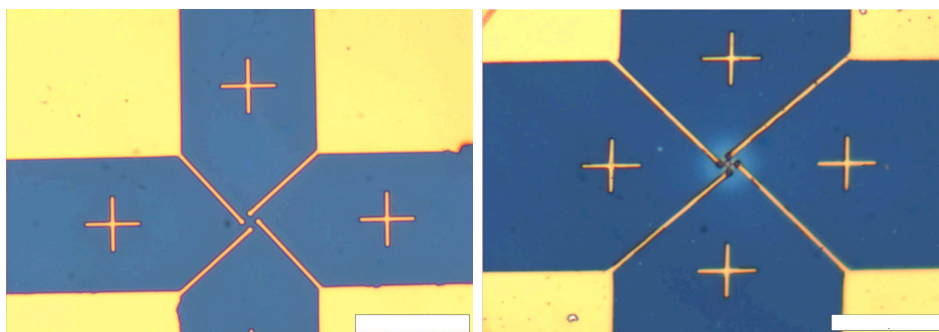


Figure 3.7: a) Lithographically structured Si/SiO₂ chip ready for FEBID. b) The same structure with a FEBID CoC Hall sensor deposited. Optical images, scale bar $20 \mu\text{m}$.

to be hooked up to the measurement instruments. To this end, the deposits were realized on top of lithographically structured gold electrodes, providing pads of $50 \times 50 \mu\text{m}^2$. The $7 \times 7 \text{ mm}^2$ Si/SiO₂ chips were then glued on leadless chip carriers (LCC) and electrical connection to the lithographic pads was realized using a wire-bonding setup. The LCC were then connected using a homemade printed circuit board allowing contact through a DB-25 connector. For all measurements, greatest care had to be taken to prevent the destruction of the deposits by electrostatic discharge (ESD). To this end, a switch-box was designed allowing to ground the electrical connections to the sensor while connecting the characterization instruments. At the same time, the switch box allowed to address the on-chip deposits individually (up to four). The entire setup is depicted in figure 3.8.

The Keithley 2400 SourceMeter is a two-point/four-point terminal resistance measurement instrument. It can be operated both in voltage and current source mode. The response is measured as a voltage drop or current either through two different connections, allowing four-point measurement, or through the sourcing connections, in the case of two-point electrical characterisation. Using a GPIB hardware interface in conjunction with a homemade VisualBasic user interface, automatic data gathering was implemented.

3.4 Bead detection setup

A novel method of superparamagnetic bead detection is implemented (figure 3.9). To this end, a magnetic coil (radius 3cm) was integrated in the chamber of an SEM. In the axis of the coil, the Hall sensors were mounted using a PCB with an integrated chip carrier. The magnetic excitation field was hence perpendicular to the sensor surface. In order to increase the magnetic excitation field at the position of the sensor, a high permeability, low-remanence core (E450-40, MicroMetals) was placed inside the coil. A power amplifier (Hero PA508X power amplifier, Rohrer Munich), driven at a frequency of 17.3Hz set by a waveform generator (Hewlett-Packard 33120A), was used as a current source. Using a current of 2A, a field of 12mT could be created at the sensor's location.

The setup provided a mean to place a superparamagnetic bead at an arbitrary position with respect to the micromagnetic sensor. This was possible by the integration of an AFM cantilever attached to a three-axis piezo actuator (SmarAct GmbH, Oldenburg, Germany). The actuator has a nanometric step resolution. However, in practice, visual feedback is limited to about 100nm due to the non-zero remanence of the magnetic core. Hence, the movements of the nanomanipulator were calibrated before using

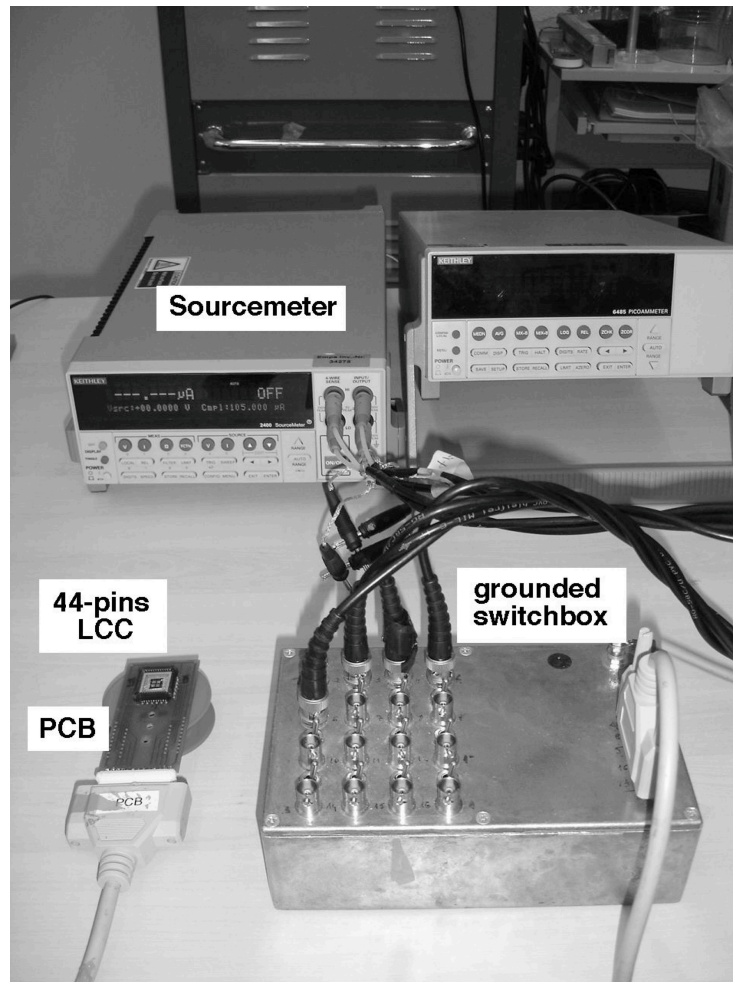


Figure 3.8: Setup used for *ex-situ* electrical characterisation and *ex-situ* bead detection, consisting of a LCC, a home-made PCB, a grounded switchbox and the Keithley 2400 SourceMeter. For bead detection, a DC magnetic field was generated below the PCB using bar magnets, an AC magnetic field was generated above the PCB using a homemade coil and the SourceMeter is replaced with a LockIn amplifier working at the AC magnetic field frequency.

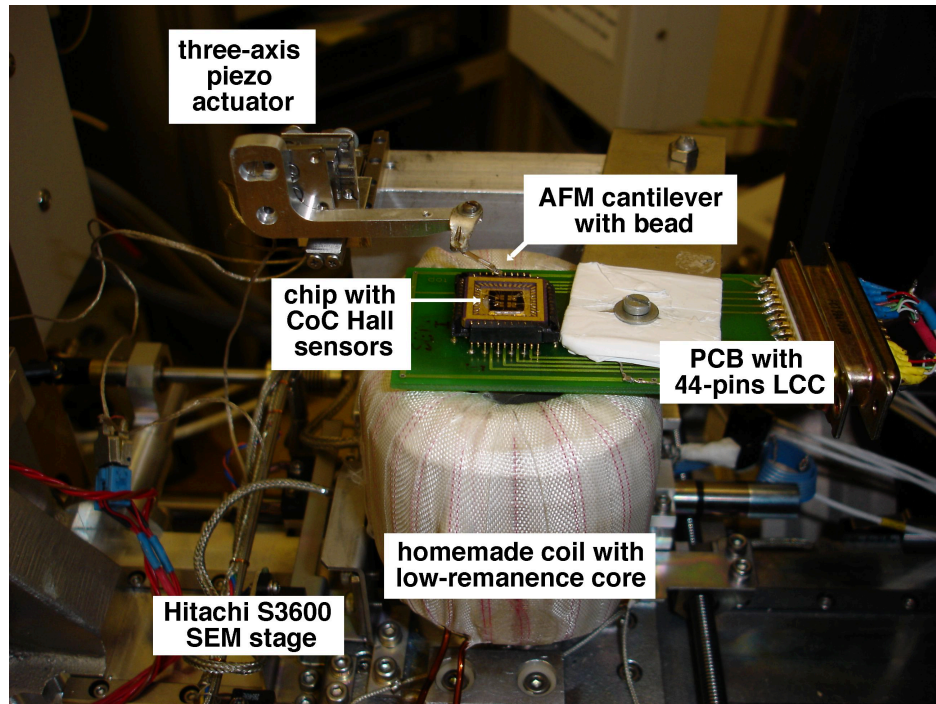


Figure 3.9: *Setup used for in-situ bead detection.*

the magnetic field.

The AFM tip (NSC15 non-contact cantilever, MikroMasch, spring constant 40N/m) was used to pick up a single microbead and to position it freely with respect to the sensor. A non-contact cantilever was chosen as it had to exhibit a certain rigidity not to be deflected when scanning over the microbeads. The in-situ nanomanipulation is shown in figure 3.10.

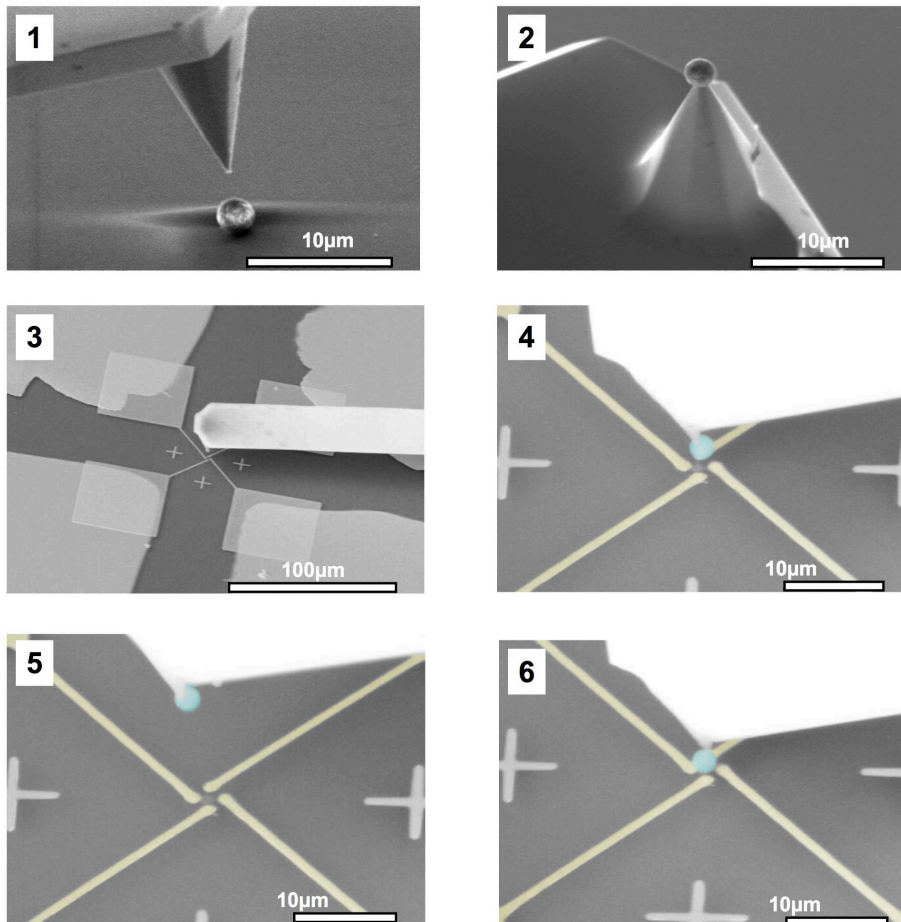


Figure 3.10: *In-situ bead placement for detection, as seen using the imaging capabilities of the SEM. The insitu detection setup is tilted by 40° with respect to the beam axis. 1) The AFM tip is approached close to the microbead. Using nanomanipulators, physical contact is made. By electron irradiation of the contact, FEBID of chamber background hydrocarbons “solder” the bead to the AFM tip. 2) View of bead fixed on AFM tip. 3) In-situ nanomanipulation with electrically contacted CoC FEBID Hall sensor and AFM tip. 4) Using nanomanipulation, the microbead can be approached towards the sensor or 5) retracted. 6) The bead is placed directly on top of the sensor.*

Chapter 4

Tuning the composition of nano-composite Cobalt-Carbon deposits

In this chapter, we show that the composition of deposits realized by FEBID of $\text{Co}_2(\text{CO})_8$ in high vacuum chambers can be tuned from 20at.% to 70at.% using a variation of the pulse time of a pulsed electron-beam. The experimental data can be described theoretically by using a novel, analytical model of FEBID in the presence of two adsorbate species. We show that the relative surface adsorbate densities can be varied by the process parameters, allowing to tune the outcome of the FEBID process. The general conditions for this tunability are presented. The model is applied to our experimental case consisting of $\text{Co}_2(\text{CO})_8$ and background chamber hydrocarbons. The experimental data is found to be in excellent agreement.

4.1 Introduction

It is known that focused electron beam induced deposition performed in high vacuum (HV) microscope chambers suffers from co-deposition of background pressure ($p \approx 10^{-6}$ - 10^{-5} mbar) hydrocarbons [21]. The injected functional precursor gas molecule, often a metal-organic or metal-inorganic compound, physisorbs together with the hydrocarbons on the substrate surface where *both* molecules are dissociated by the focused electron beam. This is the reason why carrying out FEBID in UHV environment [35] or doing pre-deposition plasma cleaning of the surface in order to remove surface-adsorbed hydrocarbons [131] have been identified as pathways to increase the metallic concentrations in the deposits. Also, with the use of recently developed

gas injection systems which allow the admission of two (or more) gases to the substrate surface [36, 132], there is a need for an analytical description of dual adsorbates FEBID model. This is especially important in light of the fact that in certain cases, it is preferable to deposit a *composite* metal-carbon nanostructure having the magnetic metal embedded as nanocrystals in a carbonaceous matrix serving for mechanical stability and as oxidation barrier in ambient or liquid atmospheres, for instance in magnetic scanning probe applications [38, 57]. Beside the mechanical properties, nanocomposite materials are known to have remarkable magnetic sensing properties that can be exploited in sub-micron, high-sensitivity Hall sensors, as this material exhibits a large extraordinary Hall effect (EHE) [20, 97]. A precise control of the outcome of the FEBID process is thus required, as it dominantly influences the magnetic sensing properties of the deposit (see Chapter 5).

This is why we present a study of the deposition process in planar deposits obtained from dicobalt-octacarbonyl ($\text{Co}_2(\text{CO})_8$). We find metallic concentrations that can be controlled between 20 and 70 at.% during the same experiment. In [18, 19, 37, 62], Co concentrations in deposits from electron dissociation of $\text{Co}_2(\text{CO})_8$ between 35at.% and 97at.% are reported, obtained in different experiments and with different beam currents. The differences are usually attributed to thermal effects by local electron-beam induced heating [18]. The importance of temperature-induced purification during the deposition process is highlighted in [65], where FEBID of Cobalt was carried out on a heated substrate, showing a close correlation between substrate temperature and deposit purity. In our case however, for low beam currents ($\leq 1\text{nA}$), Si covered by 200nm of thermally grown SiO_2 as a substrate and for planar deposits, MC simulation of electron-beam heating effects predict negligible local heating.

This is the motivation to take into account co-deposition of hydrocarbons present in the chamber background and to analytically model how the presence of two adsorbates will influence the deposition process in comparison to the one-adsorbate process described in Section 2.1.3. We find that the developed model allows for a quantitative explanation of the Co:C ratio found in the FEB induced deposits.

It must be noted that while the deposition of cobalt-containing pillars, where the electron-beam is constantly illuminating a single spot on the substrate, has been investigated in depth [18, 37, 39], the study of the linear or planar deposition of Cobalt, where the beam is raster scanned over a certain area, has only recently emerged [62–65].

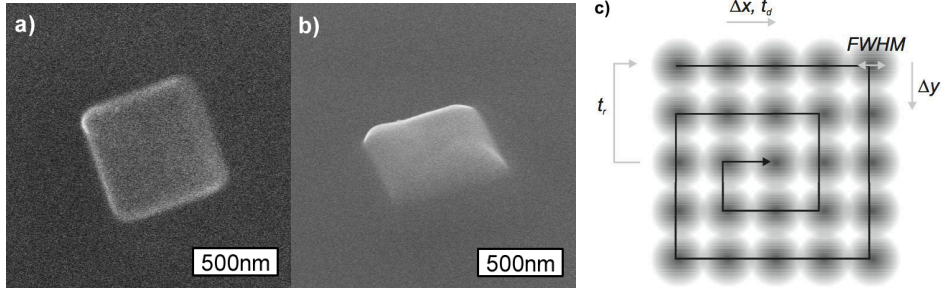


Figure 4.1: a) SEM images of 600nm square $\text{Co}_2(\text{CO})_8$:hydrocarbon deposit in top view and b) tilted (45°) view. c) Deposition strategy. The rectangular deposits are realized using a serpentine deposition path. Δx and Δy denote the increment in x and y direction and are identical throughout the experiments. Each pixel is irradiated for a dwell time t_d . The refresh time is the time elapsing between to subsequent irradiations of the same pixel and is given by the multiplication of the number of pixels with the dwell time.

4.2 Experiment

In the equipment described in chapter 3, FEBID of squares of dimensions $3 \times 3 \mu\text{m}^2$ and $600 \times 600 \text{nm}^2$ has been carried out from the precursor $\text{Co}_2(\text{CO})_8$ (see figure 4.1a,b). Silicon chips of roughly 1cm^2 with a 200nm-thick thermally grown SiO_2 layer were used as a deposition substrate. Before deposition, the substrate was cleaned in acetone, rinsed with propanol and blown dry using nitrogen.

The precursor was delivered by means of our home-made GIS. The precursor flux during the experiments was about 4.4×10^{15} molecules/s, as estimated from mass loss measurements. According to our gas flow MC simulations [129], this translates into $1.5 \times 10^{17} \text{cm}^{-2} \text{s}^{-1}$ impinging on the FEB irradiated spot. The operating pressure was $\sim 2 \times 10^{-5}$ mbar and the residual chamber pressure during deposition was $\sim 1 \times 10^{-5}$ mbar, as estimated from the pump time of the chamber (see figure 4.2a). The composition of the chamber background was measured by a residual gas analyzer (RGA) and is shown in figure 4.2b.

We used the XENOS lithography system to control the electron beam during deposition. The deposition control parameters are the nominal pulse duration t_d , i.e. the time the beam irradiates a pixel before moving to the next, the inter-pixel distance Δx , defined as the distance between two adjacent irradiated pixels, and the refresh time t_r , which measures the time elapsed between two exposition iterations (see figure 4.1c). Dividing the to-

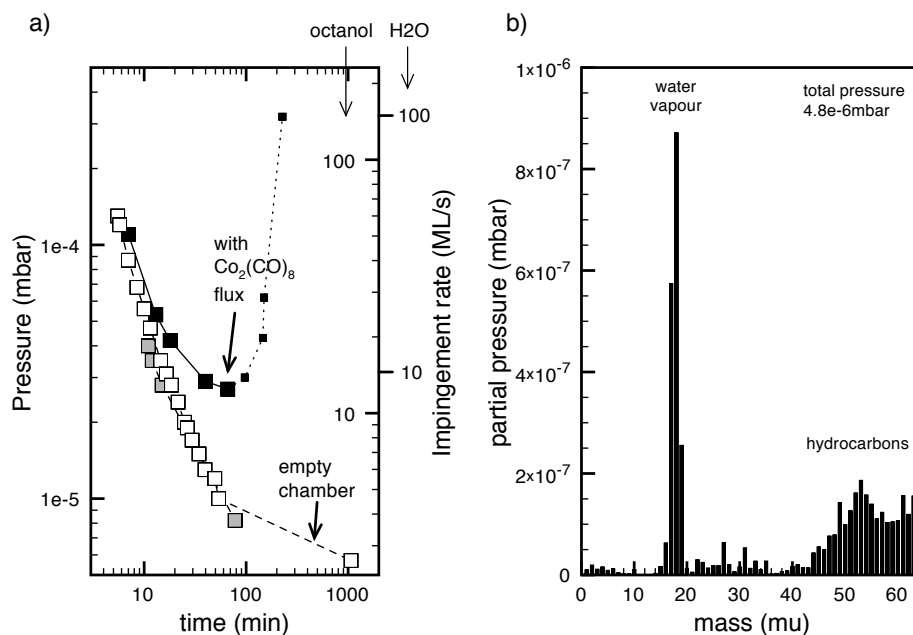


Figure 4.2: a) Evolution of the chamber pressure (as obtained by a 570l/s oil-diffusion pump) with pump time, measured by a Penning-type cold cathode ionization gauge. Empty squares indicate the values for the empty chamber, grey squares the values for the chamber with the GIS installed. Full squares indicate the pressure evolution in the presence of the precursor vessel inside the chamber, while a flux of $\text{Co}_2(\text{CO})_8$ is delivered by the GIS. Long-time measurement in this case is prevented by the deposition of Cobalt inside the ionization gauge, leading to erratic vacuum measurements (small squares). The right-hand axis gives the estimated impingement rate in monolayer per second [133], under the assumption that the residual gas is mainly water vapour or mainly octanol ($\text{C}_8\text{H}_{17}\text{OH}$). b) Composition of the background of the experimental SEM chamber used for deposition, in the absence of any precursor, as measured by a residual gas analyzer (RGA).

tal irradiation time by the total exposed surface yields the total deposition dose in C/cm^2 . In our experiments, squares with lateral dimensions of $3\mu\text{m}$ and 600nm were deposited with a constant total deposition dose of $10\text{C}/\text{cm}^2$ and the dwell time was varied over two orders of magnitude (500ns to $50\mu\text{s}$). The refresh time was always kept $\geq 10\text{ms}$, to ensure full replenishment with precursor molecules between two irradiation iterations, taking $\tau \approx 1\text{ms}$ as a typical surface residence time [15]. Actual refresh times are given in table 4.1, assessing full precursor replenishment during the refresh time. The inter-pixel distance Δx was set to 30nm . This compares to a beam diameter (FWHM) of 70nm assessed experimentally using BeamMetr [128] for the acceleration voltage (25kV) and beam current (1nA) used. Accordingly, a given location on the substrate is irradiated by two consecutive pixels (i.e. the beam overlap is 2), and the effective dwell time is the double of the nominal dwell time. The total irradiation time per pixel is then the double of the effective dwell time, as the overlap is present in both x- and y-direction.

The deposits were characterized with regard to the composition using energy dispersive x-ray spectroscopy (EDX) at 3keV . The accuracy of the compositional values obtained by this mean was checked to be correct within $\pm 5\text{at.}\%$ by calibration measurements on Cobalt-carbonate (CoCO_3). The height of the deposits was assessed by atomic force microscopy (AFM).

4.3 Experimental results

4.3.1 Composition

The metallic concentration of the deposits is found to be highly dependent on the dwell time for 600nm squares, as shown in figure 4.3. For dwell times below $1\mu\text{s}$, Cobalt concentrations as low as $20\text{at.}\%$ are found, while dwell times of $20\mu\text{s}$ or more yield deposits with above $60\text{at.}\%$ Cobalt. In contrast, $3\mu\text{m}$ square deposits show a constant Cobalt concentration of $60\text{--}70\text{at.}\%$ independently of the dwell time used.

The balance of the composition contains Oxygen and Carbon. For the 600nm squares, the Carbon content scales inversely with the Cobalt content, decreasing from about $70\text{at.}\%$ for dwell times of 500ns down to $22\text{at.}\%$ for dwell times of $50\mu\text{s}$, whereas the Oxygen level remains stable at around $18\text{at.}\%$. For the $3\mu\text{m}$ squares, the Oxygen level remains stable within the measurement error at around $15\text{at.}\%$ and a Carbon level of about $20\text{at.}\%$ is found.

The EDX measurements were performed by focusing a 3keV electron beam on the center of the deposit, so that the escape cone for the X-rays has

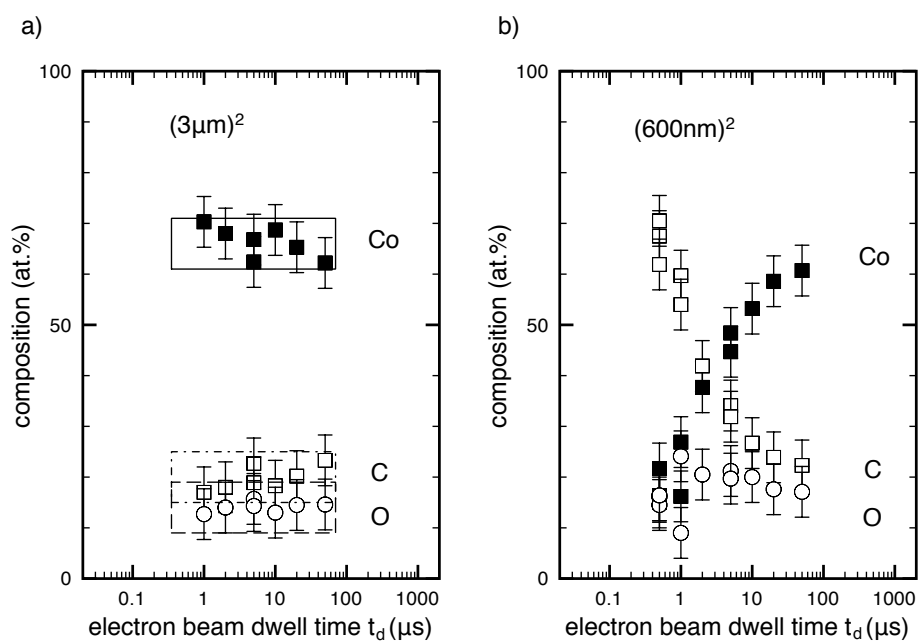


Figure 4.3: Composition of the $(3\mu\text{m})^2$ and $(600\text{nm})^2$ deposits as measured by EDX for varying dwell times. Within measurement uncertainty, the composition of the deposited compound for the $3\mu\text{m}$ squares does not depend on the dwell time and is $\text{Co}_2\text{C}_{0.6}\text{O}_{0.4}$ (shown as rectangles).

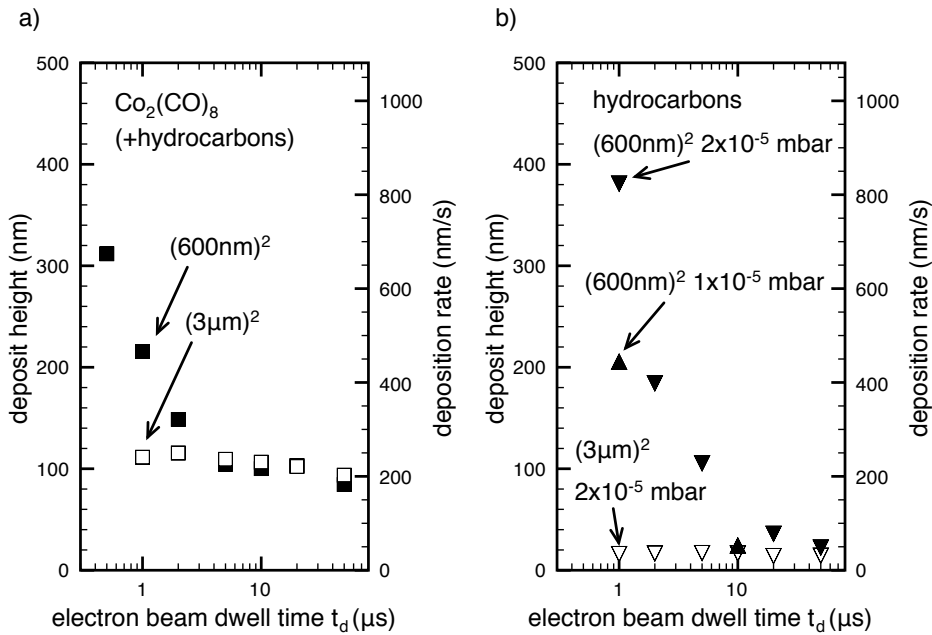


Figure 4.4: Heights of the investigated deposits. Left: $(600\text{nm})^2$ (full squares) and $(3\mu\text{m})^2$ (open squares) $\text{Co}_2(\text{CO})_8$ deposits. Right: $(600\text{nm})^2$ (full triangles) and $(3\mu\text{m})^2$ (open triangles) deposits from chamber background hydrocarbons. The hydrocarbon deposition was performed at 2×10^{-5} mbar (upwards pointing triangles) and 1×10^{-5} mbar (downwards pointing triangles). The deposit heights are measured by AFM and are taken in the center of the deposit in order to avoid edge effects. All deposits were realized at the same electron dose of $10\text{C}/\text{cm}^2$.

a radius of well below 50nm. Thus, the discrepancy in the concentrations found for the 600nm squares cannot be attributed to edge effects during the measurement. Also, the height of the deposits characterized by EDX was higher than the penetration depth of 50nm, so that there was no influence of the substrate on the measured value.

4.3.2 Deposition rates

The deposit heights are reported in figure 4.4. The corresponding deposition rates are obtained by dividing the heights by the total irradiation time per pixel, as defined in the experimental section. As the total irradiation time per pixel, the beam current and the beam diameter are constant throughout all experimental series, the deposition rates are proportional to the deposit heights. For the $600 \times 600\text{nm}^2$ squares, the deposition rates are found to

increase strongly for low dwell times (below $5\mu\text{s}$), and are nearly constant for dwell times above this threshold. For the $3\times 3\mu\text{m}^2$ squares, deposition rates decreasing slightly with dwell time are found for all dwell times investigated.

As a reference, the hydrocarbon deposition rates, obtained by depositing $600\times 600\text{nm}^2$ squares *in the absence* of $\text{Co}_2(\text{CO})_8$ precursor, are shown, for background pressure of 1 and $2\times 10^{-5}\text{mbar}$. A strong dependency on the dwell time is found in this case throughout the investigated dwell time scale. Intuitively, the absolute value of the deposition rate (at comparable dwell time) is found to be dependent on the background chamber pressure, i.e. on the amount of hydrocarbon “precursor” available for the deposition process. Comparable measurements for $3\mu\text{m}$ squares gave approximatively constant deposition heights of 30nm in the center.

In figure 4.4, it can be seen that the thickness of $(600\text{nm})^2$ deposits from $\text{Co}_2(\text{CO})_8$ presents similarities with hydrocarbon dissociation for low dwell times (high dependency on dwell time) and stabilizes for high dwell times at values comparable to $(3\mu\text{m})^2$ $\text{Co}_2(\text{CO})_8$ deposits. We propose that this behaviour is due to co-deposition of both Cobalt carbonyl and background pressure hydrocarbons, which reach the dissociation spot from gas phase and by surface migration.

4.4 Analytical two-adsorbate model

The deposition rate model in the presence of a single species of substrate adsorbate under focused electron-beam irradiation was introduced in section 2.1.3. The same formalism and notations are used throughout this section.

In order to model the change of composition with the exposure parameters, we introduce the following generic electron-impact reactions of the two adsorbate species A and B :



Here, D_A and D_B are the non-volatile, deposited reaction products, whereas V_A and V_B represent the volatile reaction products which desorb to the vacuum.

4.4.1 Deposition rates in the two-adsorbate model

We start to model surface adsorbate densities in the generic case where two adsorbate species A and B are present. The principle of co-deposition is shown

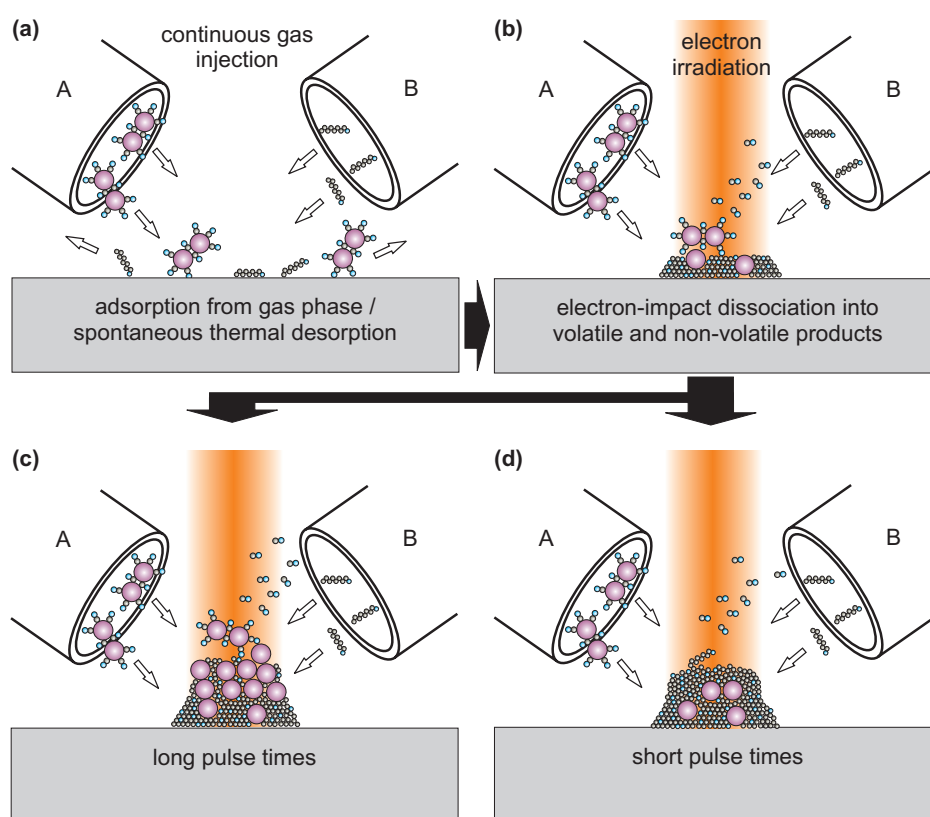


Figure 4.5: Schematic representation of the two-adsorbate model. (a) Before irradiation, competitive adsorption from the gas phase leads to an equilibrium surface density of both molecules according to their individual supply and desorption rates. (b) Upon electron irradiation, the molecule with the larger electron-impact dissociation cross-section is preferentially dissociated, say molecule B, and a B-rich deposit forms. Consequently, the adsorbate equilibrium shifts to A-rich. (c) If electron exposure continues an A-rich deposit is obtained. (d) If exposure is interrupted, the initial adsorbate equilibrium re-establishes leading to a B-rich deposit upon the next exposure pulse. From [134]

in figure 4.5 and starts from the assumptions that both molecules reversibly co-adsorb and that electron-impact dissociation of each adsorbate species leads to deposition during an electron beam exposure pulse. Analytically, in the presence of two precursors, competitive adsorption can be modelled using the following system of inhomogeneous first-order differential equations describing the adsorbate surface densities n_A and n_B :

$$\frac{\partial n_A}{\partial t} = s_A J_A \left(1 - \frac{n_A}{n_{ML,A}} - \frac{n_B}{n_{ML,B}} \right) - \frac{n_A}{\tau_A} - \sigma_A f n_A \quad (4.2a)$$

$$\frac{\partial n_B}{\partial t} = s_B J_B \left(1 - \frac{n_B}{n_{ML,B}} - \frac{n_A}{n_{ML,A}} \right) - \frac{n_B}{\tau_B} - \sigma_B f n_B \quad (4.2b)$$

where the first term accounts for surface adsorption sites already occupied by the other species [135]. Here, J is the flux of impinging precursor molecules, n_{ML} is the maximum monolayer density, s is the sticking probability and τ is the residence time. Solving this differential equations system imposing full replenishment ¹ yields:

$$n_A(t) = n_{dA} + \exp(-\bar{k}_d t) [\Delta n_A \cosh(\kappa t) + N_A \sinh(\kappa t)] \quad (4.3a)$$

$$n_B(t) = n_{dB} + \exp(-\bar{k}_d t) [\Delta n_B \cosh(\kappa t) + N_B \sinh(\kappa t)] \quad (4.3b)$$

where

$$\begin{aligned} N_A &= [(\bar{k}_d - k_{dA})\Delta n_A - k_{cA}\Delta n_B]/\kappa \\ N_B &= [(\bar{k}_d - k_{dB})\Delta n_B - k_{cB}\Delta n_A]/\kappa \\ \Delta n_A &= n_{rA} - n_{dA} \\ \Delta n_B &= n_{rB} - n_{dB} \\ \bar{k}_d &= (k_{dA} + k_{dB})/2 \\ \kappa &= \sqrt{(k_{dA} - k_{dB})^2/4 + k_{cA}k_{cB}} \end{aligned} \quad (4.4)$$

n_{rA} and n_{rB} represent the steady state surface density at full replenishment (i.e. at $t_d=0$) and n_{dA} and n_{dB} represent the equilibrium surface density at

¹The condition for full replenishment is fulfilled for $k_r \cdot t_r \gg 1$, i.e. when the refresh time t_r is much higher than the inverse of the rate constant for the replenishment process k_r as defined in equation (2.5).

full adsorbate depletion (i.e. for $t_d \rightarrow \infty$). They are given by:

$$\begin{aligned}
 n_{rA} &= \frac{s_A J_A k_{rB} - s_B J_B k_{cA}}{k_{rA} k_{rB} - k_{cA} k_{cB}} \\
 n_{rB} &= \frac{s_B J_B k_{rA} - s_A J_A k_{cB}}{k_{rA} k_{rB} - k_{cA} k_{cB}} \\
 n_{dA} &= \frac{s_A J_A k_{dB} - s_B J_B k_{cA}}{k_{dA} k_{dB} - k_{cA} k_{cB}} \\
 n_{dB} &= \frac{s_B J_B k_{dA} - s_A J_A k_{cB}}{k_{dA} k_{dB} - k_{cA} k_{cB}}
 \end{aligned} \tag{4.5}$$

The model constants k_{dA} and k_{dB} , representing the rate constants of the depletion processes, and k_{rA} and k_{rB} , representing the rate constants of the replenishment processes were introduced in the frame of the single-adsorbate model in section 2.1.3 in equation (2.5) and remain unchanged. The constants k_{cA} and k_{cB} are a measure of the competitive adsorption between the two molecular species and are expressed by:

$$k_{cA} = \frac{s_A J_A}{n_{ML,B}} \qquad k_{cB} = \frac{s_B J_B}{n_{ML,A}} \tag{4.6}$$

It is readily seen that setting them to zero leads to the *single*-molecule model given by equation (2.5).

The dissociation yield Y , describing the dissociative events per primary electron, has been introduced in equation (2.6) for the single-molecule case. In analogy, we introduce two dissociation yields Y_A and Y_B describing the dissociative events per primary electron for each of both adsorbates involved in the deposition:

$$Y_A = \sigma_A \int_0^{t_d} n_A(t) dt / t_d \tag{4.7a}$$

$$Y_B = \sigma_B \int_0^{t_d} n_B(t) dt / t_d \tag{4.7b}$$

The dependence of the dissociation yields on the dwell time is shown exemplarily for the $\text{Co}_2(\text{CO})_8$ model in figure 4.7.

The total deposition rate in the presence of two adsorbates is expressed as the sum of the deposition rates for each species, as described in equation (2.2), i.e. the dissociation yields (given by equations (4.7)) multiplied by the incoming electron flux f and the volume of the decomposed molecule V_A and

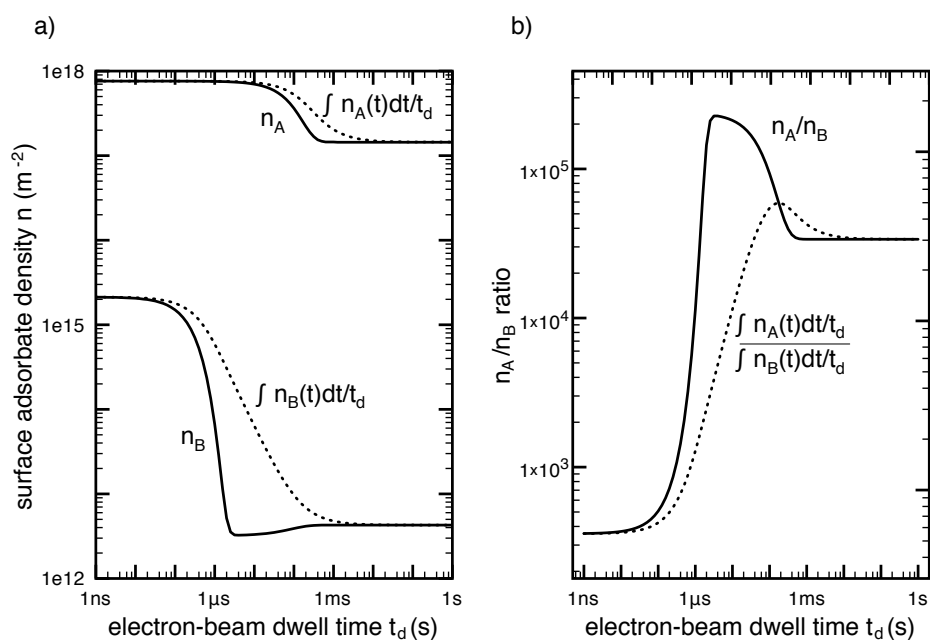


Figure 4.6: a) Surface adsorbate densities and pulse-averaged surface adsorbate densities and b) corresponding ratios. The example system is $\text{Co}_2(\text{CO})_8$ (A) and background hydrocarbons (B). The effect of competitive adsorption is visible: As the dwell time t_d increases, depletion of the adsorbate B occurs. At $t_d \approx 80 \mu\text{s}$, partial depletion of adsorbate A begins. This liberates surface sites, which are filled by the adsorbate B. For this reason, a “bump” in the function $n_B(t_d)$ (and a corresponding peak of the function n_A/n_B) occurs at around $t_d \approx 80 \mu\text{s}$.

V_B respectively:

$$R = \frac{f}{t_d} \int_0^{t_d} [V_A \sigma_A n_A(t) + V_B \sigma_B n_B(t)] dt \quad (4.8)$$

In figure 4.6a, the surface adsorbate densities n_A and n_B are plotted versus the electron pulse time t_d . As the irradiation proceeds, one of the adsorbates, say B , starts to be depleted and the surface adsorbate density moves toward a lower equilibrium value. As the depletion of the other species, here A , occurs, surface sites are liberated, which slightly increases the number of surface adsorbates for the first species. The individual onset of the transition from electron- to adsorbate-limited is given approximately by the inequality $t_d > (sJ/n_{ML} + 1/\tau + \sigma f)^{-1}$ for the specific molecule ². The ratio between the surface adsorbate densities is shown in figure 4.6b. In the example shown ($\text{Co}_2(\text{CO})_8$ and background hydrocarbons), the ratio of adsorbates present at the surface can be changed by *over two orders of magnitude* by simply changing the electron flux duration. This ratio peaks for the situation where one of the adsorbate is in depletion and the other is still being deposited in the electron-limited regime.

4.4.2 Composition of the deposit in the two-adsorbate model

We have introduced the generic electron-impact reactions of two adsorbate species A and B in equations (4.1). Using this notation, the deposit composition is determined by the ratio of deposited reaction products of each decomposition reaction:

$$Z = \frac{[D_A]}{[D_B]} = \frac{Y_A}{Y_B} \quad (4.9)$$

where $[D_A]$ and $[D_B]$ are the concentrations of the non-volatile dissociation products D_A and D_B . The yield ratio Z is determining the range within which variation in composition can be realized by tuning the depletion state of the adsorbates; more precisely, the extent to which the process is tunable is given by the comparison of the yield ratio $Z_0 = \lim_{t_d \rightarrow 0} Z(t)$ close to very short pulse times and the yield ratio $Z_\infty = \lim_{t_d \rightarrow \infty} Z(t)$ for pulse times tending to infinity. The higher this ratio Z_0/Z_∞ , the broader the composition window tunable by selective depletion.

²The exact onset depends on the variables given by equation (4.4)

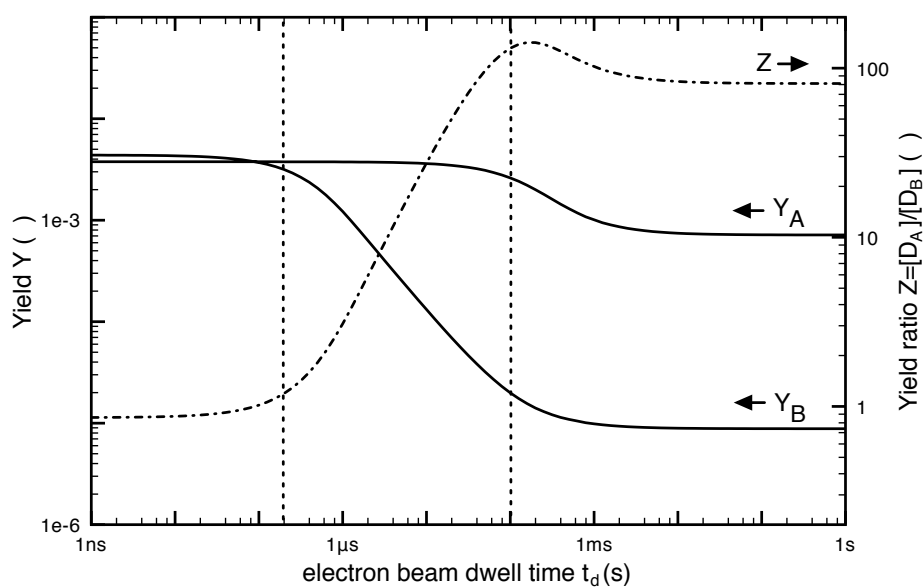


Figure 4.7: Calculated dissociation yields per primary electron Y_A and Y_B (as introduced in equation (2.6)) and yield ratio Z (given by equation (4.9)) versus electron beam dwell time. The example system is $\text{Co}_2(\text{CO})_8$ (A) and background hydrocarbons (B). The yield ratio is a measure for the ratio of non-volatile fragments of molecule A and B in the FEB deposit .

The yield ratios for very short dwell times can be derived from equation (4.7) as:

$$Z_0 = \frac{\sigma_A s_A J_a \tau_A}{\sigma_B s_B J_B \tau_B} \quad (4.10)$$

For very small exposure times, both reactions (4.1) are electron-limited and the composition is proportional to the ratios of the electron impact dissociation cross-sections σ_A and σ_B , the residence times τ_A and τ_B , the sticking probabilities s_A and s_B and the molecule fluxes J_A and J_B of both adsorbates. The composition is independent on the electron flux f for very small exposure times. Experimentally, a higher metallic concentration in the deposit for a given system of two adsorbates can be obtained by either increasing the partial pressure of the metal-containing precursor or by reducing the partial pressure of the other species, i.e. increasing the molecular flux J_A or decreasing J_B .

For very long dwell times, the following yield ratio is found:

$$Z_\infty = \frac{\sigma_A s_A J_A (1/\tau_B + \sigma_B f)}{\sigma_B s_B J_B (1/\tau_A + \sigma_A f)} \quad (4.11)$$

From this relation follows that in order to change the composition to a value different than already obtained at very small exposure times, at least one of the electron-impact reactions must be driven into the molecule-limited regime. This requires to adjust the electron flux such that $\sigma_A f \gg \tau_A^{-1}$ or/and $\sigma_B f \gg \tau_B^{-1}$, in other words, for at least one adsorbate, decomposition by the electrons should proceed at a faster rate than spontaneous thermal desorption. If the conditions for the molecule-limited regime are fulfilled for both adsorbates, equation (4.11) simplifies to $Z_\infty \approx (s_a J_a)/(s_B J_B)$ and the final decomposition product for high electron beam pulse times is given by the ratio of the molecular fluxes and the corresponding sticking probabilities.

The ratio between the calculated yield ratios is a measure of the tunability of the deposition process regarding the deposit composition and is expressed as:

$$\frac{Z_0}{Z_\infty} = \frac{1/f + \sigma_A \tau_A}{1/f + \sigma_B \tau_B} \quad (4.12)$$

For sufficiently high electron fluxes f , the ultimate tunability is determined by the ratio $\sigma_A \tau_A / \sigma_B \tau_B$. Replacing an adsorbate species with a species exhibiting a higher dissociation cross section σ will lead, as is readily seen from equation (4.10), to a modified composition for short pulse durations, exhibiting a larger contribution from this deposited species. For long pulses,

a higher cross-section will also lead to a higher contribution of this species to deposition.

Upon heating of the substrate, the residence time will vary, according to $\tau(T) = \tau_0 \exp(E_{des}/kT)$, where E_{des} represents the activation energy for desorption [15]. As a consequence, a temperature increase will change the residence time ratio in equation (4.10) towards a situation where comparatively longer residence time is obtained for the species with the lower activation energy for desorption. This would enhance the relative contribution of this species to the deposition at short pulse times. However, the shortening of the residence times induced by the heating will eventually lead to a situation where the major pathway of adsorbate removal is through thermal desorption, i.e. $1/\tau \gg \sigma f$, and the tunability of the process vanishes.

4.4.3 Application of the model to the experimental system

We now proceed to applying the two-adsorbate model developed to the deposition system consisting of $\text{Co}_2(\text{CO})_8$ and a model hydrocarbon. In the high vacuum (HV) chamber, a significant amount of residual species participate in the deposition process, as can be seen in figure 4.2b. The most abundant species in the chamber background are water vapor and hydrocarbons. From figure 4.2b we estimate that about half of the molecules present in the chamber background are water, with the balance consisting mainly of hydrocarbons. It is known that carbon-deposition by hydrocarbon decomposition and carbon-etching by water vapor are concurrent processes under electron irradiation [135, 136]. Physisorbed water on carbon surfaces dissociates under electron-impact to highly reactive species, which react to volatile carbon compounds, thus etching (nanosized) holes in the carbon substrate when a stationary focused electron beam is used [137]. The average residence time for the physisorbed water is below $1\mu\text{s}$ on stainless steel [133, 138]; in [136], a mean surface residence time of 160ns was estimated for H_2O on a $\text{In}_{0.6}\text{Ga}_{0.4}\text{As}$ surface. Part of the adsorbed water however stays on the surface for much longer [138]. For the water vapor having a net etching effect over hydrocarbon decomposition and deposition, it was found that the water vapor must be present at very high pressures ($>1\text{mbar}$, corresponding roughly to $3.5 \times 10^5 \text{ML/s}$) [136]. This is the reason why we disregard the water vapor with regard to its influence, at 10^{-6} - 10^{-5}mbar , typical for our experiments, on the metal-to-carbon composition. Still, two effects of the water vapor are possible. First, it could in some cases oxidize the deposited metal [36]. Second, it could have an effect on the number of free adsorption sites, thus

reducing the adsorption of $\text{Co}_2(\text{CO})_8$ or the hydrocarbon species. However, due to the small molecular area, the cross-interaction k_c of the water vapor (see equation (4.6)) is small as compared to the cross-interaction between $\text{Co}_2(\text{CO})_8$ and a model hydrocarbon (see table 4.1).

The chamber background hydrocarbons are generally believed to consist of several species of hydrocarbon molecules. From the RGA data shown in figure 4.2b, we indeed infer the presence of several hydrocarbon species with atomic masses above 45 atomic mass units. For the sake of the application of the two-adsorbate model to this specific experimental case, a model hydrocarbon had to be chosen. We chose different plausible hydrocarbon model molecules which are shown in table 4.1. Octanol ($\text{C}_8\text{H}_{17}\text{OH}$) is present in our atmospheres as a result of combustion engines. A five-ring polyphenyl ether (PPE, $\text{C}_{30}\text{H}_{22}\text{O}_4$) and its decomposition products, the three-ring PPE $\text{C}_{18}\text{H}_{14}\text{O}_2$, diphenyl ether $\text{C}_{12}\text{H}_{10}\text{O}$, phenol $\text{C}_6\text{H}_6\text{O}$ and benzene C_6H_6 are plausibly present in the chamber as the five-ring PPE was used as vacuum oil in the oil diffusion pumping system. Isopropanol $\text{C}_3\text{H}_8\text{O}$ or acetone $(\text{CH}_3)_2\text{CO}$ might be present as residues from the sample cleaning procedure. It was found that the quantitative application of the two-adsorbate model was not relying crucially on the choice of the model hydrocarbon, mainly because the used dissociation parameters for the model hydrocarbon were retrieved by fitting the deposition values under single-adsorbate conditions in our experimental environment. The single most-important parameter determining the quality of the fit of the two-adsorbate model with the composition of the deposit was found to be the number of Carbon atoms per dissociated molecule volume V .

4.4.4 Estimation of molecule parameters using the single-adsorbate model

In order to apply the two-adsorbate model to the system $\text{Co}_2(\text{CO})_8$ and a model hydrocarbon, one needs to estimate the input parameters, namely the molecular flux J , the sticking probability s , the electron flux f , the monolayer densities n_{ML} , the dissociation cross-section σ , the mean surface residence time τ . In the following, we discuss how estimates were found for the model parameters in the $\text{Co}_2(\text{CO})_8$ and model hydrocarbon system. All model parameters are shown in table 4.1.

Molecular and electron flux, and monolayer densities

The impinging molecular flux J_A of $\text{Co}_2(\text{CO})_8$ during the experiments was about 4.4×10^{15} molecules/s, as estimated from mass loss measurements.

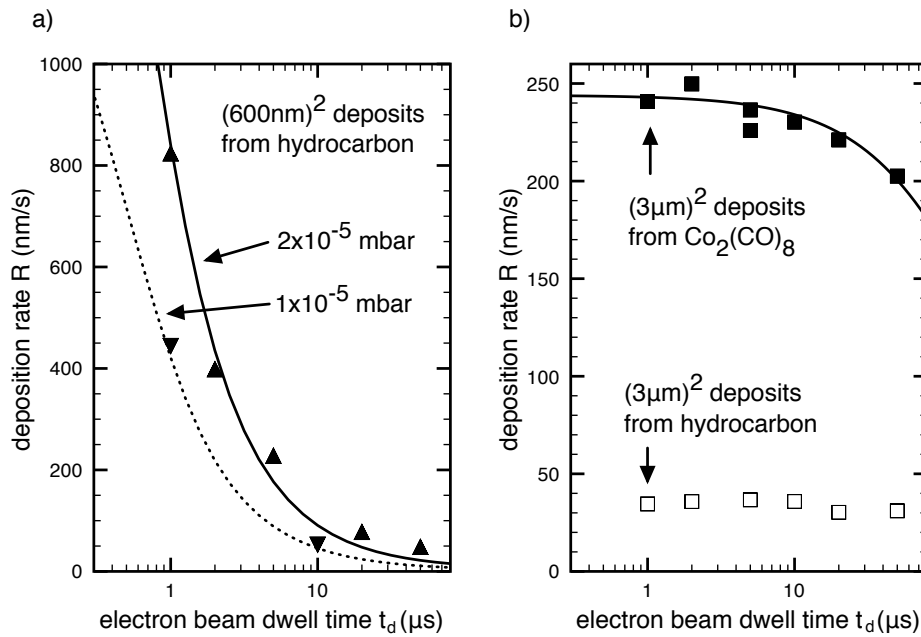


Figure 4.8: *Experimental values and single-adsorbate model fits of the vertical deposition rate R according to equation (2.8). a) Deposition rates of $(600\text{nm})^2$ hydrocarbon deposits at 1 and 2×10^{-5} mbar. b) Deposition rates of $(3\mu\text{m})^2$ deposits from $\text{Co}_2(\text{CO})_8$ and hydrocarbon at 1×10^{-5} mbar. The total electron dose for all deposits was maintained constant at $10\text{C}/\text{cm}^2$. Experimental values are measured in the center of the deposits to avoid edge effects.*

species	chemical formula	$sJ^{[1]}$ $\text{cm}^{-2}\text{s}^{-1}$	$n_{ML}^{[2]}$ nm^{-2}	V nm^3	σ nm^2	τ μs	k_r s^{-1}	k_d s^{-1}	$k_c^{[5]}$ s^{-1}
Dicobalt octacarbonyl	$\text{Co}_2(\text{CO})_8$	$1.5 \cdot 10^{17}$	2.6	$3.8 \cdot 10^{-2[3]}$	$5 \cdot 10^{-3}$	720	$2 \cdot 10^3$	$1 \cdot 10^4$	$4.3 \cdot 10^{2(a)}$ $1.6 \cdot 10^{2(c)}$
Octanol	$\text{C}_8\text{H}_{17}\text{OH}$	$1.59 \cdot 10^{15}$	3.4	$1.44 \cdot 10^{-1[3]}$	2.1	190	$5 \cdot 10^3$	$4 \cdot 10^6$	6.1 ^(b) 1.7 ^(c)
Five-ring PPE	$\text{C}_{30}\text{H}_{22}\text{O}_4$	$8.60 \cdot 10^{14}$	1.1	$6.17 \cdot 10^{-1[4]}$	2.4	80	$1 \cdot 10^4$	$4 \cdot 10^6$	3 ^(b)
Three-ring PPE	$\text{C}_{18}\text{H}_{14}\text{O}_2$	$1.12 \cdot 10^{15}$	3.5	$3.96 \cdot 10^{-1[4]}$	2.3	90	$1 \cdot 10^4$	$4 \cdot 10^6$	4 ^(b)
Diphenyl ether	$\text{C}_{12}\text{H}_{10}\text{O}$	$1.39 \cdot 10^{15}$	8.6	$2.64 \cdot 10^{-1[4]}$	2.2	110	$9 \cdot 10^3$	$4 \cdot 10^6$	5 ^(b)
Phenol	$\text{C}_6\text{H}_6\text{O}$	$1.87 \cdot 10^{15}$	4.2	$1.46 \cdot 10^{-1[4]}$	2.1	150	$7 \cdot 10^3$	$4 \cdot 10^6$	7 ^(b)
Benzene	C_6H_6	$2.05 \cdot 10^{15}$	8.8	$1.48 \cdot 10^{-1[4]}$	2.1	140	$7 \cdot 10^3$	$4 \cdot 10^6$	8 ^(b)
Acetone	$(\text{CH}_3)_2\text{CO}$	$2.38 \cdot 10^{15}$	7.2	$1.22 \cdot 10^{-1[4]}$	2.1	150	$7 \cdot 10^3$	$4 \cdot 10^6$	9 ^(b)
Isopropanol	$\text{C}_3\text{H}_8\text{O}$	$2.34 \cdot 10^{15}$	5.5	$1.26 \cdot 10^{-1[4]}$	2.1	140	$7 \cdot 10^3$	$4 \cdot 10^6$	9 ^(b)
Water	H_2O	$3.6 \cdot 10^{15}$	9.4						1.4 ^(b) 1.0 ^(a)

Table 4.1: Model parameters for $\text{Co}_2(\text{CO})_8$ and selected model hydrocarbons. ^[1] Calculated from mass loss measurement and MC simulation of precursor distribution ($\text{Co}_2(\text{CO})_8$) or approximated from chamber background pressure (model hydrocarbons and water). ^[2] Estimated from the area of the undissociated precursor molecule. ^[3] Estimated from the molar mass and the deposit density as described in [39]. ^[4] Estimated from the molar mass and the density of the undissociated molecule. ^[5] Calculated using equation (4.6) with respect to ^(a) Octanol ^(b) $\text{Co}_2(\text{CO})_8$ or ^(c) water.

According to gas flow MC simulations [129], this translates into 1.5×10^{17} $\text{cm}^{-2}\text{s}^{-1}$ (or approximately 600 monolayers (ML)/s) impinging on the FEB irradiated spot. The impinging flux J_B of the hydrocarbon was estimated from the residual chamber pressure, using the relation [133]:

$$J_B = \frac{pN_A}{\sqrt{2\pi M_B R T}} \quad (4.13)$$

where p is the chamber pressure, M_B is the molar mass of the model hydrocarbon, T is the temperature, N_A is Avogadro's number and R is the gas constant. The corresponding values are given in table 4.1. As the impinging flux of hydrocarbon is dependent on the residual chamber pressure, the dosing of the hydrocarbon flux could be experimentally implemented by variation of the pumping time prior to the deposition experiments. For this purpose, the pressure versus pumping time of the experimental chamber was calibrated (see figure 4.2a).

The electron flux was calculated from the electron beam current as measured in a Faraday cup (1nA) and the beam FWHM of 70nm, corresponding to a PE flux of 1.7×10^{20} $\text{cm}^{-2}\text{s}^{-1}$ (assuming a flat-top beam).

The sticking probabilities s_A and s_B are unknown parameters and we assumed $s_A J_A = J_A$ and $s_B J_B = J_B$, i.e. the sticking probabilities were assumed unity. Turning back to equations (2.5b) using the values given for the $\text{Co}_2(\text{CO})_8$ and model hydrocarbon system, it is apparent that the rate constants k_{dA} , k_{dB} , k_{rA} and k_{rB} are not limited by the incoming flux of molecules, but rather by thermal desorption (in the case of the replenishment process) or by electron-beam induced dissociation (for the depletion process). Hence, assuming $s_A = s_B = 1$ induces at worse a proportional error factor on the surface adsorbate densities n_d and n_r given by equation (2.5c) but does not affect the discussion of the effect of compositional variations by the variation of the electron beam pulse duration.

The monolayer densities $n_{ML,A}$ and $n_{ML,B}$ were estimated using the molecule's area. For the estimation of the decomposed volume of the adsorbates, one uses the following relation:

$$V = \frac{M}{N_A \rho} \quad (4.14)$$

where M is the molar mass and ρ is the density of the deposited material. In the case of $\text{Co}_2(\text{CO})_8$, the density of the decomposed material $\text{Co}_2\text{C}_{0.6}\text{O}_{0.4}$ was estimated by taking a weighted average between the density of Co and the density of the amorphous carbon matrix, the weight coefficient being given by the atomic composition of the deposit [39]. The decomposed volume of $\text{Co}_2\text{C}_{0.6}\text{O}_{0.4}$ was estimated to 3.8×10^{-2} nm^3 . This value compares

with $6.3 \times 10^{-2} \text{ nm}^3$ used for the FEBID product of $\text{W}(\text{CO})_6$ in [30]. For the hydrocarbon, one can use the density of the *undissociated* molecule. However, this approach is prone to overestimation. A better estimate might be given by the value of the amorphous matrix given in [39] ($\rho = 1.5 \text{ g/cm}^3$). This value compares to the density obtained for the result of electron-beam dissociation of organic precursors for the deposition of Carbon [139]. This “generic hydrocarbon” has a composition of $\text{C}_9\text{H}_2\text{O}$, comparable to the result of hydrocarbon deposition under our experimental conditions, and has a reported density of 1.7 g/cm^3 as estimated from a Rutherford backscattering spectrometry experiment [140].

Average surface residence time and electron-impact dissociation cross-section

One is left with the residence times τ_A and τ_B and the electron-impact dissociation cross-sections σ_A and σ_B which are a priori unknown molecular parameters. They were retrieved by fitting the deposition rates of the square deposits obtained under single-adsorbate conditions (see section 4.3) using the deposition rate equation (2.8).

For hydrocarbons, single adsorbate conditions were realized by injecting no precursor gas molecules; the remaining background water molecules and their related carbon etch rate can be neglected at this pressure [135, 136]. The fit of the $(600 \text{ nm})^2$ square deposits shown in figure 4.8a was performed according to equation (2.8) at two background pressures. They were used to extract the corresponding σ_B and τ_B values. The corresponding values are given in table 4.1. The hydrocarbon deposition rate at the centre was seen to be very size-dependent when comparing these deposition rates with $(3 \mu\text{m})^2$ structures in figure 4.8b. This is due to adsorbate surface diffusion: the smaller the (deposit) size the larger becomes the contribution of surface diffusion for adsorbate supply and thus the deposition rate.

This effect was used to achieve quasi single-adsorbate conditions for $\text{Co}_2(\text{CO})_8$, which were realized by depositing $(3 \mu\text{m})^2$ squares keeping the hydrocarbon supply by surface diffusion confined to the deposit rim. AFM measurements showed the rim to be about $1 \mu\text{m}$ wide and EDX confirmed a larger variable carbon content in this region (see figure 4.10). From figure 4.8b, it follows that the deposition rate for $\text{Co}_2(\text{CO})_8$ and 10^{-5} mbar hydrocarbon backpressure plateaus at 245 nm/s in the electron limited regime. For the same conditions the hydrocarbon deposition rate stays roughly constant at 35 nm/s , being less than 15%, thus allowing the extraction of σ and τ data for $\text{Co}_2(\text{CO})_8$ under conditions close to single adsorbate deposition. The corresponding values are given in table 4.1. A fitted $\sigma(\text{Co}_2(\text{CO})_8)$ of

$5 \times 10^{-3} \text{nm}^2$ is found, which corresponds to the value obtained from fitting the shape of dot deposits in [141].

For all single-adsorbate deposits, a refresh time t_r of 10ms, during which the electron-beam was blanked, was used in order to allow full replenishment of the surface with the adsorbate to the equilibrium state n_r . In the case of $\text{Co}_2(\text{CO})_8$, the fitted values for σ and τ are uniquely determined, as the experimental values describe the electron-limited *and* the onset of the precursor-limited regime, imposing two independent constraints on equation (2.8). The uniqueness of the fit is represented graphically in figure 4.9a. In the case of hydrocarbon deposition, only τ is uniquely determined, and σ represents a lower boundary estimation. Variations of the model deposition rates with varying σ and τ values are shown in figure 4.9b.

Surface diffusion

We now turn to the question of surface diffusion. It is known that surface diffusion can represent a substantial pathway of molecular supply to the FEBID process [15]. However, in equation (2.3) and (4.2), the surface diffusion is not explicitly taken into account. This allows us to derive an analytical solution in equation (4.3) and to derive general observations about the tunability of the codeposition process.

We estimate the importance of surface diffusion using the height profile of $3\mu\text{m}$ square deposits. In figure 4.10, the height profiles of $(3\mu\text{m})^2$ deposits are plotted in the case of $\text{Co}_2(\text{CO})_8$ and hydrocarbon deposition. Both profiles were measured on deposits with a dose of $10\text{C}/\text{cm}^2$ and a dwell time of $t_d=10\mu\text{s}$. Clearly, the deposition of the hydrocarbons is diffusion enhanced and one obtains the profile typical for this deposition regime [44, 64]. The profile is inclined towards the center of the deposit, as the effect of surface diffusion decreases as the precursor refresh pathway. From the profile, it appears that the diffusion length of the hydrocarbons is greater than $1.5\mu\text{m}$ under our experimental conditions. However, the edges of the $3\mu\text{m}$ $\text{Co}_2(\text{CO})_8$ exhibit a rim of about $1\mu\text{m}$ due to surface diffusion of hydrocarbons at the edges of the deposit. The diffusion length of the hydrocarbons appears to be shorter on the CoC deposit.

Surface diffusion is a thermally activated process, where a rupture of the bond between the adsorbate and the surface occurs and an analogous bond with an adjacent adsorption site is formed [15]. It is important to note that the case of a scanned beam differs from the steady-state case in that the depletion of surface adsorbed species is a function of location *and* time. Hence, surface diffusion depends not only on the level of depletion of the irradiated pixel, but also on the level of depletion of neighboring locations,

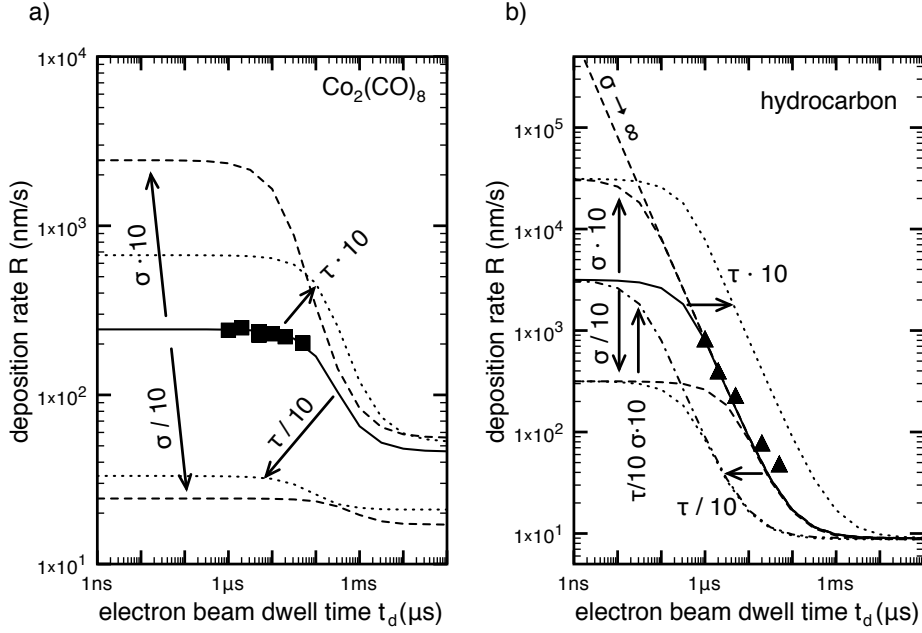


Figure 4.9: a) Variations of the fit parameters σ and τ and influence on the $\text{Co}_2(\text{CO})_8$ deposition rates. Full squares are the experimental data points from figure 4.8b. The base line (full line) corresponds to the model using $\sigma = 5 \times 10^{-3} \text{ nm}^2$ and $\tau = 720 \mu\text{s}$. In the electron-limited regime, the deposition rate is proportional to the electron dissociation cross-section σ (see equation (2.8)). Furthermore, we have $\sigma f \approx \tau^{-1} \gg sJ/n_{ML}$ so that the onset of the depletion given by $t_d > k_d^{-1}$ is determined by both σ and τ . b) Variations of the fit parameters σ and τ and influence on the hydrocarbon deposition rates. Full triangles are the experimental data points from figure 4.8a. The base line (full line) corresponds to the model using $\sigma = 2.3 \text{ nm}^2$ and $\tau = 90 \mu\text{s}$. The fitted σ represents a lower boundary estimation, as only depleted deposition was measured experimentally. Here, we have $\sigma f \gg \tau^{-1} \gg sJ/n_{ML}$ so that the depletion process is mostly governed by the dissociation cross section σ . Here, variations of τ express themselves by variations of the adsorbate density at replenishment n_r .

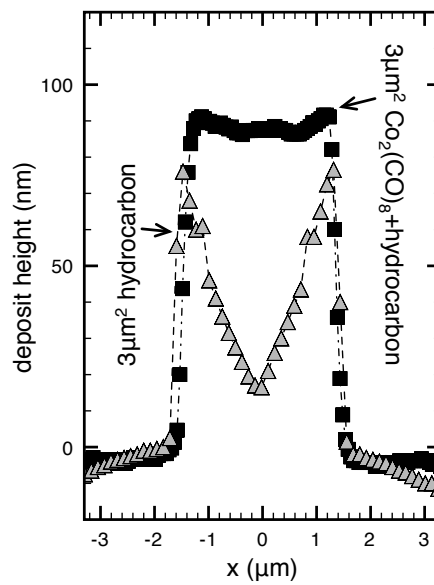


Figure 4.10: AFM profile of a $(3\mu\text{m})^2$ deposit of $\text{Co}_2(\text{CO})_8$ (black squares) and hydrocarbon (grey triangles). The dwell time was $t_d=10\mu\text{s}$ in both cases. Both depositions were carried out at a background chamber pressure of $\approx 1 \times 10^{-5}$ mbar.

so that it is not straightforward to precisely model surface diffusive effects on the scale of the deposit.

In our case, the values of σ and τ were fitted on 600nm square deposits in the case of hydrocarbons, so that the application to square deposits of 600nm under co-deposition conditions remains systematically correct. The values of σ and τ were fitted on $3\mu\text{m}$ square deposits in the case of $\text{Co}_2(\text{CO})_8$, but it is apparent that surface diffusion plays a much lower role in the transport of fresh precursor under the experimental molecular flux and at the size scales we have, as can be inferred by the flat height profile in figure 4.10.

It has been suggested that surface diffusion leads to an increase in the residence time τ , so that τ would constitute an effective residence time including spontaneous thermal desorption *and* surface diffusion [15]. While this might hold true in the single-spot irradiation situation, we find that this pathway is not sufficient to quantitatively model the deposition rates for the $3\mu\text{m}$ square and 600nm square deposits of hydrocarbon. In other words, it is not possible to fit a single σ value which would allow to describe both deposition rates (of the 600nm and $3\mu\text{m}$ hydrocarbon squares) using an increased τ value for the smaller deposit. In the case of a planar deposit, surface diffusion also depends on the depletion level of adjacent pixels, which is linked to the deposition strategy shown in figure 4.1b. By scanning the electron beam in a (line-by-line or peripheral) serpentine path, the *line refresh time*, defined as the time elapsing between the irradiation of two adjacent lines of the serpentine pattern, is becoming size dependent, all other experimental conditions being equal. When there is a beam overlap and the line refresh time is shorter than the full replenishment time, the assumption that full replenishment of the adsorbates is achieved between the irradiation pulses does not hold any more and the *exact* surface densities (as opposed to the model approach) become *intrinsically* dependent on the size of the planar deposit.

It is hence important to note that in the system $\text{Co}_2(\text{CO})_8$ and hydrocarbon, smaller deposits (within the diffusion length of the hydrocarbons) are thus richer in Carbon, as the contribution from the hydrocarbon is increased by surface diffusion. In fact, what we call quasi-single adsorbate conditions is a geometry where the contribution of hydrocarbon supply by surface diffusion is negligible. However, it must be emphasized that the model is still universally applicable, if one knows the electron-impact dissociation cross-section σ and the surface residence time τ , as long as the conditions under which they have been measured are known.

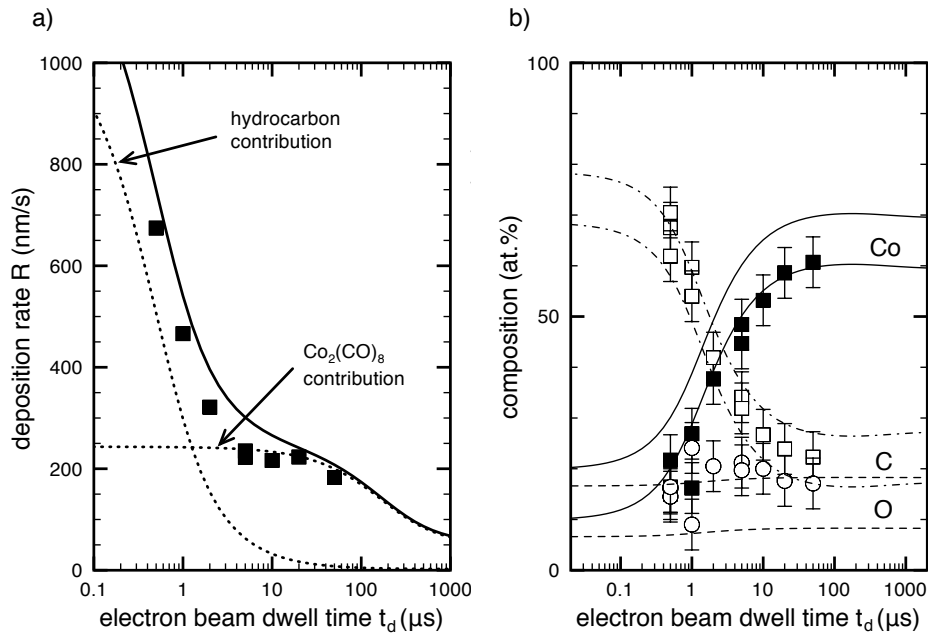


Figure 4.11: Application of the two adsorbate model to the system $\text{Co}_2(\text{CO})_8$ and hydrocarbon. The two-adsorbate system consists of $\text{Co}_2(\text{CO})_8$ at a flux of $1.5 \times 10^{17} \text{ cm}^{-2} \text{ s}^{-1}$ and hydrocarbon at a flux corresponding to 1×10^{-5} mbar residual pressure. Octanol is taken as the model molecule for hydrocarbons. The total electron dose for all deposits was maintained constant at $10\text{C}/\text{cm}^2$. a) Deposition rates of $(600\text{nm})^2$ deposits. The full line shows the corresponding model prediction (equation (4.8)). The dashed lines show the respective contributions from each species to the overall deposition rate. b) Measured composition of $(600\text{nm})^2$ deposits from $\text{Co}_2(\text{CO})_8$:hydrocarbons under two-adsorbates conditions with the model prediction shown as an overlay.

4.4.5 Application of the model to the experimental system

Deposition rates

The deposition rates calculated from the two-adsorbate model are compared with experimental rates in figure 4.11a. The corresponding yields Y_A and Y_B are shown in figure 4.7. For short pulse times, the deposition process is predominantly driven by the dissociation of hydrocarbons; for longer pulse times, the contribution of the hydrocarbons to the deposition process decreases, as the deposition is driven into a molecule-limited regime for the hydrocarbon.

Composition

The “translation” of the model Z values (equations (4.10) and (4.11)) into the deposit composition requires knowledge about the composition of the adsorbate dissociation products D_A and D_B . Depending on the nature of the parent adsorbates, the dissociation products are either pure elements or compounds made up of additional elements from the parent adsorbate molecule. Under our quasi single-adsorbate conditions, the dissociation product of cobalt carbonyl adsorbates was approximately $\text{Co}_2\text{C}_{0.6}\text{O}_{0.4}$ for all exposure times, as is shown in figure 4.3a. Of note is that this includes co-deposition of the hydrocarbon species at a relative rate of $\approx 15\%$ with respect to the $\text{Co}_2(\text{CO})_8$ deposition rate as discussed in section 4.4.4. Taking the co-deposition of the hydrocarbon under the quasi-single-adsorbate conditions into account, a composition of $\text{Co}_{77}\text{C}_9\text{O}_{14}$ is found, giving a more precise measure of the dissociation product of Cobalt carbonyl under single-adsorbate conditions in our experimental setup. The EDX measurement have been calibrated to 2 Co atoms, i.e. we assume that no Co-containing, volatile fragment is produced during the electron-impact dissociation of the parent compound. It is important to note that the composition of this deposit material obtained from electron impact dissociation of the quasi single-adsorbate species $\text{Co}_2(\text{CO})_8$ is constant for the investigated pulse times (see figure 4.3a). Hence, the observed compositional variations in the two-adsorbate conditions can *not* be explained by a more complete dissociation of the parent compound with increasing electron beam pulse time.

The electron-impact dissociation product of the hydrocarbon species under single-adsorbate conditions showed a carbon-to-oxygen ratio of about 8.5:1, which is close to the ratio found in deposits from other organic precursors ($\text{C}_9\text{H}_2\text{O}$) [139]. Hence, the model hydrocarbon molecule with initial composition $\text{C}_x\text{H}_y\text{O}_z$ is dissociated into a non-volatile deposit with composition $\text{C}_{x_C}\text{H}_{y_C}\text{O}_{z_C}$, where $x_C/z_C=8.5$. Assuming $x \approx x_C$, i.e. that the majority of the C atoms of the model hydrocarbon molecule are being incorporated into the deposit as a result of electron-impact dissociation, one obtains an estimate of the number of atoms incorporated into the deposit. In the case of the example molecule octanol, the relation is $\text{C}_8\text{H}_{17}\text{OH} \rightarrow \text{C}_8\text{O}_{0.95}$.

We are now ready to apply the dissociation products in order to calculate the atomic composition of the overall deposit. For this step, we call $Y_{\text{Co}_2(\text{CO})_8}$ and $Y_{\text{C}_x\text{H}_y\text{O}_z}$ the dissociation yields for Cobalt carbonyl and the hydrocarbon. The product of the Cobalt carbonyl dissociation is referred to as $\text{Co}_{x_{\text{Co}}}\text{C}_{y_{\text{Co}}}\text{O}_{z_{\text{Co}}}$ and the product of the hydrocarbon dissociation is referred to as $\text{C}_{x_C}\text{H}_{y_C}\text{O}_{z_C}$. It is then possible to express the outcome of the FEB induced deposition in this two adsorbate system using the following, general

relations:

$$[Co] = \frac{Y_{Co_2(CO)_8} \cdot x_{Co}}{Y_{Co_2(CO)_8}(x_{Co} + y_{Co} + z_{Co}) + Y_{C_xH_yO_z}(x_C + z_C)} \quad (4.15)$$

where the numerator represents the number of deposited Co atoms per electron, and the denominator represents the total number of deposited atoms per electron. Similar expressions can be found for the Oxygen and Carbon contents:

$$[C] = \frac{Y_{Co_2(CO)_8} \cdot y_{Co} + Y_{C_xH_yO_z} \cdot x_C}{Y_{Co_2(CO)_8}(x_{Co} + y_{Co} + z_{Co}) + Y_{C_xH_yO_z}(x_C + z_C)} \quad (4.16)$$

$$[O] = \frac{Y_{Co_2(CO)_8} \cdot z_{Co} + Y_{C_xH_yO_z} \cdot z_C}{Y_{Co_2(CO)_8}(x_{Co} + y_{Co} + z_{Co}) + Y_{C_xH_yO_z}(x_C + z_C)} \quad (4.17)$$

where Y_{Co} is the dissociation yield of $Co_2(CO)_8$ and Y_C is the dissociation yield of octanol. The model values are plotted together with the measured composition under two-adsorbates conditions in figure 4.11b. The two-adsorbate model derived in this chapter is found to be in excellent agreement with the experimentally observed variations in deposit composition.

4.5 Conclusions

In conclusion, the two-adsorbate model developed in this chapter shows that tuning of the deposit composition can be straightforwardly achieved by varying the process parameters (electron beam dwell time, electron flux) in the presence of two adsorbed species. The tuneable composition window is determined by the adsorption and supply rate of each adsorbate as well as their electron-impact efficiencies and their non-volatile reaction products. This opens the door to the controlled tuning of specific composite compositions in nanosized deposits, allowing to tailor the physiscal properties of this material.

Chapter 5

Magnetic sensing properties

In this chapter, we systematically study the electrical and magnetic sensing properties of granular Co-C nano-Hall sensors fabricated by focused electron-beam induced deposition and compare them with the properties of focused ion-beam fabricated sensors. The Hall response to an applied external magnetic field is measured and discussed. This analysis allows access to material properties such as the extraordinary Hall resistivity at saturation, or the average nanocrystal size. The sensor performance is discussed and the Co-C nano-granular sensors are found to exhibit a high resolution to highly localized magnetic flux changes.

5.1 Introduction

FEB induced deposits of $\text{Co}_2(\text{CO})_8$ have been shown to consist of Co nanocrystals embedded in an amorphous carbonaceous matrix [18, 19]. The size of these nanocrystals is in the range of 2-5nm, which is below the critical dimension for single magnetic domain size, which is about 10nm for Co particles [142]. This makes this material superparamagnetic. At room temperature, the magnetization of the nanocrystals is not frozen along a given anisotropy direction. Rather, thermal energy is sufficient to reorient the magnetization of the single nanocrystals so that the average magnetization of the material is zero. Below a certain blocking temperature however, the magnetization of the nanocrystal would remain fixed and the material would exhibit a ferromagnetic behaviour. At room temperature, and in the presence of an external magnetic field, the magnetic moments of the nanocrystals are aligned and the material exhibits a high magnetization.

The electric transport in these nanocomposite films is dominated by strong intergrain scattering [37, 62]. Hence, the resistivity depends both on

the nanoparticle sizes (r) and their average spacing (d) [143]. It was shown that the extraordinary Hall effect can be strongly enhanced by augmenting the scattering in a ferromagnetic film [144], an effect known as the Giant Hall Effect (GHE). For this reason, there is an enhancement of the EHE in the Co:C nanocomposite structures when electronic conduction is taking place in a regime close to the percolation threshold.

The ability to deposit structures locally and with arbitrary geometry using FEBID, combined with the EHE found in CoC nanocomposite material, makes this material a very promising candidate for the use in Hall elements [20], allowing the detection of highly localized, spatially inhomogeneous magnetic fields produced by dipolar sources such as the magnetic beads used for biological assays [145], magnetic grains used in magnetic recording [146] or further applications where a high spatial resolution to magnetic fields is essential [147, 148].

In this chapter, we discuss the characteristics and performances of 26 FEBID Hall elements realized during this thesis. Their properties are compared to the properties of 7 FIBID Hall elements and 1 pure Co Hall element realized as references. We discuss the properties in light of the figures of merits for micromagnetic sensors used for bead detection, as introduced in section 2.2.3 and show that the nanocomposite CoC material obtained by FEBID of Cobalt carbonyl is suited for the fabrication of small size, high-resolution magnetic sensors.

5.2 Experiment

Hall sensors have been deposited by FEBID and FIBID of $\text{Co}_2(\text{CO})_8$ on Si substrates with a thermally grown oxide layer of 200nm thickness. Cr-/Au-electrodes were defined by lithography on the substrate with a gap of $2\mu\text{m}$ between them and FEBID was carried out between the electrodes, thus providing electrical contact to the deposited Hall structures (see figure 5.1). For the FEB induced deposition, a 25keV, 1nA beam was used. For the FIB induced deposition, a 30keV Ga beam with a current of 12pA was used. Deposition was carried out using the shortest experimentally available dwell time (100ns nominal) in order to reduce the effect of FIB milling on the deposit. The deposition parameters and geometries were varied. The lateral dimensions of the deposit were assessed on top-view SEM imaging, while the thickness of the deposits was measured on highly tilted high-resolution SEM images or using Atomic force microscopy (AFM). The deposited sensors had thicknesses in the range of a few tens to a few hundreds of nanometers. The as-deposited sensors exhibited widths between 200 and 500nm. A reference

sensor was fabricated by electron-beam lithography, electron-beam evaporation of Co and subsequent lift-off. This sensor had an nearly square active area of 1500nm side length and a thickness of 80nm.

For the magnetic characterization the sensors were placed in an electromagnet with a gap of about 10cm between the polar pieces. This allows to vary the angle between the field and the sample. The maximum external field produced is little above +/- 2T DC (for 150A). The Hall voltage response versus applied field was recorded at room temperature and with the applied field perpendicular to the sensor. The sensor was biased using a DC current source. The current was ramped until drift appears on the voltage due to Joule heating. This defines the maximum allowable sensing current I_{max} as introduced in 2.2.3. The electrical resistance was measured using the setup given in chapter 3. A grounded BNC box was used for ESD protection and provided a terminal for conducting 2-points measurement on the structure. The corresponding electrical resistivity values were then determined from the geometrical dimensions of the sensors.

5.3 Hall curve analysis

A typical voltage response of a FEBID sensor is shown in figure 5.2 and the typical response of a FIBID sensor is shown in figure 5.3. In the following we introduced the methodology used to analyze Hall voltage response to a magnetic field and link it to the magnetization in the Hall element.

5.3.1 Methodology

Linear fit of the Hall response

The Hall voltage measured under varying magnetic field is a measure of the Hall resistivity of the material as defined in equation (2.29) in chapter 2:

$$\rho_H = \rho_{OHE} + \rho_{EHE} = \mu_0(R_O H_z + R_S M_z) \quad (5.1)$$

where the coefficients R_O and R_S are the ordinary and extraordinary Hall constants, H_z is the applied field in the direction perpendicular to the Hall sensor and M_z is the magnetization of the sensor material in the direction perpendicular to the Hall sensor. The OHE depends linearly on the applied field H_z whereas the EHE depends on the magnetization M_z of the sensor. The Hall voltage is expressed from equation (5.1) by:

$$U_H = \rho_H \cdot \frac{l}{w \cdot t} I_{meas} = \mu_0(R_O H_z + R_S M_z) \frac{l}{w \cdot t} I_{meas} \quad (5.2)$$

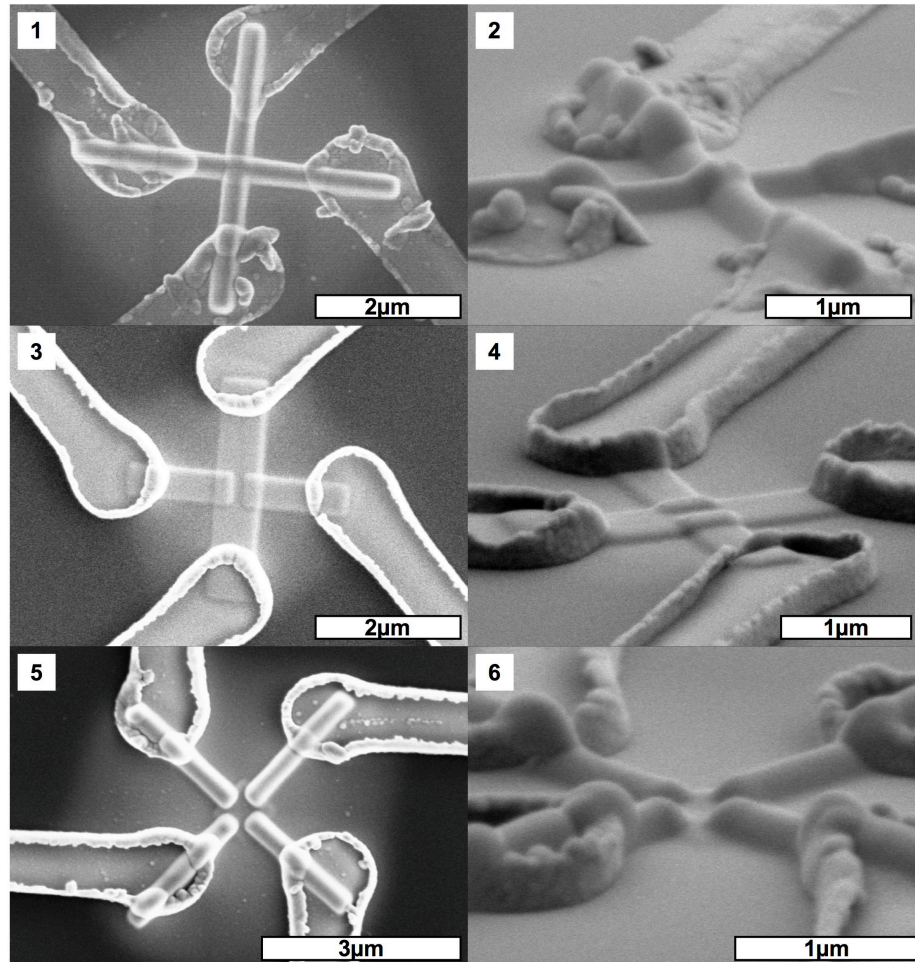


Figure 5.1: *Example of FEBID CoC Hall sensors geometries realized. 1) Simple two-lines Hall sensor. In the tilted view (2) it is apparent that the deposit is thicker at the active area. 3) and 4) (tilted view) Hall sensor consisting of three rectangular FEB induced deposits. The resistance in the longitudinal and transverse directions differ. 5) and 6) (tilted view) Hall sensor consisting of a thin active area contacted by four FEBID lines.*

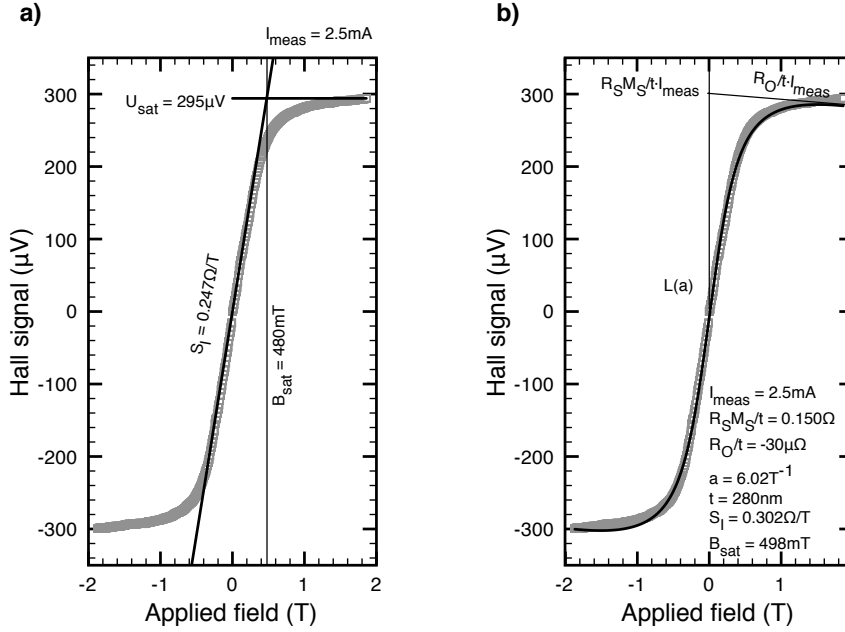


Figure 5.2: Typical Hall voltage response of a CoC nanocomposite FEBID sensor to an applied magnetic field and characterization using a) linear fits and b) Langevin fit. See text for details.

where l , w , t are the length, width and thickness of the sensor.

Accordingly, two regions can be distinguished in the Hall response as shown in figure 5.2. Around zero field, the response is driven primarily by the growing contribution of the EHE, leading to a high sensitivity S_I to the magnetic field. Above a certain saturation field B_{sat} , the Hall response decreases slowly, with a slope determined by the amplitude of the OHE. As a consequence, the two regions of the Hall response can be fitted linearly as shown in figure 5.2a. The sensitivity S_I , given by the slope of the Hall signal U_H close to zero applied field H , is retrieved from the Hall response by fitting the linear region around zero field in figure 5.2a:

$$S_I = \frac{1}{\mu_0} \left. \frac{\delta U_H}{\delta H} \right|_{H=0} / I_{meas} \quad (5.3)$$

It is also possible to fit the slope of the Hall response at high field ($B > B_{sat}$) to obtain the OHE constant R_O :

$$R_O/t = \frac{1}{\mu_0} \left. \frac{\delta U_H}{\delta H} \right|_{H > H_{sat}} / I_{meas} \quad (5.4)$$

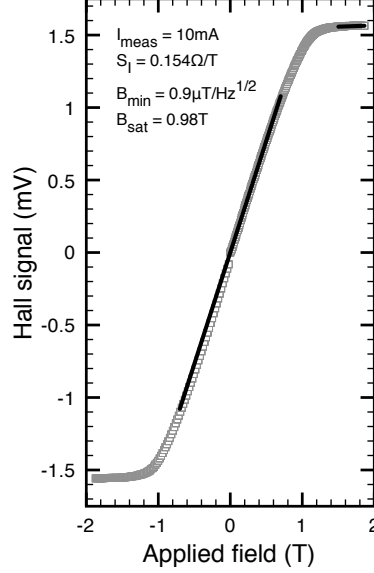


Figure 5.3: Typical Hall response of a CoC nanocomposite FIBID sensor and characterization using a linear fit.

valid for square sensor surfaces and where t denotes the sensor thickness. As has been seen in chapter 2, the OHE is dependent on the geometry of the sensor. However, as $\rho_{OHE} \ll \rho_{EHE}$ in the superparamagnetic material, the OHE is small as compared to the EHE ($|R_O/t| \ll |S_I|$) and can be neglected by approximating $U_H(H > H_{sat}) \approx U_{max}$.

The saturation field $B_{sat} = \mu_0 H_{sat}$ can be obtained from the intersection of the ordinary Hall response at high fields with the EHE response as is shown in figure 5.2a:

$$B_{sat} = \frac{U_{max}}{(R_O/t + S_I)I_{meas}} \approx \frac{U_{max}}{S_I I_{meas}} \quad (5.5)$$

Hence, a simple linear fitting routine allows to find values for the field sensitivity S_I and the saturation field B_{sat} . Knowing the dimensions of the Hall sensor, the OHE constant R_O can be obtained.

Langevin fit of the Hall response

As has been said in the introduction, the nanocomposite CoC material obtained by FEBID is granular and consists of Co nanocrystal with sizes be-

low 2-5nm which are embedded in a carbonaceous matrix [19, 134]. The nanoparticles are single domains and form films which are superparamagnetic at room temperature. If the interactions between nanoparticles are negligible, the magnetization of a superparamagnetic material is described by the Langevin theory for paramagnetism which describes the variation of the magnetization with the external magnetic field:

$$M_z = M_s L(\langle \mu \rangle \mu_0 H / k_B T) \quad (5.6)$$

where $L(x) = \coth x - 1/x$ is the Langevin function. Here, M_s is the saturation magnetization, k_B is the Boltzmann constant and T is the temperature. $\langle \mu \rangle$ is the average nanoparticle magnetic moment. The Langevin function describes the alignment of the magnetization of the single-domain Co nanocrystals to the applied field.

As is given by equation (5.1), the Hall voltage depends on the magnetization. Hence, $\rho_{OHE} \ll \rho_{EHE}$, the Hall voltage represents a measure of the magnetization in the active area of the Co-C sensor. For this reason, we fit the Hall response by a Langevin function using the following relation:

$$U_H = \mu_0 [R_O H + R_S M_S L(aH)] \frac{l}{wt} I_{meas} \quad (5.7)$$

where l , w and t are the dimensions of the active area of the Hall sensor and $a = \langle \mu \rangle \mu_0 / k_B T$ is the Langevin factor. As has been introduced before, R_O is the ordinary Hall coefficient, R_S is the extraordinary Hall coefficient, M_S is the saturation magnetization and I_{meas} is the measurement current passed through the sensor.

We now discuss which are the *independent* parameter set that can be obtained by the Langevin fit. For this, we assume a square Hall sensor active area, i.e. $w=l$, as well as knowledge of the measurement current I_{meas} . From the Langevin fit, the following independent parameters can be obtained (see figure 5.2b):

- The extraordinary Hall resistance at saturation $R_S M_S / t$, corresponding to the intercept of the linear extrapolation of the high-field response of U_H / I_{meas} with the y-axis, in units of Ω .
- The ordinary Hall resistance R_O / t , corresponding to the linear slope of the high-field response of U_H / I_{meas} , in units of Ω / T .
- The Langevin factor a as defined above, in units of T^{-1} , which is determined by the steepness of the low-field Hall response.

The saturation field B_{sat} and the sensitivity S_I can be derived from the fitted Langevin parameter sets, provided the thickness t (or, in the case of a non-square active area, the dimensions l, w, t) is known. For the derivation of these relation, we use the mathematical derivative of the Langevin function around zero given by $\delta L(x)/\delta x|_{x=0} = 1/3$. For square deposits and knowing the deposit thickness, one finds the expression for the field sensitivity S_I by derivation of equation (5.7):

$$\frac{1}{\mu_0} \left. \frac{\delta U_H}{\delta H} \right|_{H=0} = S_I \cdot I_{meas} = \frac{R_S M_S}{t} \cdot I_{meas} \frac{a}{3} \quad (5.8)$$

$$\Leftrightarrow S_I = \frac{R_S M_S a}{t \cdot 3} \quad (5.9)$$

Neglecting the contribution from the OHE and using the relation (5.9), the following expression for the saturation field B_{sat} is found:

$$U_{max} = B_{sat} S_I I_{meas} = \frac{R_S M_S}{t} I_{meas} \quad (5.10)$$

$$\Leftrightarrow B_{sat} = 3/a \quad (5.11)$$

The Langevin fit is shown in figure 5.2b for an example FEBID sensor and is compared with the linear fit. The fitted values for the field sensitivity S_I and the saturation field B_{sat} are found to be in good agreement. For comparison, a typical Hall response for the case of a FIBID CoC Hall sensor is shown in figure 5.3. It must be noted that for FIBID samples with Co concentration $\geq 70\text{at.}\%$, the assumption that the interactions between nanoparticles is negligible does not hold true and the observed behavior under magnetic field is not well described by a Langevin function.

Estimation of the average nanocrystal size using the Langevin fit

The Langevin fit of the Hall response yields access to the average nanocrystal magnetic moment $\langle \mu \rangle$, which is encoded in the Langevin factor a :

$$a = \langle \mu \rangle \mu_0 / k_B T \quad (5.12)$$

The magnetic moment per pure Co atom in a lattice has been measured to $n_B = 1.72 \mu_B$, in units of Bohr magnetons ($1 \mu_B = 9.28 \times 10^{-24} \text{J/T}$) [149]. Hence, one obtains the average number of Co atoms per nanocrystal:

$$\langle N \rangle = \langle \mu \rangle / n_B \quad (5.13)$$

The average nanocrystal volume is hence given by

$$\langle V \rangle = \langle \mu \rangle / n_B \cdot M_{Co} / (N_A \cdot \rho_{Co}) \quad (5.14)$$

where M_{Co} and ρ_{Co} are the molar mass and the density of Cobalt respectively and N_A is Avogadro's number.

Using the relation $\langle V \rangle = 4\pi/3\langle r \rangle^3$, one obtains the average particle radius:

$$r_{eff} = \sqrt[3]{\frac{3\langle \mu \rangle M_{Co}}{4\pi n_B N_A \rho_{Co}}} \quad (5.15)$$

It must be noted that the particle size r_{eff} represents an effective nanocrystal size [97] which may differ from the physical nanoparticle size r . It is an estimate of the nanocrystal size in the CoC nanocomposite, if we assume the nanocrystals are composed of pure Co. The effective nanocrystal size could be affected by the presence of a magnetically disordered, outer layer such as an oxide layer [150]. Hence, it can be said that the estimated particle size r_{eff} is dependent on the size of the Co nanoparticles, but also on their purity and on their texture. Furthermore, it represents the mean value of an unknown particle size distribution, which is however quite narrow as seen on TEM images [19].

The ratio between the spacing d and the size r of the embedded nanoparticles can be estimated for Co-C using a closed packed model, assuming a single-sized distribution of spherical particles, using [151]:

$$\frac{d}{2r} = \sqrt[3]{\frac{1}{P} \left(\frac{(1-x)\rho_{np}M_m}{x\rho_m M_{np}} + 1 \right)} - 1 \quad (5.16)$$

where x is the metallic atomic concentration in the carbonaceous matrix, M denotes the molar mass, ρ stands for the density, whereby the subscript m and np denote the insulating matrix and the Cobalt nanoparticles, respectively. $P \approx 1.35$ is the packing factor for close packing of spheres.

5.3.2 Saturation field

The relation between the Langevin and the linear fit approach is readily probed by comparing the saturation field obtained by equation (5.5) with the linear relation which is obtained if the Hall response is primarily governed by a Langevin relation (eq. (5.11)). The values for the saturation field B_{sat} measured by the linear fit are compared with the Langevin parameter a in figure 5.5a. Clearly, a linear relation following $3/a$ is visible for the FEBID sensors, which validates the Langevin fitting approach. Also, both FEBID and FIBID fabricated Hall elements are found to follow this relationship.

The saturation fields is related to the mean size of the nanoparticles r_{eff} , as the material is superparamagnetic so that the magnetization process is

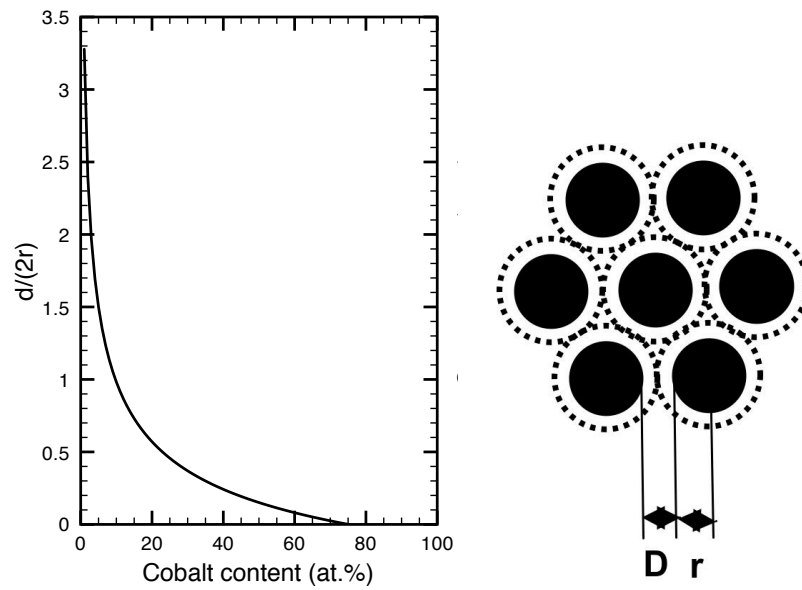


Figure 5.4: a) Dependence of the average distance d of nanocrystals normalized to their size $2r$ as a function of the Co content of the deposit. The ratio $d/(2r)$ is calculated using equation (5.16). Parameters are: $\rho_{np}=8.9\text{g/cm}^3$; $M_{np}=58.9\text{g/mol}$; $\rho_m=2\text{g/cm}^3$; $M_m=14$. Using this model, the percolation threshold ($d/(2r)=0$) is at 75 at.% Co. b) Schematic of the closed packed model for Co-C nanocomposite material.

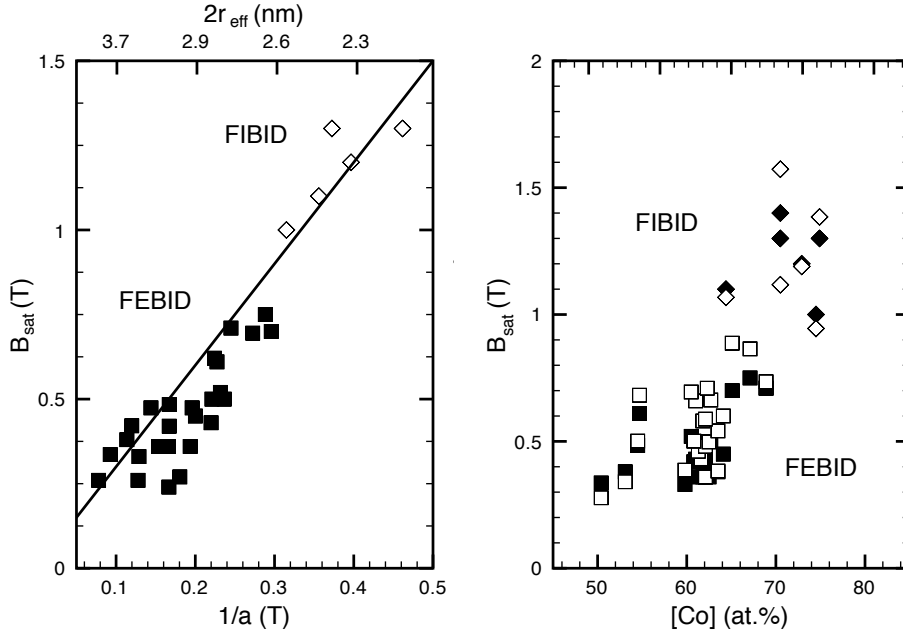


Figure 5.5: a) B_{sat} as a function of the inverse of the parameter a (from equation (5.7)), proportional to the effective diameter $2r_{eff}$ of the Co nanoparticles. The relation $B_{sat} = 3/a$ obtained for an ideal Langevin response is shown as a line. b) B_{sat} vs Co concentration, obtained for sensors from FEBID (squares), FIBID (diamonds) and evaporated Co (circles). B_{sat} is obtained from the linear fit of the sensor response around zero field (full symbols). For comparison, the value as obtained from the Langevin fit (see eq. (5.7)) are shown (outline symbols).

directly driven by the alignment of the single-domain nanoparticles under the influence of the external field as compared to switching the magnetization of a ferromagnetic layer. In particular, a dependence of the saturation field on the thickness is not found. The saturation field follows a relation $B_{sat} \propto 1/a \propto 1/\langle\mu\rangle \propto 1/r_{eff}$, as obtained from equations (5.11) and (5.15). It appears that during the FIBID process, smaller nanocrystals were obtained as compared to the FEBID process.

We also compare the saturation field B_{sat} to the Co concentration in figure 5.5b. The saturation field B_{sat} is increasing with the Co concentration. All of the FEBID realized Hall elements have saturation fields between a few hundreds mT and 1T, whereas the FIBID realized Hall elements exhibit saturation fields above 1T. The FIBID deposits had higher Co ratios than the FEBID deposits, and also higher saturation fields B_{sat} . However, we did

not observe hysteresis in the FIBID sensor Hall response. For this reason, we conclude that the FIBID material is still nanocomposite CoC but exhibiting smaller particle sizes.

For bead detection experiments, where a high biasing magnetic field is necessitated in order to magnetize the super-paramagnetic labels, saturation fields higher than 100mT are needed in order to prevent saturation of the sensor [13]. The high saturation fields obtained for FEBID and FIBID CoC Hall sensors are suited for these applications.

5.3.3 Extraordinary Hall resistivity at saturation

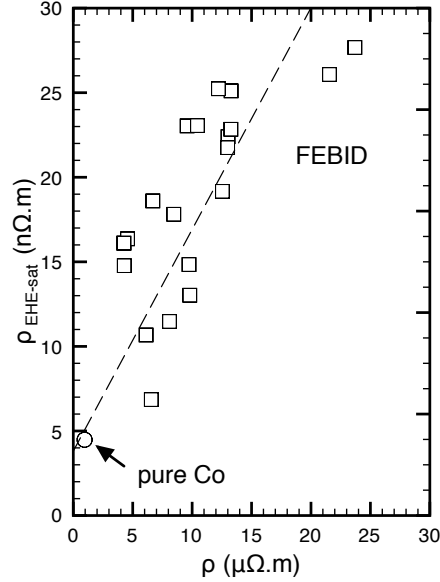


Figure 5.6: Extraordinary Hall resistivity at saturation $\rho_{EHE-sat}$ versus electrical resistivity ρ . Dotted line is a guide for the eye.

The Langevin fit gives access to the product $R_S M_S$, as has been shown in section 5.3.1. However, as the saturation magnetization M_S of the sensor remains unknown, it is not possible to extract the extraordinary Hall coefficient R_S solely from the Langevin fitting procedure. For this reason, we have calculated the *extraordinary Hall resistivity at saturation* as an alternative parameter which uniquely describes the magnetic sensing property of the material. We have obtained the extraordinary Hall resistivity at saturation

from the measurements using:

$$rho_{EHE-sat} = S_I B_{sat} t \quad (5.17)$$

We are now interested in how the Hall resistivity is linked to the longitudinal (electrical) resistivity. To this end, the electrical resistivity was estimated from the resistance as measured between 2 points of the Hall structure and using the sensor dimensions as measured on SEM images. In figure 5.6, the extraordinary Hall resistivity at saturation is plotted against the electrical resistivity for FEBID sensors. The values for the evaporated Co sensor are given as a reference. All FEBID samples exhibit both higher electrical and Hall resistivity as compared to the pure Co sample. The highest extraordinary Hall resistivity values are obtained for the highest electrical resistivity values.

The use of a 2-point setup for the assessment of the electrical resistance induce some error on the resistivity value. The FEB induced deposit contacts the Au electrodes from above and the quality of the electrical contact is subjected to caution, as the height of the electrodes (100nm) might prevent a continuous electrical pathway. On separate, dedicated 4-point electrodes, FEBID of Cobalt carbonyl was carried out as a reference and contact resistances in the order of 20Ω were reproducibly obtained. The FEBID Hall sensors on the other hand exhibit resistances of $\geq 150\Omega$. For this reason, we estimate the maximum error introduced by the use of a 2-point setup for the measure of the electrical resistivity to about 13%. The dimensions of the deposits were measured using an image processing software on high resolution, top-view and tilted SEM images. The error on the geometrical dimensions is estimated to roughly 10%. For the pure Co sample realized by evaporation, it appears the error is larger. We measured a resistivity of $1\mu\Omega\text{m}$ which compares to a reported resistivity of Co of $0.06\mu\Omega\text{m}$ at 20°C .

As can be seen in figure 5.6, within the limits of the error estimation, the Hall resistivity follows a linear relationship with the electrical resistivity. In a metal, the ordinary Hall effect is small, due to the high charge carrier density present. Hence, below saturation, its contribution can be neglected with respect to the extraordinary Hall effect [90]. The extraordinary Hall resistivity ρ_{EHE} is found to vary at saturation with the electrical resistivity ρ as [152]:

$$\rho_{EHE-sat} = \gamma\rho_0\rho_S + \gamma\rho_S^2 \quad (5.18)$$

where γ is a model coefficient. The electrical resistivity ρ has been decomposed using Matthiessen's rule in a spin-dependent, magnetic part ρ_S that

stems from spin-orbit scattering and a spin-independent, “ballast” scattering event induced contribution ρ_0 :

$$\rho = \rho_0 + \rho_S \quad (5.19)$$

Hence, variation of a parameter in a material exhibiting EHE leading to an increase in the electrical resistivity ρ affects the EHE: If the spin-dependent scattering term ρ_S is constant as the spin-independent scattering term ρ_0 increases, the EHE is expected to be a linear function of ρ_0 , as has been shown for Ni-SiO₂ films with increasing SiO₂ impurities [152].

The linear relationship observed between the Hall resistivity $\rho_{EHE-sat}$ and the electrical resistivity ρ points to an spin-independent scattering mechanism increase for increasing electrical resistivity. This observation is consistent with the scattering-limited electrical transport mechanism expected in this nanocomposite material [143], where the charge carriers undergo scattering at the interface between the Co nanocrystals and the carbonaceous matrix.

5.4 Sensor performance, magnetic field and magnetic flux resolution

The field sensitivity S_I is proportional to the small-field slope of the Hall signal curve. It is predominantly driven by the EHE. As can be seen in figure 5.7a, S_I showed large variations between 0.03 and 1.1 Ω/T for FEBID Hall elements which compares to values in the range between 0.015 and 0.5 Ω/T for FIBID or pure Co Hall elements. As the metal concentration approaches the metal-insulator transition, an exponential increase of the field sensitivity is recorded, which corresponds to the onset of the giant Hall effect (GHE).

Similarly, a decrease in the Cobalt concentration is found to increase the electrical resistivity ρ of the deposits, as shown in figure 5.7b for FEBID Hall structures. The increase in intergrain scattering due to the decrease in Cobalt concentration reduces the conductivity of the material. Of note is that the resistivity obtained experimentally for the “pure” Co is still approximately 20 times greater than that reported for the pure material ($5.6 \times 10^{-8} \Omega m$). This discrepancy is attributed to the use of an electrical 2-point measurement for the measure of the resistance, as the interface between the Au electrode and the evaporated Co structure might represent a step-coverage problem.

We now turn to the magnetic field resolution B_{min} , which represents the most important parameter for a Hall sensor with respect to its ability to discriminate small magnetic field changes. B_{min} is defined as the minimum

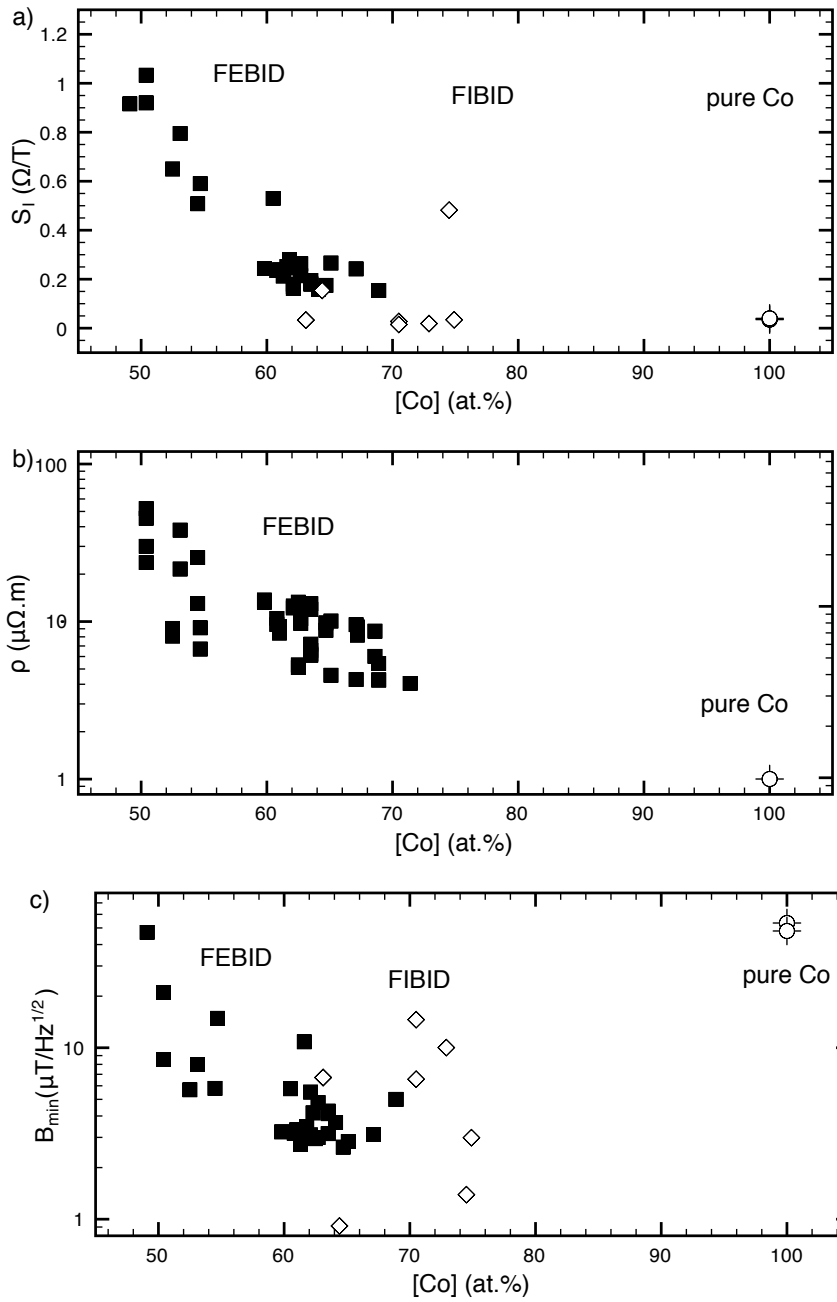


Figure 5.7: a) Field sensitivity S_I as a function of Co concentration, obtained for sensors from FEBID (squares), FIBID (diamonds) and evaporated Co (circles). S_I is obtained from the linear fit of the sensor response around zero field. b) Electrical resistivity ρ versus Co concentration. Electrical resistivity could not be represented in the case of FIB induced deposits in the absence of a clearly defined cross-section. c) Minimum magnetic field resolution B_{min} as a function of Co concentration.

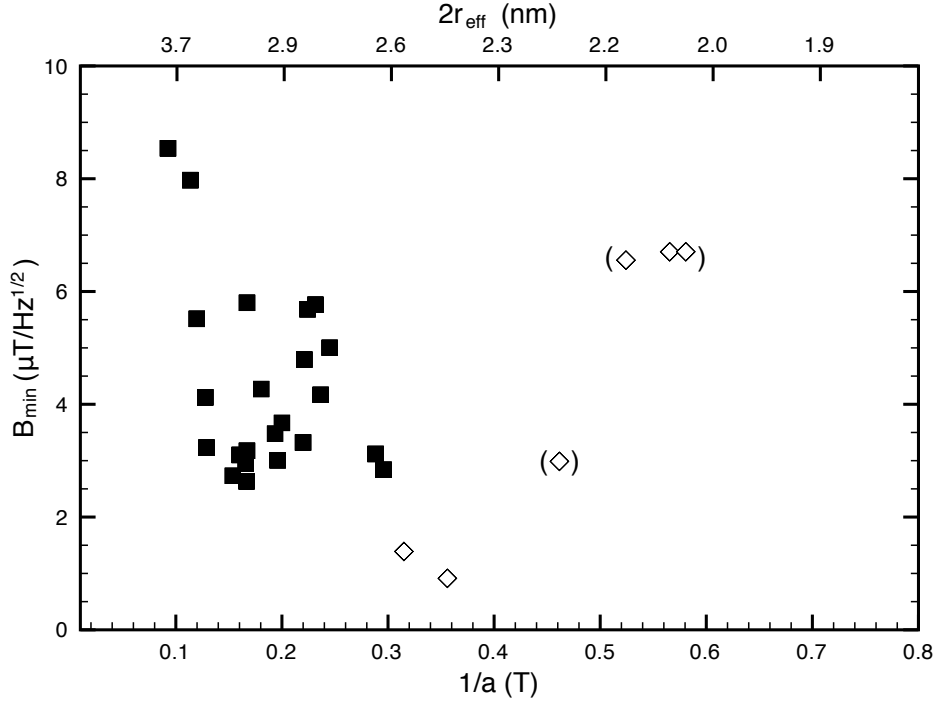


Figure 5.8: B_{min} versus inverse of the parameter a , obtained for sensors from FEBID (squares) and FIBID (diamonds). The high ($1/a$) value FIBID sensors are considered unreliable because the assumption of non-interacting nanocrystals does not hold true.

change in the magnetic field that will give a noticeable change in the Hall signal (see section 2.2.3). It is limited by the voltage noise δV . In figure 5.7c, we show the B_{min} values calculated taking the thermal noise regime as the ultimate limiting interference, as expressed in equation (2.25).

Sensors with lower Cobalt concentrations have a higher sensitivity S_I , but also a higher voltage noise δV . Therefore, the magnetic flux resolution B_{min} does not show a clear trend on Cobalt concentration, as can be seen in figure 5.7c. However, the sensors with the best resolutions (i.e. below $5\mu\text{T Hz}^{-1/2}$) had a local minimum at concentrations at around 65-75at.% Co. This value corresponds to a crossover between low electrical resistivity, hence low thermal noise and high allowable measurement current on one side, and high sensitivity to the magnetic field on the other side. The sensors with high S_I ($S_I > 0.4$, corresponding to sensors with a Co concentration $< 60\text{at.}\%$) had a strongly increased δV and a low I_{max} , resulting in a worse field resolution B_{min} .

Table 5.1: Comparison of the characteristics for micromagnetic Hall sensors. S_I is the magnetic field sensitivity (see equation (5.3)); B_{min} is the minimum resolvable magnetic field change in the thermal noise regime (see equation (2.25)) and Φ_{min} is the minimum resolvable change in magnetic flux in the thermal noise regime (see equation (5.20)). ϕ_0 is the flux quantum $\phi_0 = h/2e = 2.07 \times 10^{-15} \text{Tm}^2$. Table published in [97].

Ref.	Type	Width (nm)	S_I (V/AT)	B_{min} (nT/Hz ^{1/2})	Φ_{min}/ϕ_0
[108]	Si-GaAs	100	270	300	1.5×10^{-3}
[153]	InAs	1000	473	3500	1.8×10^{-3}
[154]	InGaAs	2000	700	400	8×10^{-4}
[105]	n-Si	2400	175	200	5.5×10^{-4}
[147]	FePt	160	325	166000	1.6×10^{-4}
[155]	Bi	50	4	80000	1×10^{-4}
[110]	InSb	500	370	720	9×10^{-5}
[103]	InAsSb	1000	2750	51	2.5×10^{-5}
[97]	Co-C	100	0.15	1000	4.5×10^{-6}

A clearer trend is obtained when comparing the minimum field resolution B_{min} with the inverse of the Langevin factor a , proportional to the particle size. As can be seen in figure 5.8, the lowest B_{min} values were obtained for smallest nanoparticles, which is in agreement with the theoretical predictions of an enhanced extraordinary Hall resistivity with reduced particle size [97].

For the detection of highly localized and spatially close magnetic dipole, the relevant parameter is the magnetic flux resolution Φ_{min} given by:

$$\Phi_{min} = B_{min} \times A \quad (5.20)$$

where A is the active area of the sensor [156].

In order to improve this resolution, the Hall elements fabricated by focused particle beam induced deposition can be further reduced in size. As has been shown in chapter 4 however, reducing the size of the as-deposited FEBID structure below the diffusion length of the hydrocarbons will lead to higher hydrocarbon uptake in the deposit when deposition is carried out in a HV chamber. For this reason, we applied a size-reduction using FIB-milling [108] down to active areas $(100\text{nm})^2$ in dimension. For the sensors investigated, the size reduction was not found to lead to a reduced field sensitivity S_I . This represents a clear advantage as compared to semiconducting Hall devices where ion implantation during the modifications using FIB milling will lead to a reduced sensitivity and an increase in noise level [109]. We compare the minimum field resolution and minimum magnetic flux resolu-

tion in table 5.1. Although the minimum field resolution of our sensors is found to be worse than that of semiconducting devices [89], the magnetic flux resolution obtainable by the CoC nanocomposite Hall sensors compares favorably.

5.5 Conclusion

In this chapter, we have shown how to apply Langevin analysis to the CoC FEBID Hall sensors. We extracted the saturation fields, which are sufficiently high to allow for high magnetizing fields in view of the application of these sensors in superparamagnetic bead detection. The saturation extraordinary Hall resistivity is found to correlate with the electrical resistivity, as predicted by the extraordinary Hall theory in nanocomposite materials. The sensitivity of these sensors to the magnetic field is evaluated. Due to the possibility to microfabricate magnetic sensors with dimensions down to 100nm, the sensitivity to a highly localized magnetic flux change is found to be the highest reported so far.

Chapter 6

Single-bead detection using FEBID Co-C Sensor

6.1 Introduction

The detection of superparamagnetic beads is a promising field for applications in medical diagnostics [157] where they are used as tags for molecular species. Two different diagnostic situations can be addressed: the measurement of the *concentration* of a specific biochemical agent, which requires relatively large sensor active surfaces providing the possibility for several microbeads to aggregate and subsequent bead “counting” [157]; on the other hand, the ultimate detection limit for the presence of highly diluted species is given by the ability to detect just a *single* superparamagnetic bead [80, 117]. Furthermore, the use of single beads in molecular motors [158] requires the possibility to track the position of the superparamagnetic bead with respect to the sensor surface.

As has been shown in chapter 5, Co-C sensors realized by FEBID are able to measure highly localized magnetic fields, as they have a high spatial resolution towards changes in the magnetic flux. Such highly localized, weak magnetic fields are typical of experimental situations in biomolecular assays which work with super-paramagnetic, micron-sized beads acting either as tags for molecular detection or as transducers allowing single-molecule manipulation [13, 78]. We prove the Co-C FEBID sensor’s magnetic sensing properties by demonstrating the magnetic detection of a single, super-paramagnetic, micron-sized bead.

At first, we perform experimental single-bead detection using the Co-C FEBID sensor. This is done *ex-situ* where the presence or absence of a single microbead on the sensor surface is reliably assessed by the magnetic sensor

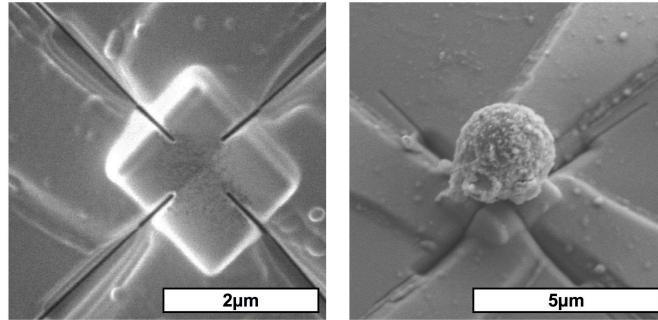


Figure 6.1: a) FEBID CoC Hall sensor used for the bead detection experiment. A $2 \times 2.5 \mu\text{m}^2$ rectangle was deposited by FEBID and subsequently reduced in size using FIB milling. b) FEBID Hall sensor with a Dynabead M-280 placed on its surface for the ex-situ bead detection experiment.

signal in the presence of an AC+DC magnetic field. The experimental data are discussed in terms of the microbead magnetization model introduced in section 2.2.1. Finally, a novel, *in-situ* bead manipulation and detection platform, combining an AC magnetic field and a nanomanipulation setup in a SEM, allows to conduct magnetic distance measurements where the distance between the sensor's surface and the paramagnetic microbead is correlated to changes in the magnetic field as seen by the magnetic sensor.

6.2 Experimental setup

6.2.1 Sensors and microbeads

For bead detection, sensors were fabricated by FEB induced deposition of CoC squares onto predefined Au/Pt electrodes on Si chips with a 200nm thermal oxide layer (see chapter 3). The FEB induced squares were subsequently FIB-milled in order to reduce the active area of the sensors (see table 6.1). It appeared that such FIB-milling also led to an increase in the maximum measurement current I_{max} that could be passed through the sensor before thermal drift occurs. This effect was attributed to Ga implantation in the SiO₂ layer increasing its thermal conductivity. The Si chips were then fixed with silverpaint onto a ceramic leadless chip-carrier (LCC04419 from Spectrum Semiconductors) with 44 contacts, of which 16 were electrically contacted by wire-bonding to the on-chip Au/Pt pads. Connections to the measurement apparatus was provided by means of a home-made printed circuit board (PCB) providing a 25-pins D-Subminiature connector and a

home-made 16 BNC sockets switch-box.

Greatest care had to be taken not to subject the sensors to electrostatic discharge (ESD). As the FEB induced deposit was the part of the electric pathway exhibiting the highest impedance, an electrical discharge such as one produced by friction or by plugging an apparatus to the shared power line would easily lead to the destruction of the FEB induced deposit. For this reason, the switch-box was designed allowing to easily ground the electrical connections to the sensor as long as it was not in use. The switch-box also allowed to contact different sensors on the same chip (see chapter 3).

The detection experiments were carried out using the Dynabead M-280 microbeads (Invitrogen Inc.). They have a diameter of $2.8\mu\text{m}$ and consist of a polystyrene matrix. The magnetic nanoparticles are made of maghemite (Fe_2O_3) and vibrating sample magnetometry (VSM) measurements are found in the literature [83] (see section 2.2.1).

The characteristics of the CoC Hall sensors used for the detection experiments are given in table 6.1, along with experimental parameters of the AC magnetic field.

6.2.2 Magnetic fields

Ex-situ experiment

An AC magnetic field was created using a home-made electromagnetic coil placed above the sensor, creating an AC field perpendicular to the sensor surface. For in-situ detection, the coil was placed below the sensor (see figure 3.9). A current of 2A was delivered to the coil by a power amplifier (Hero PA508X power amplifier, Rohrer Munich) which could deliver up to $\pm 50\text{V}$, $\pm 10\text{A}$ electrical power with a 200kHz bandwidth. We were limited in the maximum power we could pass through the coil as the coil would noticeably heat up for higher currents. The coil was operated at a frequency of $f_0=172.6\text{Hz}$ (ex-situ) and $f_0=17.3\text{Hz}$ (in-situ), which was set using a waveform generator (Hewlett-Packard 33120A). The low frequency was chosen to limit electromagnetic coupling. For the generation of DC magnetic fields, we have used different stackings of NdFeB permanent magnets placed below the sensor with different gaps with respect to the sensor to generate a variable DC magnetic field. In order to calibrate the DC magnetic field produced by the NdFeB at different gaps we used commercial magnetic sensors (Honeywell SS94A1 with a sensitivity 50mV/mT and SS94A2D with a sensitivity of 10mV/mT) placed on the PCB at the position of the CoC Hall sensor. The AC magnetic field was calibrated using the detection (CoC Hall) sensor.

The sensor response was first recorded in the absence of the microbead

Table 6.1: Characteristics of CoC FEBID sensors and AC field parameters used for bead detection. The sensitivity S_I , the magnetic field resolution B_{min} and the magnetic flux resolution Φ_{min} are the figures of merit introduced in section 2.2.3. ϕ_0 is the flux quantum $\phi_0 = 2.07 \times 10^{-15} \text{ Tm}^2$.

	Ex-situ detection	In-situ detection
Active area	$600 \times 600 \text{ nm}^2$	$500 \times 500 \text{ nm}^2$
Sensitivity S_I	91 mV/AT	36 mV/AT
Sensing current I_{sens}	10 mA	15 mA
Electrical resistance R	34.6Ω	35.6Ω
Magnetic field resolution B_{min}	$0.8 \mu\text{V/Hz}^{1/2}$	$1.4 \mu\text{V/Hz}^{1/2}$
Magnetic flux resolution Φ_{min}	$1.4 \times 10^{-4} \phi_0$	$1.7 \times 10^{-4} \phi_0$
AC magnetic field B_{ac}	7.6 mT	11.9 mT
Excitation frequency f_0	172.61 Hz	17.261 Hz
Induced signal U_{ind} at f_0	$230 \mu\text{V}$	$720 \mu\text{V}$

for different DC fields, in order to obtain the zero-level of the measurement. This is to ensure a correct interpretation of the experiment knowing that the sensor response $S_I(B)$ is not linear with the applied field (see chapter 5). Also, a possible influence of cross-talking between the AC and DC field can be eliminated through this zeroing routine. Then, a microbead was placed on top of the center of the sensor using a micromanipulation setup in a SEM (see figure 6.1) for the actual bead detection.

In-situ experiment

For the in-situ bead detection experiment, the home-made coil was placed inside the chamber of a SEM as described in chapter 3. A low-remanence nanocomposite magnetic core (E450-40, MicroMetals) was placed in the coil to enhance the magnetic field. The coil was situated below the sensor. Above the sensor, a home-made nanomanipulation setup providing three piezo axis (Smaract GmbH) allowed the precise manipulation of a commercial non-contact AFM tip (MikroMasch NSC15, spring constant 40N/m). The tip was used as a micromanipulation tool for the precise placement of a microbead.

6.2.3 Hall signal recovery using Lock-in amplification

With respect to the initial waveform generator output, the power amplifier and the impedance of the coil induce a phase shift on the signal. Because of inductive coupling between the coil and the measurement setup, the signal at the Lock-in amplifier consists mainly (in terms of amplitude) of an inductive,

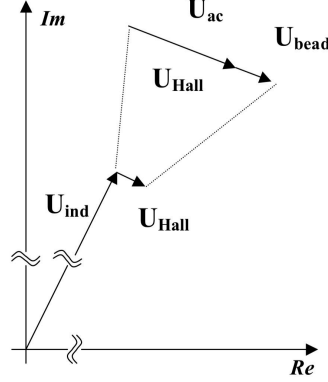


Figure 6.2: Schematic representation of the amplified signal. The most prominent contribution is the inductive signal U_{ind} which is in the order of hundreds of microvolts. The Hall signal U_{Hall} is perpendicular (in terms of phase) to the inductive signal and is in the order of some microvolts. The Hall signal is constituted by the measure of the AC magnetic field U_{ac} and by the actual signal induced by the microbead U_{bead} which is in the order of $\leq 1\mu V$.

parasitic signal U_{ind} . The useful Hall signal U_{Hall} is orders of magnitude lower than this inductive signal (see figure 6.2). As a result of the Hall signal being out-of-phase by 90° with respect to the inductive signal, the *amplitude* of the total signal $U_{ind} + U_{Hall} = \sqrt{U_{ind}^2 + U_{Hall}^2} \stackrel{U_{ind} \gg U_{Hall}}{\approx} U_{ind}$ is almost insensitive to the Hall signal.

In order to discriminate the small Hall signal, a lock-in (EG&G 7260 DSP), where the output of the Hall sensor is demodulated at a frequency f_0 , was used. A time constant of 1s and a filter slope of 12dB/octave, corresponding to an equivalent noise bandwidth of 167mHz [159], were used. As the Hall signal is out-of-phase by 90° with respect to the inductive signal, we had to calibrate the phase of the inductive signal first. In order to do this, the Hall signal was set to zero by setting the measurement current to zero, which does not affect the inductive signal. Once the phase was calibrated, the Hall signal could be measured at 90° (in terms of phase) of the much bigger inductive signal.

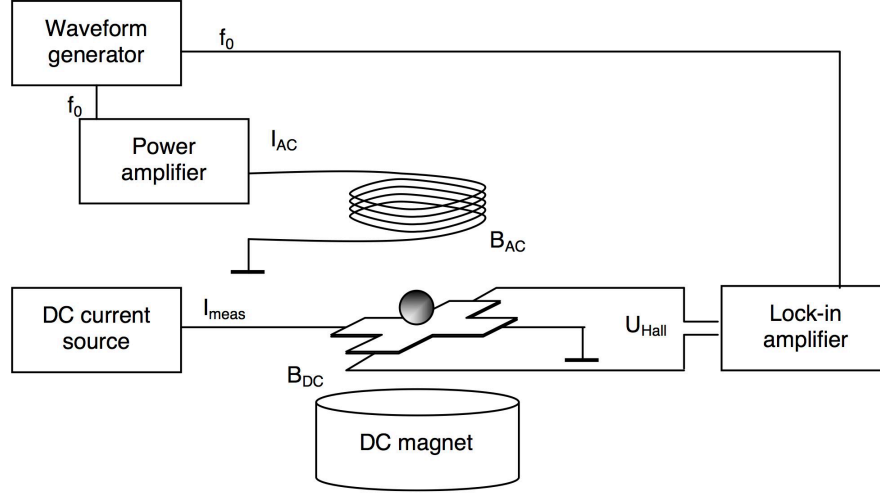


Figure 6.3: Schematics of the bead detection setup used for ex-situ measurements: the DC field is varied by changing the gap between the permanent magnet and the sensor; the AC field is generated with a macroscopic coil placed above the substrate. Adapted from [105].

6.3 Ex-situ single-bead detection

6.3.1 Detection scheme

For the ex-situ bead detection experiment, an AC, phase-sensitive detection scheme, previously shown in [105] with a CMOS Hall sensor, has been used (see figure 6.3). To this end, the sensor chip is placed in a perpendicular AC magnetic field B_{ac} that is modulated at a frequency f_0 . An inductive voltage is measured and the phase is calibrated. The sensor is then biased with a measurement current I_{meas} and the Hall voltage is measured at the frequency f_0 . In the presence of an AC magnetic field B_{ac} oscillating at frequency f_0 , the magnetization of the bead will follow the external field up to a cut-off frequency given by the magnetization dynamics. The microbead is superparamagnetic, thus its magnetization follows a Langevin relation (see chapter 2). This makes the peak-to-peak AC amplitude of the bead magnetization dependent on the DC field, as the Langevin magnetization curve is highly non-linear with respect to the magnetizing field. Hence, the ability for the bead to “follow” a sinusoidal, external magnetic field is decreasing with increasing DC field as the microbead saturates. In other words, the AC field variations of the microbead are a local measure of the slope of the Langevin

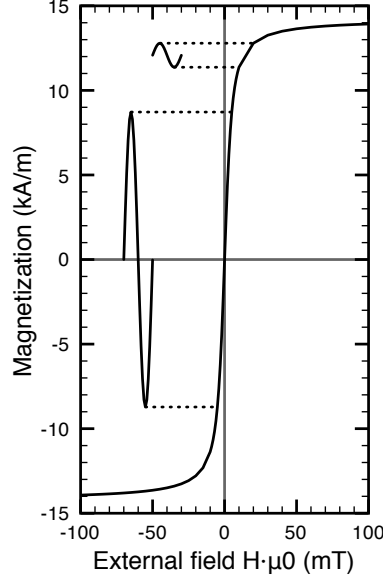


Figure 6.4: Model bead response to a 10mT peak-to-peak sinusoidal excitation in the case of 0mT DC field and 15mT DC field.

magnetization (see figure 6.4). At sufficiently high DC fields, the microbead is invisible to the magnetic sensor, whereas at zero field, full bead signal (determined by the magnetic susceptibility at low field) is expected. This single-bead detection scheme has been introduced and demonstrated with Hall sensors based on CMOS technology [105] and was used for subsequent single-bead detection using Hall sensors [110, 111, 153].

6.3.2 Results

Ex-situ bead detection is shown in figure 6.5. The AC magnetic excitation field B_{ac} is on at all time. At time $t=0s$, the measurement current is gradually increased from 0 to I_{meas} . Full measurement current is reached at approximately time $t=7s$. The Hall offset given by the AC excitation field is given by the measurement with a DC field of 64mT which saturates the microbead and cancels its AC contribution to the Hall signal. The bead signal is given by the difference of the Hall signal at zero DC field and the Hall offset.

Several measures were taken at different DC fields. The Hall signals with and without bead under increasing DC fields are shown in figure 6.6. At zero field, the Hall contribution corresponding to the low-field susceptibility

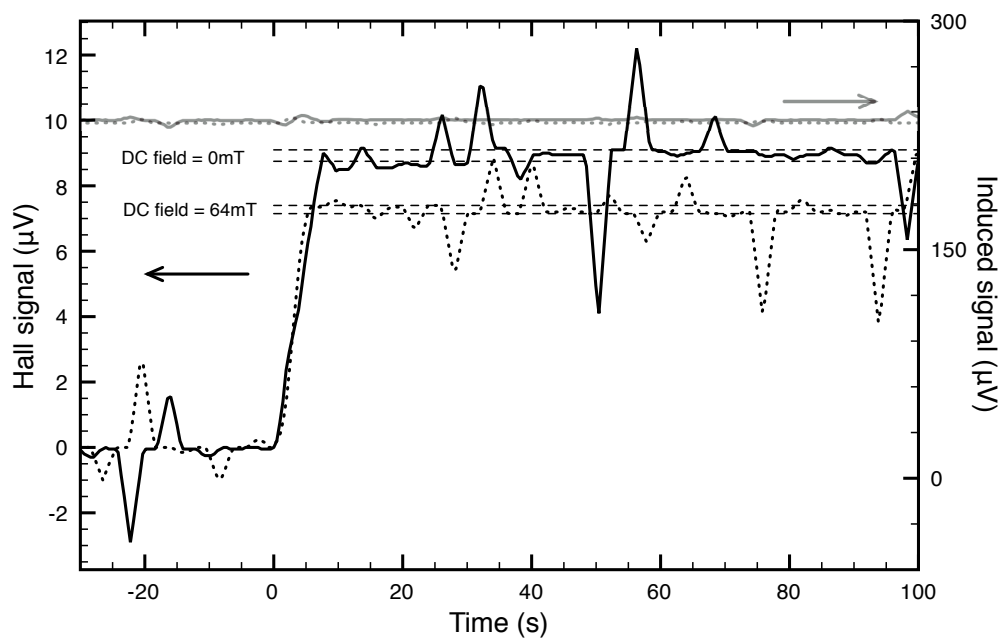


Figure 6.5: Hall signal versus time (black lines, left-hand axis) and induced voltage (grey lines, right-hand axis) in a DC field of 0mT (full lines) and 64mT (dotted lines). The sensing current is switched on at time $t=0$

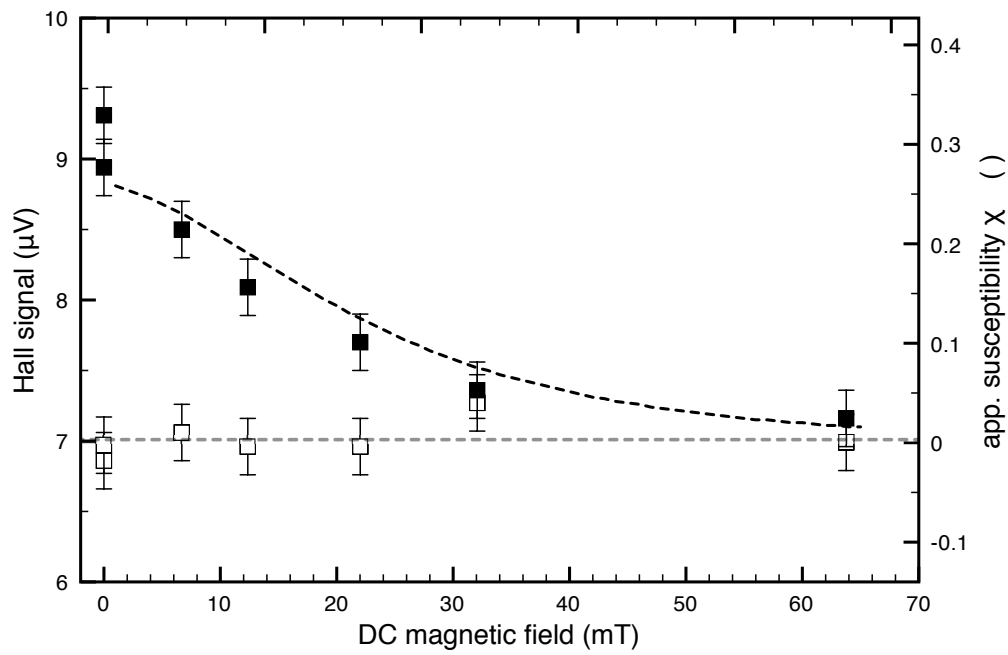


Figure 6.6: Hall signal versus DC magnetic field and model (equations (6.4) and (6.5)). Right-hand axis shows corresponding apparent susceptibility χ_{app} (see equation (6.3)).

of the bead is clearly measurable, but vanishes as the DC field is increased and the microbead saturates.

6.3.3 Discussion

Limitation by the magnetic induction

According to Faraday's law of magnetic induction, any closed electric loop which is subjected to a *perpendicular* alternating magnetic field will pick up an inductive voltage U_{ind} proportional to the integral of the magnetic flux variation times the surface enclosed by the electric loop. The signal from the sensor can hence be expressed as:

$$U_{sensor} = U_{ind} + U_{Hall} \quad (6.1)$$

where U_{ind} is the induced voltage and U_{Hall} is the Hall signal. The induced voltage U_{ind} is given by:

$$U_{ind} \propto \frac{\delta\Phi_{wire}}{\delta t} \cdot B_{ac} \propto \Phi_{wire} \cdot f_0 \cdot B_{ac} \quad (6.2)$$

where Φ_{wire} is the magnetic flux crossing the area defined by the electrical connections of the sensor. As Φ_{wire} has the same phase as B_{ac} , the term $\delta\Phi_{wire}/\delta t$ adds $\pi/2$ to the phase of the inductive signal with respect to the excitation field B_{ac} . The second approximation in equation (6.2) $\delta\Phi_{wire}/\delta t \propto \Phi_{wire} \cdot f_0$ is valid for a sinusoidal variation of the magnetic flux.

Ideally, one would like to reduce the induced voltage to zero, so that the signal from the sensor would consist of the (useful) Hall signal only, allowing higher amplification. However, the excitation field B_{ac} cannot be reduced without also reducing the magnetic signal from the bead, as the AC signal of the bead follows the excitation field. Hence, equation (6.2) tells us that in order to reduce the induced voltage, one can either work at lower frequencies f_0 , at the cost of increasing the low-frequency electrical noise, or reduce the magnetic flux Φ_{wire} crossing the electric loop defined by the macroscopic connections to the sensor. The latter option could be implemented by either reducing the electrical loop defined by the sensor, i.e. providing long, narrow-spaced microcontacts to the sensor, hence reducing the surface through which the induced voltage is *picked up*, or by reducing the surface through which the magnetic field is *generated*, by providing some kind of on-chip magnetic coil [99, 123, 160, 161] which could be used for the *local* generation of the AC magnetic excitation field. Another solution is to modulate the sensing current I_{meas} at a frequency f_I different from the magnetic excitation frequency f_0 , and detecting the Hall signal at the corresponding sidebands $f_0 \pm f_I$,

away from the electromagnetic signal produced at the frequency f_0 and its harmonic.

As a consequence of our experimental setup (both macroscopic electric connections defining a loop with some cm^2 area and macroscopic AC magnetic field generated by a coil with diameter in the cm range), the main limitation with using a perpendicular magnetic field source was the high level of inductive voltages induced in the setup. In our setup, the inductive voltage was in the hundreds of μV range (for mT excitation and frequencies below 200Hz, see figure 6.5, grey lines), which compares to an effective Hall signal in the 100nV range (see figure 6.6). This imposes severe constraints on the read-out electronics, because any amplification also amplifies the inductive signal. In order to partly overcome this issue, we reduced the AC frequency f_0 in order to minimize the ratio between induced voltage and Hall signal to about 10^2 . However, this increases the measurement noise, as the measurement is carried out in the $1/f$ noise frequency range.

Bead susceptibility and geometrical factors

We now turn to the useful Hall signal as represented in figure 6.6 and separate the *material properties* of the microbead (the bead susceptibility) from the geometrical effects, which are described by a geometrical factor.

Knowing the Hall voltage at bead saturation $U_{Hall}(B_{dc} \rightarrow \infty)$, it is possible to introduce an *apparent* susceptibility given by [105]:

$$\chi_{app}(B_{dc}) + 1 = \frac{U_{Hall}(B_{dc})}{U_{Hall}(B_{dc} \rightarrow \infty)} \quad (6.3)$$

The apparent susceptibility is shown on the right-hand axis of figure 6.6. B_{ac} plays the role of a small local probing field and B_{dc} of a bias field. Hence, the apparent susceptibility represents an upper-bound estimate, as it implies that the probing excitation field B_{ac} is small enough to provide a linear sampling of the susceptibility. In our case, $B_{ac}=7.6\text{mT}$, necessary to obtain a sufficient SNR for bead detection, is small enough to probe the apparent susceptibility around zero in the linear regime, as can be inferred by comparison of the Dynabead magnetization measurements shown in figure 2.13. However, it must be noted that the apparent susceptibility $\chi_{app}(B_{dc})$ is not strictly a material property but is also dependent on the sensor geometry and the bead-sensor distance.

In order to separate this geometrical influence, and to retrieve the microbead susceptibility χ from the data in figure 6.6, we start by decomposing the Hall signal into two terms:

$$U_{Hall} = S_I I_{meas}(B_{ac} + B_{sens}) \quad (6.4)$$

where the first term corresponds to the measurement by the Hall sensor of the excitation field B_{ac} , while the second term is the measure of the bead's magnetic field, which ultimately represents the signal of interest (see scheme in figure 6.2). We apply the magnetic dipole moment to describe the magnetic field generated by the magnetization of the bead. The bead signal U_{bead} is the signal corresponding to the bead magnetic field B_{sens} as seen by the sensor which was introduced in equation (2.20). Assuming in first approximation that the local bead field can be averaged over the sensor surface, one can write:

$$\begin{aligned} U_{bead} &= S_I \cdot I_{meas} \cdot B_{sens} \\ &= S_I \cdot I_{meas} \cdot C \cdot \mu_0 \left. \frac{dM}{dB} \right|_{B=B_{dc}} \cdot B_{ac} \end{aligned} \quad (6.5)$$

where C is a dimensionless coupling coefficient which quantifies the sensor's ability to convert the bead's magnetic field into a measurable Hall voltage [85]. The term $\mu_0(dM/dB)|_{B=B_{dc}}$ in equation (6.5) corresponds to the magnetic susceptibility $\chi(B_{dc})$ of the bead. The susceptibility is non-linear and depends on the level of saturation of the bead, i.e. on the magnetic DC field applied. Therefore, for negligibly small excitation fields B_{ac} , the measure of the Hall voltage under increasing DC bias field B_{dc} represents a direct measure of the bead's susceptibility χ [85, 105], provided the sensor sensitivity S_I is constant in the range of applied B_{dc} fields (i.e. provided the sensor does not saturate) and one has access to the coupling coefficient C .

The coupling coefficient C can be obtained by [85]:

$$C = \frac{R^3}{3w^2} \int_{-w/2}^{w/2} \int \frac{2(R + z_{offset})^2 - x^2 - y^2}{(x^2 + y^2 + (R + z_{offset})^2)^{5/2}} dx dy \quad (6.6)$$

where R is the radius of the bead, w is the sensor width and z_{offset} is the geometrical offset between the bead surface and the sensor surface. The coupling coefficient C is essentially a geometric factor which depends on the miniaturization of the sensor and on the bead's size (to the extent that this sets the lower limit of the distance between the center of the dipole and the surface of the sensor).

The effective distance between the sensing element and the bead is of high importance for the experimental and theoretical determination of the bead signal U_{bead} . For this reason, an offset z_{offset} is included in the analytical expression (equation (6.6)). In any microfluidic application, the sensor has to be protected from the aqueous environment by deposition of a insulating layer. Its thickness will determine the offset z_{offset} . However, in *thick* (i.e.

non-2D) sensors, the thickness of the sensor itself might play a role. Conceptually, in this case a convolution between the current distribution and the response to the highly localized magnetic field of the Dynabead takes place. The sensing current will be distributed throughout the thickness of the sensor, depending on the local electrical resistivities, while the bead magnetic field is also non-linear at this scale. The knowledge of the exact distribution of the current lines in the sensor could be implemented by FEM simulations, assuming uniform resistivity. This approach was qualitatively proposed in [111] and highly non-uniform current distribution were predicted. However, it proves sufficient to make the assumption that the current distribution is uniform and that the sensing layer of the FEB induced deposit is concentrated at some height in the deposit.

Under the condition $w \ll R$, i.e. the sensor used for detection is smaller than the bead, the average bead field can be approximated by the maximum bead field below the bead as the error induced by this estimation vanishes as the sensor width decreases (see figure 2.15):

$$U_{bead} \approx S_I \cdot I_{meas} \cdot \left[\frac{\mu_0 \Delta m}{4\pi(R + z_{offset})^3} \right] \quad (6.7)$$

where

$$\begin{aligned} \Delta m &= m(B_{dc} + B_{ac}) - m(B_{dc}) \\ &= m_{sat} \left[\coth[\alpha(B_{dc} + B_{ac})] - \coth(\alpha B_{dc}) + \frac{B_{ac}}{\alpha B_{dc}(B_{dc} + B_{ac})} \right] \end{aligned} \quad (6.8)$$

using the Langevin bead magnetization description (equations (2.11) and (2.14)).

The bead signal given in figure 6.6 was fitted using equations (6.7) and (6.8), obtaining two independent fit parameters z_{offset} and χ . The fit relies on knowledge of the saturation magnetic moment m_{sat} , which is given by the bead volume and the density of the ferrite nanoparticles in the microbead. We used a typical value of $m_{sat} = 1.7 \times 10^{-13} \text{ Am}^2$ (see table 2.1). The same value was used for fitting the bead magnetization data in [83] and [105], to which our findings are compared to in table 6.2. A fitted susceptibility $\chi=0.73$ is found. This susceptibility compares with the vibrating sample magnetometry measurements in [83] of $\chi = 0.5$. However, it differs by a factor of four as compared with the values found for a single Dynabead M-280, using the same approach as here, in [105], where the authors reported a susceptibility of $\chi = 2.8$. This is however consistent with the reported dispersity of magnetic properties for Dynabeads M-280 [157], where the standard deviation of twelve independent measurements of the magnetic signal induced

Table 6.2: *Properties of Dynabead M-280 microbeads. The susceptibility χ is calculated according to equation (2.17) and the average nanoparticle magnetic moment m_p is calculated using equation (2.16). For the saturation magnetic moment, a typical value of $m_{sat} = 1.7 \times 10^{-13} \text{ Am}^2$ was used. $\chi_0 = \chi(B_{dc} = 0)$ denotes the magnetic susceptibility at zero field.*

Source	Method	α $\text{Am}^2 \text{J}^{-1}$	χ_0	m_p Am^2
[83]	VSM	80	0.5	3.3×10^{-19}
[105]	Langevin fit	448	2.8	1.85×10^{-18}
our data - ex-situ	Langevin fit	116	0.73	4.8×10^{-19}
our data - in-situ	Langevin fit	95	0.60	3.9×10^{-19}

by single Dynabeads M-280 was found to be 72% (the corresponding value for the susceptibilities listed in table 6.2 is 95%, but on a smaller statistical basis).

The fitted z_{offset} is 250nm. This compares to the difference between the heights of the electrode and the deposit, as obtained by AFM measurement (300nm). In other words, the unknown current distribution in the thick sensor can be reasonably approximated by assuming that the FEB induced deposit higher than the Au electrodes acts as a geometrical spacer. This coarse estimation proves sufficient to fit the model with the experimental data.

Comparison with other microsensors used for bead detection

A selection of single-bead detection experiments reported in literature is shown in table 6.3. The table reports the publications of single-bead detection where sufficient experimental details were presented for comparison with our results. The publications from the spin-valves group of Prof. Freitas in Lisbon ([87, 99, 116]), from the group at Philips Research Lab, using GMR devices ([123, 161]), from Tokyo Institute of Technology ([107, 110]), from Florida State University ([85, 153]), and one report from IMEC Belgium ([160]) are shown.

The coupling parameter C is compared, by calculating both the theoretical value (equation (6.6)) and the experimental value (equation (6.5) using the susceptibilities given in table 2.1). Clearly, it appears that the coupling factor C is maximized when using small active area sensors, as in our case. However, the integration of a passivation layer as required for use in a microfluidic environment leads to a reduction in the coupling factor.

FEBID is an advantageous pathway for the fabrication of sub-micrometric Hall sensors due to the possibility to fabricate small active area surfaces without loss of sensitivity. This represents an inherent advantage of FEBID Hall sensors for use in single-bead detection setups. However, the FEBID process is limited in resolution. This resolution limit is given in first approximation by the beam size and the deposition regime [44], as well as on the the height of the deposit and the SE distribution within the deposit [68]. However, as has been discussed in chapter 4, another limit is present for FEBID in HV environment, where the contribution of hydrocarbon to the deposition was found to be size dependent, thus limiting the size of the deposit for which a certain metallic composition can be attained.

6.4 In-situ single-bead detection

6.4.1 Detection scheme

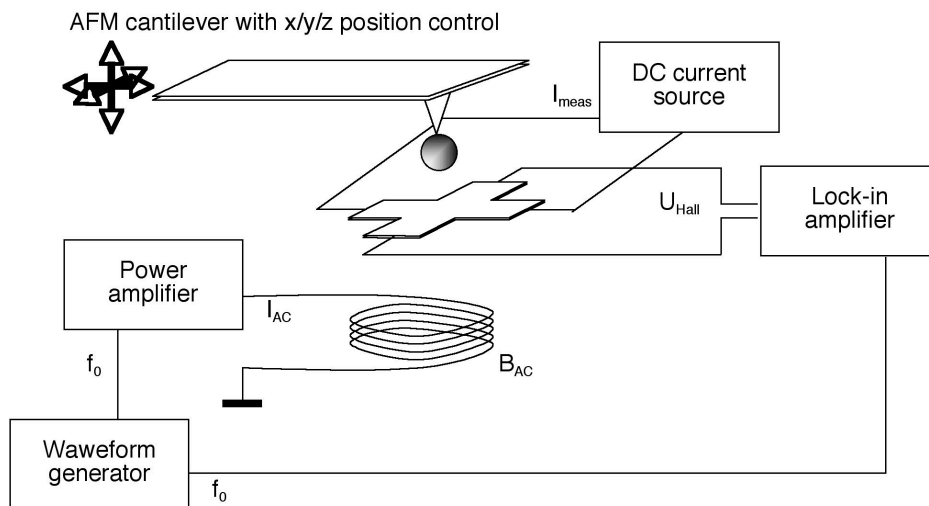


Figure 6.7: Schematics of the bead detection setup used for *in-situ* measurements.

Measuring the magnetic field of a static bead as was shown in section 6.3 is different in some regard to the situation where the field of a moving bead has to be tracked. In [160] and [123], micromagnetic sensors were included into a fluidic setup, where bead handling was realized using close-by current lines exerting an attractive force on the bead when subjected to a current [13]. Alternating the attraction between two current lines situated on both sides

Ref.	Bead	Sensor	w μm	l μm	z_{offset} μm	B_{acc} mT	f_0 Hz	S_I Ω/T	I_{meas} mA	U_{bead} μV	B^{sens} T	C_{exp}	C^{theor}
[157]	D28	GMR	20	5	1	5.0	200		5				8.0×10^{-3}
[105]	D28	Hall	2.4	2.4	5.6	1.1	520	175	0.3	0.3	5.0×10^{-6}	9.1×10^{-3}	5.0×10^{-3}
[116]	M20	SV	2	6	0.3	1.5	DC	462	10	100	2.2×10^{-5}	4.8×10^{-2}	4.5×10^{-2}
[117]	D28	SV	3	4.1	0	3.2	40			12			1.3×10^{-1}
[110]	D28	Hall	4.5	4.5	0	4.4	670	370	1		3.3×10^{-6}	2.2×10^{-3}	7.5×10^{-2}
[87]	M20	PHE	10	10	0.2	1.5	DC	30	10	0.3	1.0×10^{-6}	2.2×10^{-3}	3.5×10^{-3}
[153]	S12	Hall	1	1	0.025	2.1	622	616	0.04	2	8.1×10^{-5}	$4.7 \times 10^{-2[1]}$	2.4×10^{-1}
	D28	Hall	0.6	0.6	0.25	7.6	172	0.091	10	1.9	2.1×10^{-3}	5.5×10^{-1}	3.8×10^{-1}
[160]	D28	SV	1.4	6	1.5	1.0	DC	6500	3	150	7.7×10^{-6}	1.5×10^{-2}	3.7×10^{-2}
[123]	M10	GMR	3	100	0.5	1.3	200k	2150	4	0.3	3.5×10^{-8}	1.9×10^{-5}	$2.6 \times 10^{-4[2]}$
[123]	D28	GMR	3	100	0.5	1.3	200k	2150	4	1.4	1.6×10^{-7}	2.5×10^{-4}	$3.1 \times 10^{-3[2]}$
[161]	D28	GMR	3	100	0.5	2.0	100k	2150	1	0.5	2.3×10^{-7}	2.3×10^{-4}	$3.1 \times 10^{-3[3]}$
	D28	Hall	0.5	0.5	0.6	11.9	172	0.036	15	0.8	1.5×10^{-3}	2.5×10^{-1}	2.2×10^{-1}

Table 6.3: Overview of static (upper half) and moving (lower half) single-bead detection experiments reported in literature. Shaded lines highlight our results for comparison. “D28” denotes Dynabead D-280, diameter $2.8\mu\text{m}$, “M20” Micromer-M, diameter $2.0\mu\text{m}$, “S12” is the Sigma Bead, diameter $1.0\mu\text{m}$, and “M10” stands for Dynal MyOne, diameter $1.0\mu\text{m}$. The bead characteristics are given in table 2.1. The sensor principles are Giant Magnetoresistance (GMR), Spin-Valve (SV), Planar Hall effect (PHE) and Hall sensors (Hall) (see section 2.2.5). w and l denote the sensor’s width and length, respectively. The experimental coupling factor C_{exp} was calculated using equation (6.5) and the magnetic susceptibilities listed in table 2.1. The theoretical value of the coupling factor C^{theor} is given by equation (6.6). For the moving bead experiments, where the coupling factor is dependent on the bead-sensor distance, the factor was calculated for the closest geometry experimentally achievable. ^[1] The experimental coupling coefficient differs by an order of magnitude because the bead was not saturated in the experiment. ^[2] A fluidic platform was used for bead handling. The effective bead-sensor distance is underestimated by about $1.5\mu\text{m}$, hence, the coupling coefficient C^{theor} is overestimated. ^[3] An AFM tip was used for manipulation where the bead is attached to the side of the tip. This offset is not included in the tabular z_{offset} ; for this reason, the coupling coefficient C^{theor} is overestimated.

of the micromagnetic sensor, the beads were controllably brought to cross the sensor, while the sensor response was monitored. A clear, symmetric peak appears as the bead crosses the sensor, which is adequately described by a magnetic dipole moment (equation (2.18)). The authors concluded that the micromagnetic sensors could be used in a microfluidic setup to count beads crossing the sensor. However, the height at which the bead crosses the sensor is not defined, being in the range of micrometers due to electrostatic forces [160].

Here, another approach to vary the position of the bead with respect to the sensor was used. It is comparable to the setup used in [161], where a bead was attached to the side of an AFM tip, which was used as a micromanipulator to vary the bead's position. In this section, we report in-situ bead detection performed inside the chamber of an SEM. This offers the clear advantage that the bead position can be tracked by using the imaging capabilities of the electron microscope, obviating the need of having the AFM tip free of the bead to use it for imaging purposes as in [161]. Hence, we were able to place the bead on the very tip of the AFM nanomanipulator and to monitor the sensor's response including the position where the bead is in closest vicinity to the sensor.

The Hall sensor output is recorded in the presence of an oscillating magnetic field B_{ac} , which is enhanced locally as the microbead is approached towards the sensor using a nanomanipulation setup, because the magnetized bead creates a supplementary contribution to the local magnetic field as it approaches the sensor. The detection scheme is shown schematically in figure 6.7.

6.4.2 Results and discussion

The result of the in-situ detection experiment is shown in figure 6.8. Upon movement of the bead away from the sensor, the Hall signal changes to a lower value, depending on the distance between the sensor surface and the bead. It is important to note that the AFM tip used as a micromanipulator does not contribute to the variation in Hall signal. This was verified by recording the output of the sensor while the AFM tip (with no bead attached) was moved towards the sensor (see figure 6.8, dotted line). Also, the inductive signal U_{ind} was not found to change with the AFM position.

The sensor signal was recorded at varying distances and the result is shown in figure 6.9. It is readily seen that at bead distances greater than $1.8\mu\text{m}$, no change in signal is monitored. This corresponds to the maximum distance up to which the bead can be detected in this configuration. The useful signal range, defined as the difference in signal between the close and

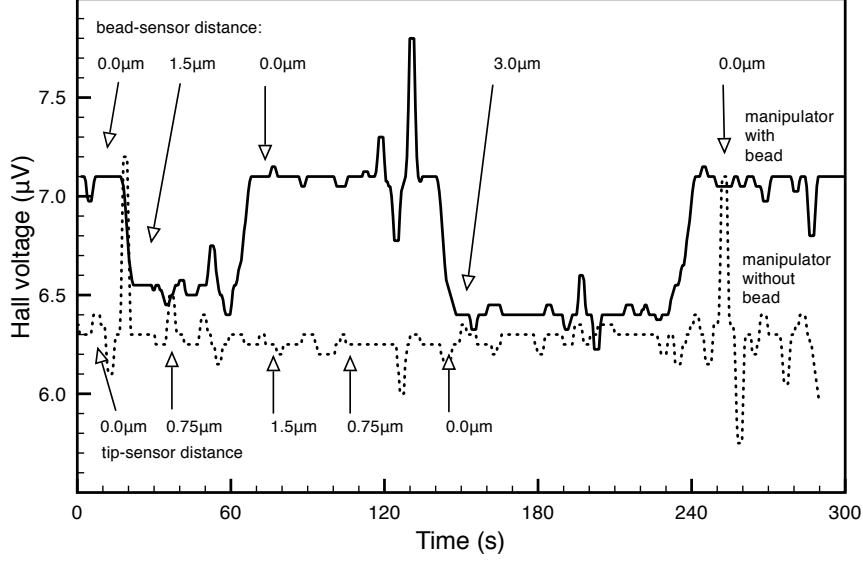


Figure 6.8: Hall signal versus time during movement of the micro-manipulation setup. Full line shows response to the change of a microbead's position. Dotted line shows corresponding response to the bare AFM tip used as a nanomanipulator.

the distant bead position, is roughly 700nV, which compares with an induced voltage of $720\mu\text{V}$ (see table 6.1). Accordingly, the noise level is quite important as compared to the signal. The jumps in the signal in figure 6.8 correspond to the last digit of the Lock-in scale because the scale was limited by the presence of the inductive voltage U_{ind} .

In figure 6.9, the model values expected from the dipole model are shown as an overlay. The model introduced in section 6.3 remain valid (see equation (6.5) introducing the bead signal U_{bead}), but now the coupling coefficient C (equation (6.6)) is a function of the bead-sensor distance z . For sensor sizes much smaller than the bead diameter, equation (6.7) rewrites to:

$$U_{bead} \approx S_I \cdot I_{meas} \cdot \frac{\mu_0 \Delta m}{4\pi(R + z_{offset} + z)^3} \quad (6.9)$$

The in-situ detection does not use a DC magnetic field B_{dc} . The model distance between the dipole and the sensor comprises the bead radius R , an offset (related to the thickness of the sensor) z_{offset} and the actual bead-sensor distance z . The fit of the data shown in figure 6.9 using equations

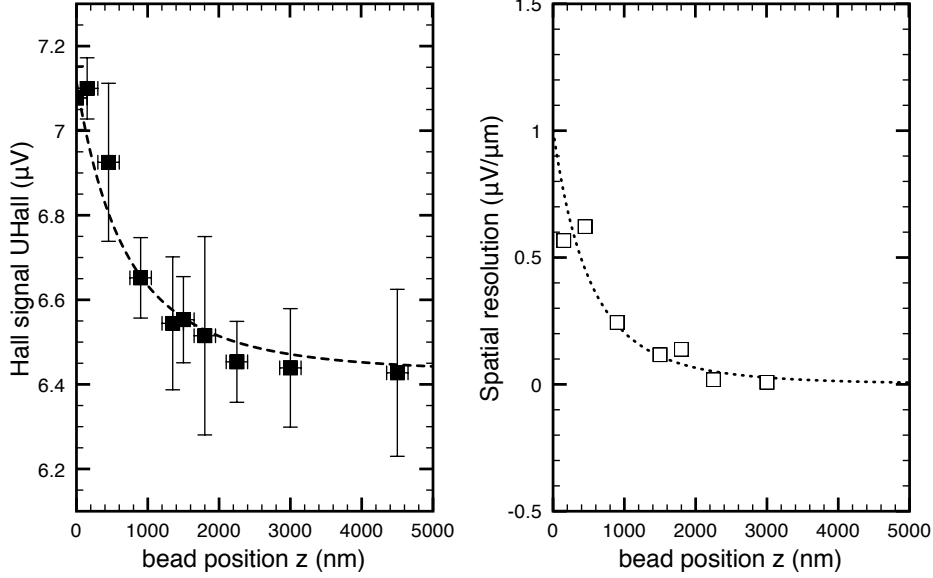


Figure 6.9: *In-situ bead tracking. a) Hall signal versus bead distance from sensor and b) corresponding spatial resolution (right-axis).*

(6.9) and (6.8) yields a Langevin coefficient α of 95 (see equation (2.16)); corresponding to a magnetic susceptibility of the bead of $\chi=0.6$) and an equivalent offset z_{offset} of 660nm. As was the case for the in-situ detection, this offset is found to be close to the portion of the FEB induced deposit higher than the gold electrodes, which was measured by AFM to 600nm.

The highest response is obtained for the situation where the bead is in contact with the sensor. This is a difference to the setup described in [161], where the authors used a GMR micromagnetic sensor. As this sensor is sensitive only to magnetic fields in the planar direction, and as the low saturation of the sensor makes an in-plane magnetization of the bead impossible, the magnetic signal of the bead is zero at the point where the microbead is just above the sensor, i.e. the point where the coupling factor C would allow for the highest position resolution. For this reason, the GMR sensor discussed in [161] could well be used to map the magnetic field of the bead as it crossed the sensor, but does not allow for tracking of the bead's position, e.g. in a molecular switch configuration: for a perfectly centered bead, the sensor signal is zero for any height above the sensor.

Analytically, the spatial sensitivity of the sensor to the vertical movement

of a perfectly centered bead is given by:

$$\frac{dU_{bead}(z)}{dz} = S_I \cdot I_{meas} \cdot \frac{3\mu_0\Delta m}{4\pi(R + z_{offset} + z)^4} \stackrel{z \gg R+z_{offset}}{\propto} \frac{1}{z^4} \quad (6.10)$$

which predicts a rapid drop, proportional to z^{-4} of the sensor signal with the increase of the distance z between the bead and the sensor. Dividing the noise level of the measurement by the spatial sensitivity yields the spatial resolution in units of dimension. Figure 6.9b shows the sharp drop of spatial sensitivity of the in-situ detection as soon as the bead is moved away from the sensor. The sensitivity is about $1\mu\text{V}/\mu\text{m}$ when the bead touches the sensor and drops rapidly to zero as the bead approaches the resolution limit of $1.8\mu\text{m}$. Under our experimental conditions, a noise level of about 100nV (corresponding to the last digit of the Lock-in amplifier scale) was obtained, as the amplification range was limited by the inductive signal U_{ind} . This noise level corresponds to a spatial resolution of about 100nm , when the bead is in contact with the sensor. Reducing the induced voltage, which could be achieved by including on-chip magnetizing wires as described in section 6.3, an increase in spatial resolution is expected.

6.5 Conclusion

In this chapter, we have shown single-bead detection using FEB deposited Co-C micro-Hall sensors. The findings were discussed in terms of the magnetic susceptibility of the microbead and of a coupling coefficient describing the geometrical applicability of a specific microsensor to bead detection. We showed that it is possible to measure the magnetic susceptibility of a Dynabead M-280 using a CoC Hall sensor. Due to the possibility to fabricate magnetic sensors with active areas down to hundreds of nanometers in dimensions, excellent coupling coefficients are demonstrated for FEBID CoC Hall sensors. Finally, a novel bead manipulation setup was shown which allowed measuring the bead's magnetic signal at any position of the bead with respect to the sensor. Using this setup, it was shown that the sensor is capable of tracking the vertical distance between the CoC sensor and a Dynabead M-280.

Chapter 7

Conclusion

This thesis reports the successful fabrication and characterization of sub-micron sized, nanocomposite CoC Hall sensors fabricated by Focused Electron Beam Induced Deposition (FEBID) of $\text{Co}_2(\text{CO})_8$. We demonstrate that these sensors are able to detect single superparamagnetic microbeads such as used in biomolecular assays for molecular tagging. Ideally, one would want to be able to track the position of such microbeads, in order to monitor changes in molecular length under the action of certain restriction enzymes. While optical bead tracking is available, it is not possible to integrate this technique into array-like, high throughput assays. In order to integrate quantitative, parallel read-out of biomolecular reactions in Lab-on-a-chip platforms, there is a need for integrated, high sensitivity magnetic sensors which are able of single microbead detection. This requires high sensitivity materials and the possibility to scale it down below bead dimension. While micromagnetic sensors exhibiting high sensitivities are available, the sensors are not easily scaled down, and the fabrication steps involved are not necessarily compatible with the integration in a microfluidic platform. This lack of easy to integrate, high sensitivity, sub-micrometric magnetic sensors motivated this work on using FEBID for the deposition of magnetic sensing elements.

The material deposited by FEBID of $\text{Co}_2(\text{CO})_8$ consists of Co nanocrystals in a carbonaceous matrix. In this material, high sensitivities to the magnetic field are obtained, as electronic transport is subject to the Extraordinary Hall effect, due to the ferromagnetic nature of the Co nanocrystals, which is enhanced by intergrain scattering due to the nanocomposite structure of the material. Add to this the ability of FEBID to carry out deposition in any geometry on surfaces, including at the bottom of prestructured microfluidic channels, and FEBID appears to be a strong candidate for the realization of sub-micron Hall sensors for single microbead tracking.

This thesis pursued this concept by focusing on the steps involved in

the realization of such a nanocomposite CoC Hall sensor. First, we focused on the processes which arise on the single-molecular scale under electron-irradiation with the investigation of fundamental dissociation pathways induced by electrons. On the electron-beam scale, an exact understanding of the FEBID induced deposition process in a High Vacuum chamber, taking into account the role of chamber background hydrocarbons, was developed. On the material scale, the magnetic sensing properties of the deposited material were investigated in-depth. Finally, on the application scale, single-bead detection and tracking was demonstrated.

In the following, we summarize the main results obtained during this study. Future research perspective are given in section 7.2.

7.1 Contributions of this thesis

FEBID is known to yield materials with varying purities. For FEBID of $\text{Co}_2(\text{CO})_8$, compositional variations between 20at.% and 97at.% are found in the literature. For the first time, we demonstrate experimentally the controlled tunability of the process between 30at.% and 70at.% using the electron-beam pulse-time as the tuning parameter. These findings are explained in terms of co-deposition taking the chamber background hydrocarbons in the High Vacuum chamber into account, thus demonstrating their importance in the FEBID process and invalidating the negligibility of this parameter in the discussion of FEBID in HV chambers. A general, two-adsorbate model describing the evolution of the surface adsorbate densities of the species participating in the deposition is presented. An analytical solution is derived for the case where surface-diffusion is implicit. Using this analytical solution, general expressions for the tunability of a two-adsorbate deposition process are given. It is found that for two species to open a broad tunability window, the ratio of the product of the mean surface residence times τ and electron-impact dissociation cross sections σ must be far from unity. We show experimental evidence for this two-adsorbate model in a system consisting of $\text{Co}_2(\text{CO})_8$ and chamber background hydrocarbons. The model allows for a *quantitative* description of the variation of the composition of the deposited material. We believe this model to be of high importance to the FEBID community, as it allows to controllably tune the composition and hence the physical properties of composite nanosized elements obtained by FEBID in the presence of two adsorbed species.

We have then studied the nanocomposite CoC material obtained by FEBID of $\text{Co}_2(\text{CO})_8$ with regards to its magnetic sensing properties. A Langevin fit was applied to the measured Hall voltage signal. We demonstrate that this

procedure allows to magnetically estimate the average nanocrystal size in the CoC nanocomposite, providing a microcharacterisation method of the material. We experimentally show the dependence of the saturation magnetic field of the material on the composition and explain the findings by smaller nanoparticle sizes for nanocomposites with higher Co contents. A linear dependency between the electrical resistivity and the Hall resistivity at saturation is found, hence proving the importance of intergrain scattering for the increase in field sensitivity in the CoC material. Empirically, we then show how inverse trends on sensitivity and resistivity in the CoC material lead to an optimum in terms of minimal field resolution at a composition of about 65at.%. To the best of our knowledge, the proposed CoC nanocomposite Hall sensors are the most sensitive integrated microsensor in terms of ultimate magnetic flux resolution.

Finally, we have demonstrated the ability of the CoC nanocomposite Hall sensor to detect a single superparamagnetic Dynabead M-280. Due to the possibility to obtain active areas in the order of hundreds of nanometers in width using Focused Particle Beam Processing, the CoC Hall sensors have excellent coupling to the highly localized magnetic field of a single superparamagnetic microbead. The CoC Hall sensor is not only suitable to conduct simple bead detection experiments, but allows to measure the magnetic susceptibility of a single microbead. A novel nanomanipulation setup is presented which allows the in-situ measure of the magnetic field of a single microbead in a SEM where a magnetic field source has been integrated. This novel nanomanipulation setup is used to demonstrate bead tracking by the CoC nanocomposite Hall sensor mimicking the enzymatic curl-up of a biomolecule.

7.2 Future research perspectives

We believe several interesting two-adsorbate systems can be identified for future study work, maybe also allowing to understand previous compositional results in a new light. With the development of dual-GIS systems, two species can be co-adsorbed on surfaces while controlling the respective molecular fluxes. Using carefully chosen compounds, high tunability could be implemented for Co/Pt, Co/Cu, Ni/Fe and other magnetically relevant materials. We hope that the understanding of two-adsorbate deposition proposed in this thesis will lead to applications in novel composite nanomaterials. Also, the proposed co-deposition mechanism opens the door for materials exhibiting a compositional gradient on the nanoscale for which applications remain to be found.

The next steps in the integration of CoC Hall sensors are straightforward. The integration of on-chip magnetic modulation coils will reduce the inductive signal currently limiting the experimental resolution of the setup. Having demonstrated the feasibility of high-sensitivity, sub-micron CoC nanocomposite Hall sensors for single microbead tracking, we believe that with the future break-through of parallel e-beams for high-throughput FEBID, the integration of CoC nanocomposite Hall sensors in high-density chemical arrays using microbead tracking as transducer will hopefully become a beneficial technique allowing ultra-low molecular detection for use in high-sensitivity diagnosis platforms or feedback sensors in novel nanoactuator devices.

Appendix A

Thermal decomposition of $\text{Co}_2(\text{CO})_8$ by electron-beam induced heating

FEBID of Cobalt containing material has been shown to yield deposits with a very broad range of compositions, from 10at.% up to over 95at.% [19, 37, 38, 62] (see figure A.1), with primary electron energies between 5keV and 30keV and with beam currents varied between 20pA and $2\mu\text{A}$. Thermal decomposition by electron-beam induced heating was shown to yield deposits of high purity ($\geq 85\text{at.}\%$) [18]. In all cases, increase of the beam current was shown to lead to higher purities in the deposits and this effect was generally attributed to local heating by the electron-beam, leading to thermal annealing of the CoC deposit [18, 19, 37, 62]. In this chapter, we show the conditions under which thermal decomposition plays a role for deposition of $\text{Co}_2(\text{CO})_8$, comparing experimental results with Monte-Carlo simulations of electron-beam induced heating.

A.1 Introduction

$\text{Co}_2(\text{CO})_8$ is known to decompose at temperatures slightly above its melting point of 51°C [56]. However, the thermally deposited material incorporates non-negligible amounts of carbon and oxygen (15-30at.% at 100°C , [51]) due to the incomplete decomposition of the precursor molecule [52]. Above 200°C , thermal decomposition of the precursor molecule is complete [51, 52]. Thermal decomposition of $\text{Co}_2(\text{CO})_8$ has also been shown to occur during FEBID, when working with beam currents high enough to create non-negligible temperature rise [18]. When depositing linear or planar cobalt-containing films,

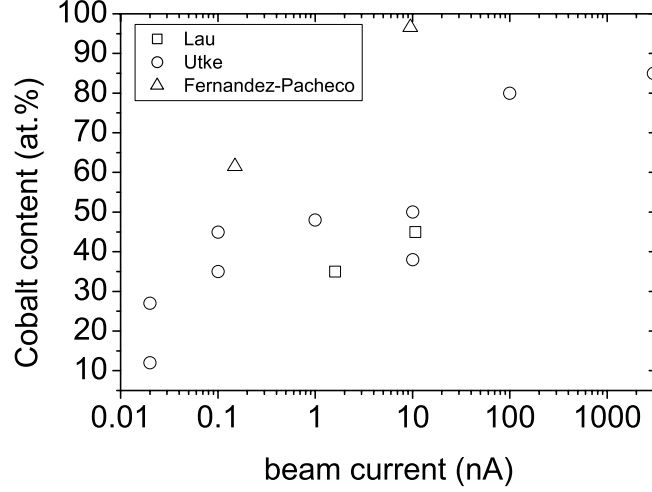


Figure A.1: Cobalt contents of FEBID deposits reported in literature. Sources: [18, 37, 62].

such temperatures can be reached when depositing on substrates with low thermal conduction, such as silicon nitride free-standing membranes, where heat dissipation is only two-dimensional.

A.2 Experimental results

We show thermal decomposition of cobalt carbonyl in FEBID by scanning a beam over a 150nm-thick silicon nitride membrane repeatedly. Due to electron-beam heating and low thermal conduction, heat is built up in the membrane, leading to a deposit being magnitudes larger than the beam diameter (see figure A.3). Two different deposition regimes can indeed be identified: incomplete decomposition in the outer, lower-temperature parts, and complete decomposition in the inner, higher-temperature part.

A.3 Heat transfer model

Using Monte Carlo simulation of the energy density distribution per electron [48], the energy loss per electron for different acceleration voltages can be calculated (table 4). The energy loss is assumed to be transferred to thermal energy and thus is used to calculate the heating power of the electron beam.

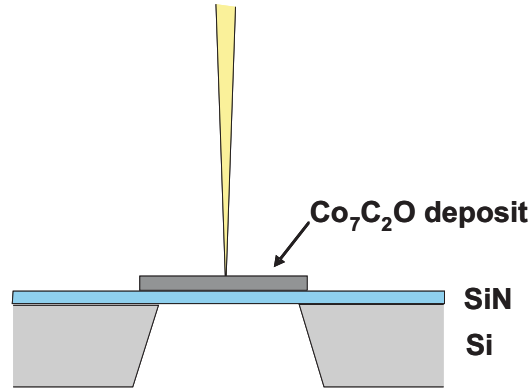


Figure A.2: *Schema of deposition experiment.*

Material	κ	ρ	$\int \Phi$ 5keV	$\int \Phi$ 25keV
SiN _x (x=0.8-1.0)	3W/mK [162]	3.4g/cm ³	3.4keV	0.6keV
Co	100W/mK	8.9g/cm ³	3.7keV	2.3keV
Co _{0.73} C _{0.18} O _{0.09}	20W/mK [18]	7.2g/cm ³ [39]	3.7keV	1.7keV

Table A.1: *Parameters used for the MC simulation of energy loss per electron and FEM simulation of electron-beam heating. κ is the thermal conductivity and ρ is the density. The energy loss per electron $\int \Phi$ is calculated through a 150nm membrane of the corresponding material.*

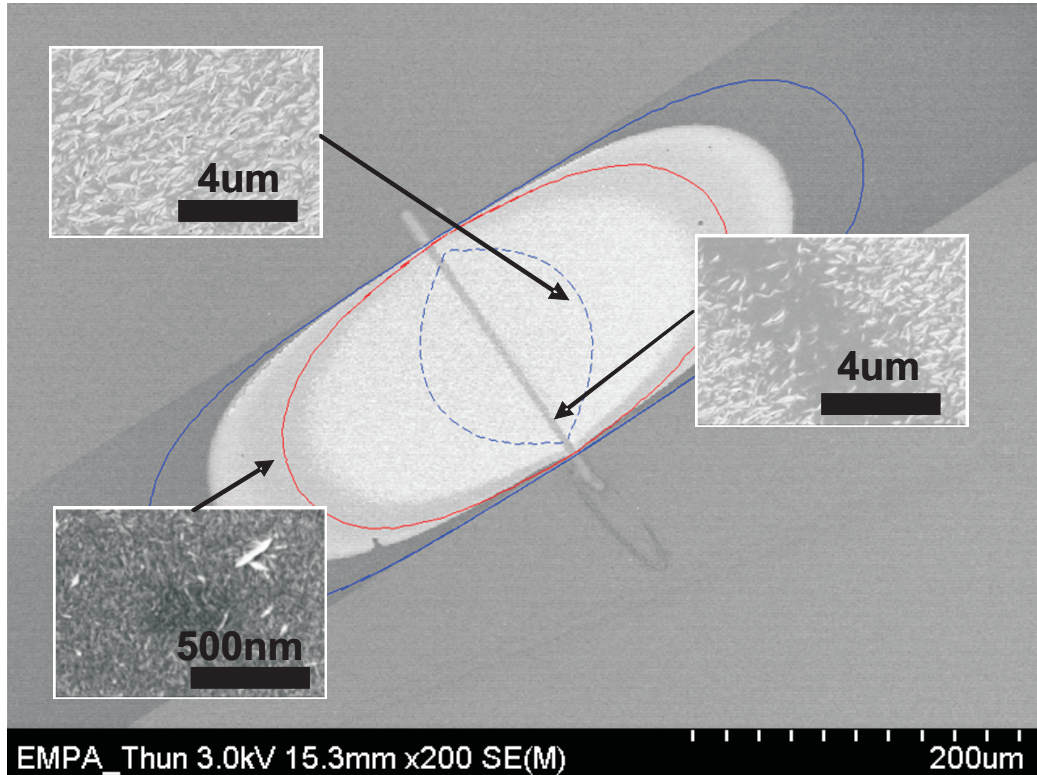


Figure A.3: SEM image of the FEB line deposit of $\text{Co}_2(\text{CO})_8$ on a 150nm Silicon nitride membrane. The beam (25kV, 250nA) was scanned repeatedly over the line segment, leading to a local heating of the silicon-nitride membrane and large-area thermal deposition. Isotherm simulation data is superposed. Dotted lines show the limit of 50° C under initial irradiation before any deposit appears. Full lines show the limits of 50° C and 200° C heating in the presence of an 150nm thick CoC deposit. (a) High-purity dissociation to polycrystalline cobalt (86at.%, as measured by EDX) is observed in the region close to the heat source. (b) incomplete dissociation (80at.%) on lower temperatures regions of the membrane. (c) The part of the deposit irradiated by the electron-beam during deposition appears darker and amorphous; Cobalt content of the irradiated part is measured as 88at.% Co by EDX.

We use a finite-element method (FEM) software to then calculate the heat distribution in the membrane. The heating power is calculated using:

$$P = \int_0^{-t} \Phi(z) dz \cdot I \quad (\text{A.1})$$

where t denotes the membrane thickness, $\Phi(z)$ is the ionization depth distribution projected on the incident electron beam axis and I is the incident beam current. For the given primary electron energy (25keV), beam current (250nA) and membrane thickness (150nm), the initial heating power is estimated to 98 μ W. Assuming fast scanning of the beam (i.e. neglecting transient effects), the heating of the membrane can be estimated by FEM modelling. This initial heating is reported in figure A.3 as an overlay (dotted line), showing the limit of 50°C heating before decomposition of the precursor molecule. Thus, thermal induced decomposition is taking place from the very beginning of the dissociation. Upon growth of the deposit, the heating term is increased, due both to the thickening of the membrane, and to the nature of the cobalt-rich deposit, enhancing scattering of the electrons. The upper limit can be estimated by the total power of the electron beam, subtracting the power of the backscattered electrons leaving the system. This upper limit is reported in figure A.3 as an overlay (full lines), showing the limits of 50°C and 200°C heating.

When irradiating a line segment with an electron-beam, the segment under exposure is heated locally and heat transfer takes place, following:

$$\frac{dQ}{dt} = -\kappa A \frac{dT}{dx} \quad (\text{A.2})$$

where Q is the heat energy in Joule, κ is the thermal conductivity in $Jm^{-1}K^{-1}$, and A is the surface through which conduction takes place in m^2 . Integration along x yields:

$$\frac{dQ}{dt} = -\frac{\kappa}{x} A \Delta T \quad (\text{A.3})$$

We express the heat energy in term of the heat capacity C using:

$$\frac{dQ}{dt} = C \frac{dT}{dt} \quad (\text{A.4})$$

Integration along t gives:

$$T(t) = T_0 + \Delta T \exp[-t/\tau] \quad (\text{A.5})$$

where the time constant τ is defined as:

$$\tau = CL/\kappa A \quad (\text{A.6})$$

For the initial membrane (no deposit), assuming uniform heating of the membrane at the irradiated spot (flat top beam, centre of membrane), thermal conduction through a rectangular strip to the heat sink (lower estimate, heat transfer actually faster), and taking as value for the heat capacity of SiN $400\text{Jkg}^{-1}\text{K}^{-1}$ [163], the relaxation time is about $30\mu\text{s}$. This compares to an actual refresh time of $150\mu\text{s}$. Hence, the approach consisting in neglecting transient thermal effects leads to an over-estimation of the actual electron-beam induced heating. As the deposit grows, the assumption becomes worse, as the cross-section area and the thermal conductivity increase.

A.4 Conclusion

Thermal decomposition upon electron-beam heating of a substrate yields two distinct deposit structures. Monte-carlo simulations of ionization density distributions are shown to be a suitable mean for the coarse estimation of the local heating upon linear beam irradiation.

Appendix B

HREELS study of electron-induced dissociation of Tetrakstrifluorophosphine platinum ($\text{Pt}(\text{PF}_3)_4$)

Understanding the fundamental electron-induced reactions leading to the decomposition of the surface-adsorbed precursor molecules is the key to the in-depth understanding of the FEBID processes. For this reason, a four weeks research stay at the Institute of Applied and Physical Chemistry at the University of Bremen was carried out in the framework of COST Action CM0601. In the laboratory of Prof. Swiderek, a high-resolution electron energy-loss spectroscopy (HREELS) apparatus was used to study the dissociation under low-energy electrons of two model precursors in condensed monolayers which is being used in FEBID. This chapter discusses the results found in the case of Tetrakstrifluorophosphine platinum ($\text{Pt}(\text{PF}_3)_4$), a popular FEBID precursor for the deposition of high-conductivity electrical contacts. The preliminary results for the Cobalt containing precursor Cobalt-tri(carbonyl)-nitrosyl ($\text{Co}(\text{CO})_3\text{NO}$) are given in annex C

B.1 Introduction

Electron energy loss spectroscopy is a powerful and versatile spectroscopy technology. Low-energy electrons are emitted from an electron source and are filtered by a monochromator, which transmits only electrons defined by a narrow distribution around a selected energy. This monochromatic electron beam is then impinging on a surface, where it undergoes multiple interactions

with the surface molecules. Elastic interactions give rise to a reflected electron beam with an energy distribution similar to the incident beam. Inelastic interactions however induce energy losses which are highly characteristic for the inelastic excitation channels of the surface molecules. The reflected electrons are collected by a spectrum analyzer where their energy loss is measured. This allows characterisation of the surface molecules regarding chemical composition and the nature of covalent bonds.

In this chapter, we take advantage of this technique to investigate the dissociation process of precursors relevant for FEBID at low electron energies, comparable to the energy of secondary electrons or low energy back-scattered electrons generated by high energy primary electrons in FEBID. Precursor molecules are adsorbed on a clean surface and exposed to electrons with defined energy. HREEL spectra are collected and dissociation energies are identified.

B.2 Tetrakistrifluorophosphine platinum

$\text{Pt}(\text{PF}_3)_4$ (CAS 19529-53-4) is a pure trifluorophosphine complex [15] which has been shown suitable for the electron-beam induced deposition of Pt [31, 164, 165], with reported deposit composition of up to 82 at.% Pt, 13 at.% P and 4 at.% F (at 10kV, 41nA irradiation). The reported vapour pressure is 53 mbar at room temperature [166]. $\text{Pt}(\text{PF}_3)_4$ was chosen for this study because it is a widely used precursor in FEBID for the deposition of electrically conducting electrodes [31, 164].

$\text{Pt}(\text{PF}_3)_4$ has a reported melting point of -15°C and a boiling point of 86°C (at atmospheric pressure). Thermal decomposition is reported to take place at 90°C . Under FEBID conditions, electron-induced fragmentation of adsorbed PF_3 ligands compete with the desorption of intact ligands, which leads to non-negligible amounts of phosphorus being embedded in the deposit [15]. Increasing the substrate temperature thus leads to higher purity deposits, as the desorption rate of the released ligands is increased [164]. The desorption temperature of PF_3 from Ag(111) surfaces is 125K, as measured by temperature-programmed desorption (TPD) [167]. This compares to a reported desorption temperature of 170K for the $\text{Pt}(\text{PF}_3)_4$ molecule adsorbed on a Pt surface [168].

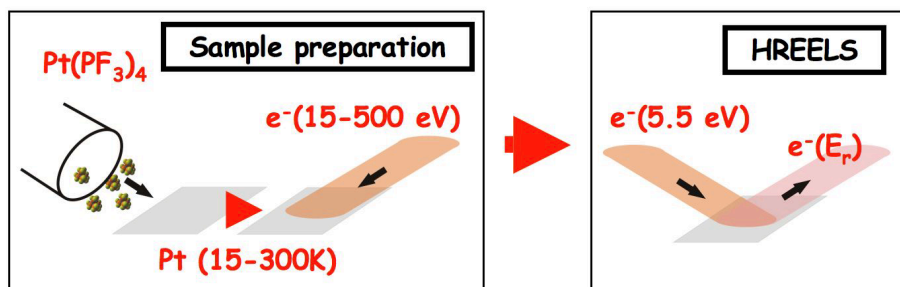


Figure B.1: Schematic representation of the HREELS experiment carried out. In a first step, molecules are adsorbed on a substrate and subjected to electron irradiation. The HREEL spectra are recorded in a second step. Iterating between irradiation and spectrum acquisition yields dose resolved spectra.

B.3 Experimental setup

The HREELS apparatus consists of two chambers: the main chamber and the preparation chamber. Specimens are prepared in the preparation chamber and moved into the main chamber to perform HREELS measurements. Both chambers are separated by a mechanical valve, thus preventing contamination in the main chamber during sample preparation. The experimental flow is schematically represented in figure B.1.

A critical parameter for the resolution of HREELS is the chamber pressure. Using a combination of turbo-molecular and ionic getter pumps, UHV regime is established, translating into 10^{-11} to 10^{-9} mbar in the main chamber. During sample preparation, the pressure in the preparation chamber never exceeds 5×10^{-8} mbar.

The sample consists in a Pt foil mounted on a mobile cryostat. The cryostat can be heated in a temperature range of 15K to 300K using a resistive heating setup. Precursor molecules are leaked into the chamber using a needle valve and get adsorbed on the Pt foil. The amount of adsorbed molecules is estimated by the pressure drop in the reservoir tubing upon opening of the needle valve. An electron flood gun delivering several microamperes of electron in the energy range of 5-500 eV is also mounted in the preparation chamber. A picoammeter connected to the substrate is used to monitor the impinging electron current, in order to perform controlled irradiation of the sample. The dose delivered to the sample during the irradiation step is in the order of $\mu\text{A}/\text{cm}^2$.

In the main chamber, a monochromatic electron source delivers an electron current ($\approx 100\text{-}200\text{pA}/\text{cm}^2$) with defined energy (5eV) onto the sub-

strate. The electron source is a W-filament. The monochromatic distribution is obtained by the serial arrangement of two monochromator units, where the electron beam is deflected by multiple electrostatic fields onto a curved trajectory inside a rounded tube. The exit slit is only reached by electrons having the appropriate energy. Electrostatic lenses allow for focusing and narrowing of the beam.

Opposite the monochromatic electron source, an analyzer collects the electrons reflected from the surface. Again, a curved electrostatic field is used to tune the transmission of the electrons with regard to their energy. At the end of the analyzer, a channeltron is used to amplify the electron signal.

The angle between the electron source and the normal to the substrate can be varied mechanically, whereas the angle between the spectrum analyzer and the substrate normal is fixed at 60° . Specular condition is obtained when the angle of the impinging probing electrons is equal to the angle of the spectrum analyzer, whereas all other positions are off-specular. This is relevant, as some electron-molecule interactions lead to a specific exit angle of the electrons involved, whereas other lead to diffuse electron reflection.

Spectra were acquired in sets of 600 channels in the range of 5.05 to 4.45eV. Each channel is the absolute electron count integrated at 1Hz. Each individual set of measurement is obtained by three subsequent scans, which leads to acquisition times of 30 minutes per set. Data shown in the results section are obtained by averaging two subsequent data sets, which have been corrected for drifts in the position of the elastic peak previously. The resolution of the elastic peaks was typically 11meV full width at half maximum (FWHM) and was in all cases below 13meV FWHM during all experiments.

It is important to note that the absolute intensities of the spectra carry little information, as they are readily influenced by temperature changes or especially by charging phenomena, so that only relative intensities of peaks can be used to infer changes in the composition of the adsorbed layers. Furthermore, we monitored shifts in peak energies, which hint at the appearance of new species.

B.4 HREEL spectra of unirradiated adsorbates

B.4.1 Identification of fundamental modes

The HREEL spectrum of $\text{Pt}(\text{PF}_3)_4$ is shown in figure B.2. Identification of the fundamental peaks is performed by comparison with IR spectroscopy

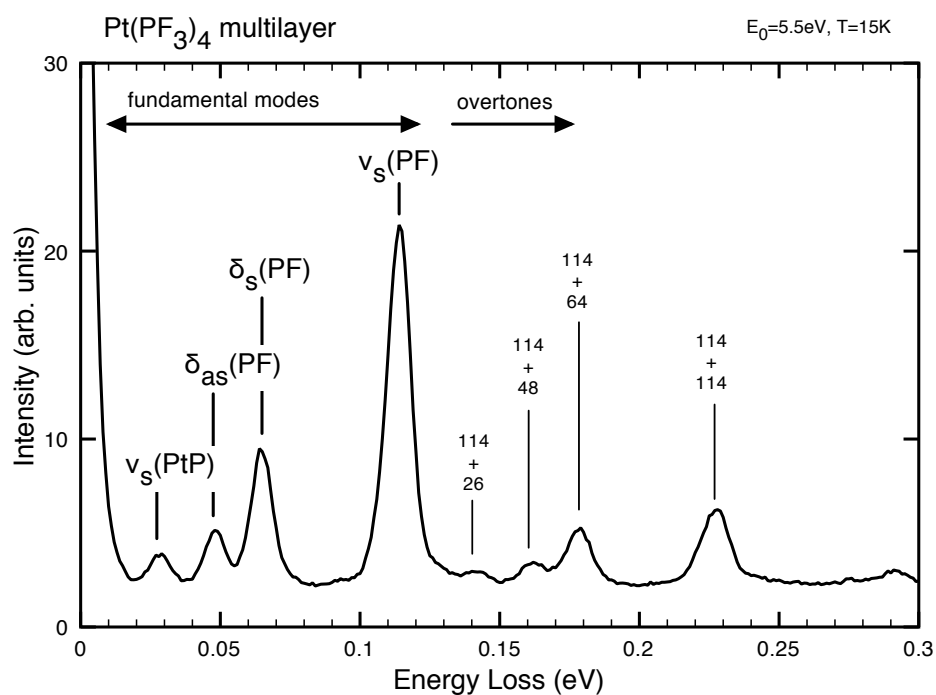


Figure B.2: Fundamental modes of $Pt(PF_3)_4$ and overtones. The fundamental modes are $\nu_s(PtP)$: Pt-P stretching at 26meV; $\delta_{as}(PF)$: asymmetric PF bending (48meV); $\delta_s(PF)$: symmetric PF bending (64meV); $\nu_s(PF)$: symmetric PF stretching (114meV).

results found in literature [169, 170]. Higher-order peaks are obtained when electrons undergo multiple scattering events and are thus located at sums of fundamental peaks. The strongest peak are the response of the PF_3 ligand, which exhibit high signal-to-noise ratio. This points at a relatively high cross-section of inelastic interaction of electrons with these ligands. The feature used to identify the presence of $\text{Pt}(\text{PF}_3)_4$ is the Pt-P stretching peak located at 26meV.

B.4.2 Assessment of substrate coverage

Energy loss spectra were acquired for different coverages and are shown in figure B.3a. The fundamental modes for the Pt-P and P-F bonds are visible for all adsorbed layers. However, for layers adsorbed with 0.5 μbar or higher differential precursor pressure, higher harmonic peaks (above 114meV) appear. Higher energy loss peaks due to multiple scattering exhibit an increased intensity with respect to the fundamental peaks when the surface coverage increases, as multiple scattering events become more probable to occur. Using this interpretation, we estimate that full monolayer coverage is established when between 0.2 μbar and 0.5 μbar of the precursor is leaked into the preparation chamber.

B.4.3 Confirmation of excess PF_3 removal

At room temperature, $\text{Pt}(\text{PF}_3)_4$ partially releases PF_3 ligands which have to be removed by freeze-pump-thaw cycles to remove high vapor pressure PF_3 [164]. Freeze-pump-thaw cycles were carried out prior to the vacuum distillation of the precursor into the final glass tube. The $\text{Pt}(\text{PF}_3)_4$ precursor was always maintained at a temperature of around 0°C by ice-cooling during experiments.

To rule out the presence of high amounts of free PF_3 in the adsorbed film at 15K, we performed several HREELS measurements at different temperatures (see figure B.3b). Upon crossing the desorption temperature of PF_3 (125K), the ratio between the peak intensities corresponding to the P-F stretching and Pt-P stretching decreases slightly from a ratio 12:1 up to 100K to a ratio 9:1 for 140K and more, pointing to at possible desorption of a small amount of co-adsorbed PF_3 . For temperatures close to the desorption temperature of the $\text{Pt}(\text{PF}_3)_4$ molecule (170K) or above, the peaks corresponding to multiple inelastic interactions disappear, which points at the desorption of the multilayer. At 200K, only the signal corresponding to a single layer of $\text{Pt}(\text{PF}_3)_4$ is recorded, as the monolayer is known to have stronger binding to

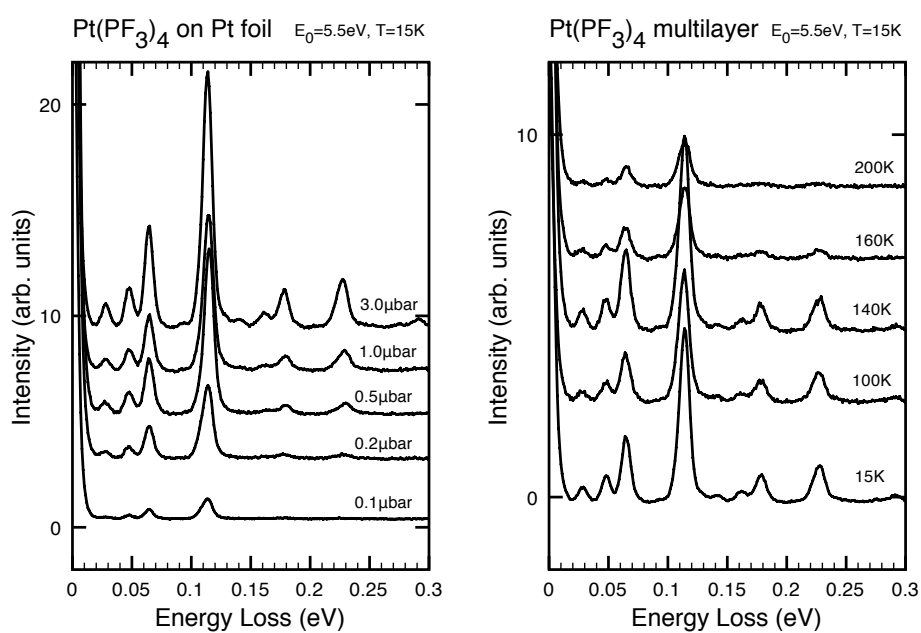


Figure B.3: a) HREEL spectra of $Pt(PF_3)_4$ at different coverages. b) HREEL spectra of $Pt(PF_3)_4$ multilayer acquired at different temperatures. Note that only the relative intensity of the peaks in a spectrum conveys useful information on composition.

the substrate (often comparable to chemisorbed species in binding energy) than the next layers in the multilayer.

B.5 $\text{Pt}(\text{PF}_3)_4$ dissociation under electron irradiation

We investigate the dissociation of $\text{Pt}(\text{PF}_3)_4$ under electron irradiation at varying energies (15eV, 30eV, 100eV, 200eV, 500eV) and varying doses. Doses are calculated by monitoring the substrate current during exposition and measuring the exposure time. Knowing the dimensions of the illuminated area (about 1cm^2), areal doses and current densities can be deduced.

When irradiating adsorbed $\text{Pt}(\text{PF}_3)_4$ at 15K, PF_3 ligands dissociated from the precursor molecule will remain adsorbed on the surface due to the low temperature and might be dissociated upon further irradiation. To distinguish this parallel dissociation channel, irradiation experiments were carried out at temperatures of 140K, i.e. above the reported desorption temperature of PF_3 . Results for 15eV irradiation at 140K are shown in figure B.4a. $\text{Pt}(\text{PF}_3)_4$ was adsorbed at 15K and the substrate heated to 140K. In this heating step, co-adsorbed free PF_3 is desorbed. The substrate temperature is maintained constant at 140K and the film is exposed to varying doses of 15eV electrons. It is found that the HREEL spectra do not exhibit significant change upon electron exposure with energies of 15eV or 30eV in the doses investigated (i.e. $\leq 15\text{mC}$).

The dissociation cross section is bigger at 500eV irradiation of $\text{Pt}(\text{PF}_3)_4$, as can be seen in figure B.4b. Upon irradiation with the lowest measured dose (1200 μC), the Pt-P peak at 26meV vanishes strongly. The peaks attributed to PF_3 are broadened and shifted to lower energies (symmetric stretching peak at 114meV) for the highest investigated dose (4800 μC).

PF_3 is known to undergo dissociation of P-F bonds under electron irradiation as reported for PF_3 adsorbed on Ru(0001) [171] and in the gas phase [172]. In [173], decomposition of PF_3 adsorbed on Ru(0001) under 500eV exposure is reported. The authors describe a step-wise dissociation of PF_3 to PF_2 to PF induced by energetic electrons. In [174], the characteristic energy bands of PF_3 and derived species are calculated and assessed experimentally using PF_3 trapped in solid neon. The authors report a lowered symmetric PF stretching peak ν_s for PF_2 (105meV) compared to PF_3 (110meV). The shift to lower energy losses in our measurements is hence attributed to showing dissociation of the ligands PF_3 to PF_2 . This proves that indeed desorption of PF_3 competes with electron-induced decomposition of this ligand under

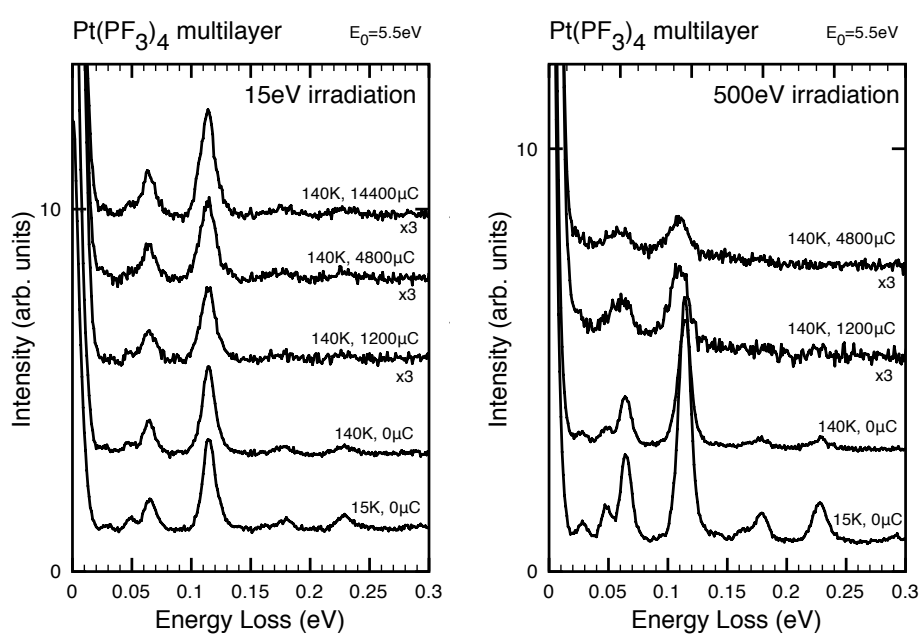


Figure B.4: a) HREEL spectra of $Pt(PF_3)_4$ irradiated with varying doses of 15eV electrons at a substrate temperature of 140K, i.e. above the temperature of PF_3 desorption (125K). b) HREEL spectra of $Pt(PF_3)_4$ irradiated with varying doses of 500eV electrons at a substrate temperature of 140K.

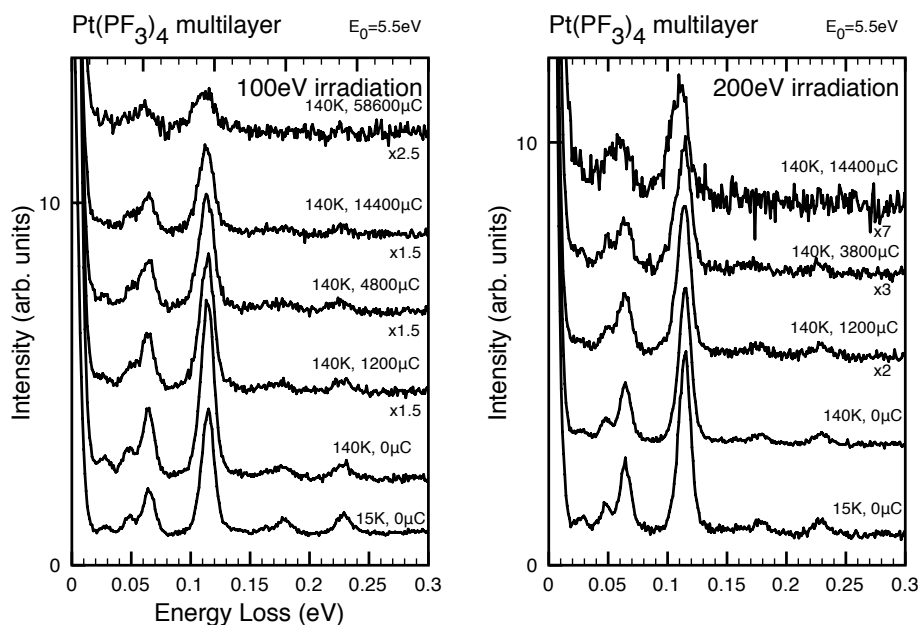


Figure B.5: Irradiation of $\text{Pt}(\text{PF}_3)_4$ with a) 100eV and b) 200eV electrons at 140K showing a shift of the symmetric P-F stretching peak ν_s at 114meV to lower energy losses.

electron irradiation at 500eV. The deposited material must be composed partially by some fragments from dissociated PF_3 ligands. The same behavior was monitored upon irradiation with 100eV and 200eV (see figure B.5) electrons. The intensity of the energy shift however decreases with decreasing electron energy.

B.6 Conclusions

A HREELS study of the low-energy irradiation of $\text{Pt}(\text{PF}_3)_4$ has been conducted. Under higher energy irradiation (100eV upwards), we monitored a shift in peak energy of the PF bond signal to lower energy losses. We tentatively attributed this to the partial creation of PF_2 species due to dissociative irradiation. The energy shift increases with increasing irradiation electron energy, which points to an increase in intra-ligand bond dissociation cross-section with electron energy. Putting these findings together, we expect that lower energy irradiation yield Pt deposits of higher purity.

The experimental limitations we encountered regarding the measurements

of $\text{Pt}(\text{PF}_3)_4$ were surface charging upon electron irradiation and of course, the vicinity between the Pt-P peak and the elastic peak ($\Delta E=26\text{meV}$). Both effects would make it difficult to identify the intensity of the PtP peak after electron irradiation.

Complementary work is in progress at the laboratory at the Surface Chemistry and Interfacial Phenomena Laboratory of Prof. Fairbrother, aiming at the investigation of the dissociation pathways using X-ray photoelectron spectroscopy (XPS).

Appendix C

Preliminary HREELS study of the electron-induced dissociation of Cobalt-tri(carbonyl)-nitrosyl ($\text{Co}(\text{CO})_3\text{NO}$)

In this annex, we present the preliminary HREELS measurements realized on the Cobalt containing precursor Cobalt-tri(carbonyl)-nitrosyl ($\text{Co}(\text{CO})_3\text{NO}$). The HREELS spectrum of the adsorbed compound is presented. Major peaks are identified. Preliminary results under irradiation are shown.

C.1 Cobalt-tri(carbonyl)-nitrosyl $\text{Co}(\text{CO})_3\text{NO}$

$\text{Co}(\text{CO})_3\text{NO}$ (CAS 14096-82-3) is a dark-red liquid with a reported boiling point of 50°C and a vapour pressure of 107 mbar at room temperature [175]. It decomposes thermally to pure cobalt at 350°C [176]. It has been shown suitable for the electron-beam induced deposition of Co in [37], where it was decomposed thermally by e-beam heating. The composition of e-beam heating induced deposits show a composition of about 45 at.% Co with the balance being O and N in equal proportions ¹.

$\text{Co}(\text{CO})_3\text{NO}$ was preferred to $\text{Co}_2(\text{CO})_8$ for this HREELS study because reported spontaneous, auto-catalytic decomposition of the latter triggered

¹as measured by EDX, deposition carried out with beam currents of 1nA to 200nA at 25keV

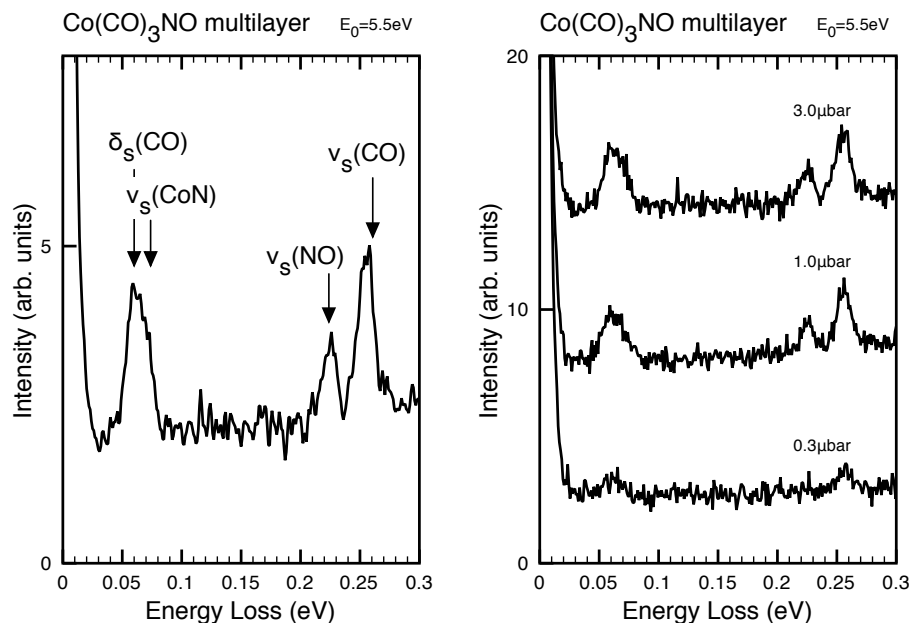


Figure C.1: a) Tentative identification of the fundamental modes of $\text{Co}(\text{CO})_3\text{NO}$: symmetric C-O bending (59meV); Co-N stretching (73meV); N-O stretching (221meV); symmetric C-O stretching (262meV). b) HREEL spectra of $\text{Co}(\text{CO})_3\text{NO}$ at different coverages.

fear of contamination in the chamber and detection optics of the highly sensitive apparatus.

C.2 HREEL spectra of unirradiated adsorbates

The fundamental modes of $\text{Co}(\text{CO})_3\text{NO}$ are reported in figure C.1a. The presence of lighter elements in the ligands reduces the interaction with impinging electrons, which leads to lower signal-to-noise ratio when compared with the spectrum in figure B.2 for $\text{Pt}(\text{PF}_3)_4$. The prominent peaks at 260meV, 220meV and 60-75meV are tentatively identified using comparison with peaks reported for $\text{Co}(\text{CO})_3\text{NO}$ in the gas phase [177] and adsorbed on Na:Zeolith Y [178].

HREEL spectra for different coverages of $\text{Co}(\text{CO})_3\text{NO}$ are shown in figure C.1b. At the lowest measured coverage, corresponding to a precursor flux characterized by a pressure drop of 0.3 μbar at the precursor reservoir tub-

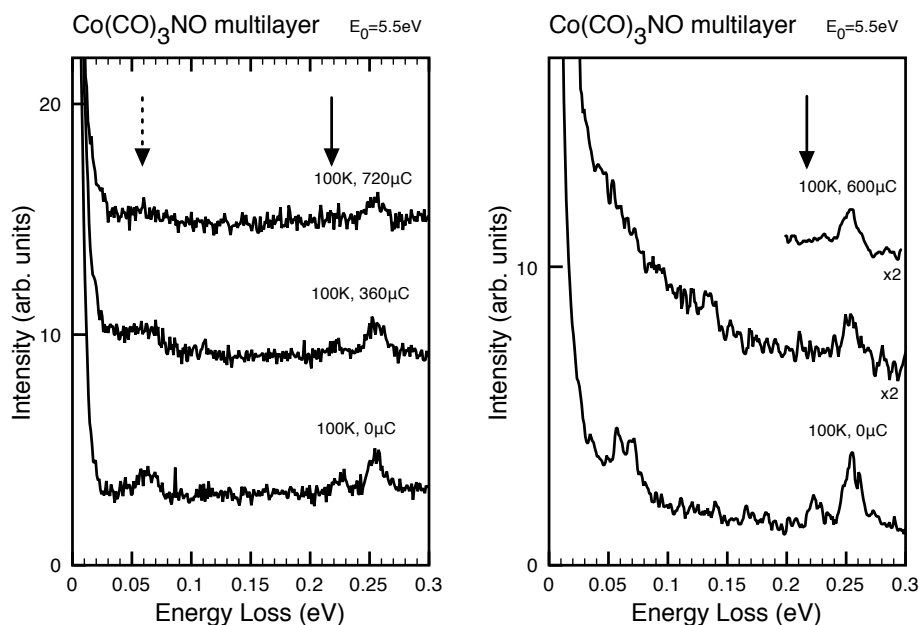


Figure C.2: a) Evolution of HREEL spectra of $\text{Co}(\text{CO})_3\text{NO}$ adsorbed on Pt under increasing 15eV electron irradiation. The arrows indicate the positions of the monitored N-O (full arrow) and Co-N (dotted arrow) peak. b) Evolution of HREEL spectra of $\text{Co}(\text{CO})_3\text{NO}$ adsorbed on Pt before and after 500eV electron irradiation, dose=600μC. Data is smoothed with a 3-pixel floating average filter. The arrow indicate the position of the monitored N-O (full arrow) peak. The 200-300meV range of the exposed spectrum is shown also with an integration time of 36s per meV (main figure: 6s per meV).

ing, the peaks corresponding to C-O stretching and bending are discernable. Upon admission of 1μbar of the precursor, the main fundamental peaks are identifiable. Adsorption of 3μbar of the precursor does not induce a change in the recorded spectrum as compared to a dose of 1μbar, which indicates that the average layer thickness is larger than the penetration depth of the impinging monochromatic electrons used for recording the spectrum. Using this interpretation, monolayer coverage is obtained at a flux between 0.3μbar and 1μbar.

C.3 $\text{Co}(\text{CO})_3\text{NO}$ dissociation under electron irradiation

$\text{Co}(\text{CO})_3\text{NO}$ was adsorbed on a clean Pt surface and exposed to increasing doses of electron with 15eV energies (see figure C.2a). Evolution of dissociation processes is discussed in terms of relative intensities of the 262meV peak corresponding to the symmetric C-O stretch, the 221meV peak corresponding to the symmetric N-O stretch and the 73meV peak corresponding to the Co-N stretch. Due to the low interaction with the monochromatic electrons used for measurement, the signal-to-noise ratio is below good statistics, even though longer acquisition times were used (up to 90 minutes per spectrum). However, first insights in the dissociation of $\text{Co}(\text{CO})_3\text{NO}$ could be obtained.

Upon increase of the total dose, the relative intensity of the peak corresponding to the N-O vibration is found to diminish (figure C.2a, full arrow). In parallel, a decrease of the Co-N peak can be observed (figure C.2a, dotted arrow). However, multiple other excitation modes are found in this low-energy region, so that the decrease is in no way characteristic. Similar results are found for irradiation by 500eV electrons (see figure C.2b). The absence of a discernable NO peak is confirmed by the close-up on the 200meV to 300meV shown as inset in figure C.2b, where the signal integration time was set to 36s per meV (from 6s per meV standard value). The decrease and disappearance of the NO peak tend to point at a dissociation mechanism where the NO ligands would first be released by the precursor molecule at these irradiation energies.

These results are quite surprising. NO ligands are bound more strongly to the metallic entities than CO ligands [179]. As a consequence, the electron irradiation of cationic $\text{Co}(\text{CO})_3\text{NO}^+$ in the gas phase was found to privilege CO ligand liberation [180]. Furthermore, the monitored NO ligand dissociation from the precursor molecule does not account for the high N concentrations found in deposits carried out under FEBID conditions.

In conclusion, we tentatively performed initial HREELS measurements of electron-induced dissociation of $\text{Co}(\text{CO})_3\text{NO}$ with energies of 15eV and 500eV. Due to low signal-to-noise ratios, definite conclusions are hard to draw. We monitored a decrease in NO signal upon irradiation at both energies, which would possibly point at a preferential NO ligand removal. A more in-depth study would be needed to validate this observation, including a preliminary Temperature Programmed Desorption (TPD) study to identify the desorption temperature of the ligands from the substrate,

C.4 Conclusions

Preliminary measurements were undertaken on the electron-induced dissociation of surface-adsorbed $\text{Co}(\text{CO})_3\text{NO}$ precursor molecules. It was expected to see a rapid decrease in CO signal under electron irradiation, as these ligands are believed to be bound more weakly than the NO ligand. However, the NO peak rapidly vanishes under electron irradiation, which seems to point to a liberation of the NO ligand under irradiation with the energies investigated (15eV and 500eV). Here, it would be interesting whether this holds true for other irradiation energies, as for deposition carried out under FEBID conditions (i.e. with electrons in the whole energy range up to 25keV), high N concentrations are found in the deposits.

Bibliography

- [1] G. Charvin, J. F. Allemand, T. R. Strick, D. Bensimon, and V. Croquette. Twisting DNA: single molecule studies. *Contemporary Physics*, 45(5):383–403, 2004.
- [2] T. Strick, J. F. Allemand, V. Croquette, and D. Bensimon. Twisting and stretching single DNA molecules. *Progress in Biophysics & Molecular Biology*, 74(1-2):115–140, 2000.
- [3] T. Lionnet, S. Joubaud, R. Lavery, D. Bensimon, and V. Croquette. Wringing out DNA. *Physical Review Letters*, 96(17), 2006.
- [4] C. Bustamante, S. B. Smith, J. Liphardt, and D. Smith. Single-molecule studies of DNA mechanics. *Current Opinion in Structural Biology*, 10(3):279–285, 2000.
- [5] C. Bustamante, Z. Bryant, and S. B. Smith. Ten years of tension: single-molecule DNA mechanics. *Nature*, 421(6921):423–427, 2003.
- [6] J. F. Allemand, D. Bensimon, R. Lavery, and V. Croquette. Stretched and overwound DNA forms a Pauling-like structure with exposed bases. *Proceedings of the National Academy of Sciences of the United States of America*, 95(24):14152–14157, 1998.
- [7] T. R. Strick, J. F. Allemand, D. Bensimon, and V. Croquette. Stress-induced structural transitions in DNA and proteins. *Annual Review of Biophysics and Biomolecular Structure*, 29:523–543, 2000.
- [8] Z. Bryant, M. D. Stone, J. Gore, S. B. Smith, N. R. Cozzarelli, and C. Bustamante. Structural transitions and elasticity from torque measurements on DNA. *Nature*, 424(6946):338–341, 2003.
- [9] J. Gore, Z. Bryant, M. Nollmann, M. U. Le, N. R. Cozzarelli, and C. Bustamante. DNA overwinds when stretched. *Nature*, 442(7104):836–839, 2006.

- [10] T. R. Strick, J. F. Allemand, D. Bensimon, and V. Croquette. Behavior of supercoiled DNA. *Biophysical Journal*, 74(4):2016–2028, 1998.
- [11] T. R. Strick, D. Bensimon, and V. Croquette. Micro-mechanical measurement of the torsional modulus of DNA. *Genetica*, 106(1-2):57–62, 1999.
- [12] F. Ritort. Single-molecule experiments in biological physics: methods and applications. *Journal of Physics-Condensed Matter*, 18(32):R531–R583, 2006.
- [13] M. A. M. Gijs. Magnetic particle handling in lab-on-a-chip microsystems. In B. Azzerboni, G. Asti, L. Pareti, and M. Ghidini, editors, *Magnetic Nanostructures in Modern Technology: Spintronics, Magnetic MEMS and Recording*, NATO Science for Peace and Security Series B - Physics and Biophysics, pages 153–165. Springer, 2008.
- [14] BioNano-Switch EC Project. <http://www.bionano-switch.info>, 2006–10. [Online; accessed October 19th, 2010].
- [15] I. Utke, P. Hoffmann, and J. Melngailis. Gas-assisted focused electron beam and ion beam processing and fabrication. *Journal of vacuum science & technology*, 26(4):1197–1276, 2008.
- [16] W. F. van Dorp and C. W. Hagen. A critical literature review of focused electron beam induced deposition. *Journal of Applied Physics*, 104(8):081301, 2008.
- [17] S. J. Randolph, J. D. Fowlkes, and P. D. Rack. Focused, nanoscale electron-beam-induced deposition and etching. *Critical Reviews in Solid State and Materials Sciences*, 31(3):55–89, 2006.
- [18] I. Utke, T. Bret, D. Laub, Ph. Buffat, L. Scandella, and P. Hoffmann. Thermal effects during focused electron beam induced deposition of nanocomposite magnetic-cobalt-containing tips. *Microelectronic Engineering*, 73-74:553–558, 2004.
- [19] I. Utke, J. Michler, Ph. Gasser, C. Santschi, D. Laub, M. Cantoni, P.A. Buffat, C. Jiao, and P. Hoffmann. Cross section investigations of compositions and sub-structures of tips obtained by focused electron beam induced deposition. *Advanced Engineering Materials*, 7(5):323–331, 2005.

- [20] G. Boero, I. Utke, T. Bret, N. Quack, M. Todorova, S. Mouaziz, P. Kejik, J. Brugger, R. S. Popovic, and P. Hoffmann. Submicrometer Hall devices fabricated by focused electron-beam-induced deposition. *Applied Physics Letters*, 86(4):042503, 2005.
- [21] A. Botman, J. J. L. Mulders, and C. W. Hagen. Creating pure nanostructures from electron-beam-induced deposition using purification techniques: a technology perspective. *Nanotechnology*, 20(37):17, 2009.
- [22] R. L. Stewart. Insulating films formed under electron and ion bombardment. *Physical Review*, 45(7):0488–0490, 1934.
- [23] E. F. Burton, R. S. Sennett, and S. G. Ellis. Specimen changes due to electron bombardment in the electron microscope. *Nature*, 160(4069):565–567, 1947.
- [24] J. H. L. Watson. An effect of electron bombardment upon carbon black. *Journal of Applied Physics*, 18(2):153–161, 1947.
- [25] J. Hillier. On the investigation of specimen contamination in the electron microscope. *Journal of Applied Physics*, 19(3):226–230, 1948.
- [26] H. König. Die Rolle der Kohle bei elektronenmikroskopischen Abbildungen. *Naturwissenschaften*, 35(9):261–265, 1948.
- [27] J. H. L. Watson. Specimen contamination in electron microscopes. *Journal of Applied Physics*, 19(1):110–111, 1948.
- [28] A. Perentes and P. Hoffmann. Focused electron beam induced deposition of Si-based materials from SiO_xC_y to stoichiometric SiO₂: Chemical compositions, chemical-etch rates, and deep ultraviolet optical transmissions. *Chemical Vapor Deposition*, 13(4):176–184, 2007.
- [29] Nanotools Scanning Probes, Munich. <http://www.nano-tools.com>.
- [30] P. C. Hoyle, M. Ogasawara, J. R. A. Cleaver, and H. Ahmed. Electrical-resistance of electron-beam-induced deposits from tungsten hexacarbonyl. *Applied Physics Letters*, 62(23):3043–3045, 1993.
- [31] J. D. Barry, M. Ervin, J. Molstad, A. Wickenden, T. Brintlinger, P. Hoffman, and J. Melngailis. Electron beam induced deposition of low resistivity platinum from Pt(PF₃)₄. *Journal of Vacuum Science & Technology B*, 24(6):3165–3168, 2006.

- [32] I. Utke, P. Hoffmann, B. Dwir, K. Leifer, E. Kapon, and P. Doppelt. Focused electron beam induced deposition of gold. *Journal of Vacuum Science & Technology B*, 18(6):3168–3171, 2000.
- [33] G. Hochleitner, H. D. Wanzenboeck, and E. Bertagnolli. Electron beam induced deposition of iron nanostructures. *Journal of Vacuum Science & Technology B*, 26(3):939–944, 2008.
- [34] M. Shimojo, M. Takeguchi, K. Mitsuishi, M. Tanaka, and K. Furuya. Mechanisms of crystalline iron oxide formation in electron beam-induced deposition. *Japanese Journal of Applied Physics Part 1- Regular Papers Brief Communications & Review Papers*, 46(9B):6247–6249, 2007.
- [35] T. Lukasczyk, M. Schirmer, H. P. Steinruck, and H. Marbach. Electron-beam-induced deposition in ultrahigh vacuum: Lithographic fabrication of clean iron nanostructures. *Small*, 4(6):841–846, 2008.
- [36] A. Perentes, G. Sinicco, G. Boero, B. Dwir, and P. Hoffmann. Focused electron beam induced deposition of nickel. *Journal of Vacuum Science & Technology B*, 25(6):2228–2232, 2007.
- [37] Y. M. Lau, P. C. Chee, J. T. L. Thong, and V. Ng. Properties and applications of cobalt-based material produced by electron-beam-induced deposition. *Journal of Vacuum Science & Technology a-Vacuum Surfaces and Films*, 20(4):1295–1302, 2002.
- [38] I. Utke, F. Cicoira, G. Jaenchen, P. Hoffmann, L. Scandella, B. Dwir, E. Kapon, D. Laub, P. Buffat, N. Xanthopoulos, and H. J. Mathieu. Focused electron beam induced deposition of high resolution magnetic scanning probe tips. In P. Bernier, P. Ajayan, Y. Iwasa, and P. Nikolaev, editors, *Symposium on Making Functional Materials with Nanotubes held at the 2001 MRS Fall Meeting*, pages 307–312, Boston, Ma, 2001.
- [39] I. Utke, V. Friedli, J. Michler, T. Bret, X. Multone, and P. Hoffmann. Density determination of focused-electron-beam-induced deposits with simple cantilever-based method. *Applied Physics Letters*, 88(3):031906, 2006.
- [40] D. Drouin, A. R. Couture, D. Joly, X. Tastet, V. Aimez, and R. Gauvin. CASINO v2.42 - a fast and easy-to-use modeling tool for scanning electron microscopy and microanalysis users. *Scanning*, 29(3):92–101, 2007.

- [41] K. Kanaya and S. Okayama. Penetration and energy-loss theory of electrons in solid targets. *Journal of Physics D-Applied Physics*, 5(1):43, 1972.
- [42] L Reimer. *Scanning Electron Microscopy. Physics of Image Formation and Microanalysis*. Springer, 2nd edition, 1998.
- [43] D. Beaulieu, Y. Ding, Z. L. Wang, and W. J. Lackey. Influence of process variables on electron beam chemical vapor deposition of platinum. *Journal of Vacuum Science & Technology B*, 23(5):2151–2159, 2005.
- [44] I. Utke, V. Friedli, M. Purrucker, and J. Michler. Resolution in focused electron- and ion-beam induced processing. *Journal of Vacuum Science & Technology B*, 25(6):2219–2223, 2007.
- [45] L. van Kouwen, A. Botman, and C. W. Hagen. Focused electron-beam-induced deposition of 3 nm dots in a scanning electron microscope. *Nano Letters*, 9(5):2149–2152, 2009.
- [46] W. F. van Dorp, B. van Someren, C. W. Hagen, and P. Kruit. Approaching the resolution limit of nanometer-scale electron beam-induced deposition. *Nano Letters*, 5(7):1303–1307, 2005.
- [47] J. Goldstein, D.E. Newbury, D.C. Joy, C.E. Lyman, P. Echlin, E. Lifshin, L. Sawyer, and J.R. Michael. *Scanning Electron Microscopy and X-Ray Microanalysis*. Springer Science+Business Media, New York, 3rd edition, 2003.
- [48] L. Reimer, M. Kassens, and L. Wiese. Monte Carlo simulation program with a free configuration of specimen and detector geometries. *Mikrochimica Acta*, pages 485–492, 1996.
- [49] M. N. Baibich, J. M. Broto, A. Fert, F. N. Vandau, F. Petroff, P. Eitenne, G. Creuzet, A. Friederich, and J. Chazelas. Giant magnetoresistance of (001)Fe/(001) Cr magnetic superlattices. *Physical Review Letters*, 61(21):2472–2475, 1988.
- [50] G. Binasch, P. Grunberg, F. Saurenbach, and W. Zinn. Enhanced magnetoresistance in layered magnetic-structures with antiferromagnetic interlayer exchange. *Physical Review B*, 39(7):4828–4830, 1989.
- [51] G. A. West and K. W. Beeson. Chemical vapor-deposition of cobalt silicide. *Applied Physics Letters*, 53(9):740–742, 1988.

- [52] G. J. M. Dormans, G. J. B. M. Meekes, and E. G. J. Staring. OMCVD of cobalt and cobalt silicide. *Journal of Crystal Growth*, 114(3):364–372, 1991.
- [53] P. A. Lane, P. E. Oliver, P. J. Wright, C. L. Reeves, A. D. Pitt, and B. Cockayne. Metal organic CVD of cobalt thin films using cobalt tricarbonyl nitrosyl. *Chemical Vapor Deposition*, 4(5):183–+, 1998.
- [54] S. Gu, P. Atanasova, M. J. Hampden-Smith, and T. T. Kodas. Chemical vapor deposition of copper-cobalt binary films. *Thin Solid Films*, 340(1-2):45–52, 1999.
- [55] S. W. K. Choi and R. J. Puddephatt. Cobalt-palladium and cobalt-platinum bilayer films formed by chemical vapor deposition. *Chemistry of Materials*, 9(5):1191–1195, 1997.
- [56] P. Gilmont and A. A. Blanchard. Dicobalt octacarbonyl, cobalt nitrosyl tricarbonyl, and cobalt tetracarbonyl hydride. *Inorganic Syntheses*, 2:238–243, 1946.
- [57] I. Utke, P. Hoffmann, R. Berger, and L. Scandella. High-resolution magnetic Co supertips grown by a focused electron beam. *Applied Physics Letters*, 80(25):4792–4794, 2002.
- [58] A. Lapicki, K. Kang, and T. Suzuki. Fabrication of magnetic dot arrays by ion beam induced chemical vapor deposition (IBICVD). *IEEE Transactions on Magnetics*, 38(5):2589–2591, 2002.
- [59] A. Lapicki, E. Ahmad, and T. Suzuki. Ion beam induced chemical vapor deposition (IBICVD) of cobalt particles. *Journal of Magnetism and Magnetic Materials*, 240(1-3):47–49, 2002.
- [60] M. H. Ervin and B. M. Nichols. Electron beam induced deposition of cobalt for use as single- and multiwalled carbon nanotube growth catalyst. *Journal of Vacuum Science & Technology B*, 27(6):2982–2985, 2009.
- [61] I. Utke, V. Friedli, S. Fahlbusch, S. Hoffmann, P. Hoffmann, and J. Michler. Tensile strengths of metal-containing joints fabricated by focused electron beam induced deposition. *Advanced Engineering Materials*, 8(3):155–157, 2006.
- [62] A. Fernandez-Pacheco, J. M. De Teresa, R. Cordoba, and M. R. Ibarra. Magnetotransport properties of high-quality cobalt nanowires grown

- by focused-electron-beam-induced deposition. *Journal of Physics D-Applied Physics*, 42(5), 2009.
- [63] A. Fernandez-Pacheco, J. M. De Teresa, R. Cordoba, M. R. Ibarra, D. Petit, D. E. Read, L. O'Brien, E. R. Lewis, H. T. Zeng, and R. P. Cowburn. Domain wall conduit behavior in cobalt nanowires grown by focused electron beam induced deposition. *Applied Physics Letters*, 94(19), 2009.
- [64] A. Fernandez-Pacheco, J. M. De Teresa, A. Szkudlarek, R. Cordoba, M. R. Ibarra, D. Petit, L. O'Brien, H. T. Zeng, E. R. Lewis, D. E. Read, and R. P. Cowburn. Magnetization reversal in individual cobalt micro- and nanowires grown by focused-electron-beam-induced-deposition. *Nanotechnology*, 20(47):9, 2009.
- [65] R. Cordoba, J. Sese, J. M. De Teresa, and M. R. Ibarra. High-purity cobalt nanostructures grown by focused-electron-beam-induced deposition at low current. *Microelectronic Engineering*, 87(5-8):1550–1553, 2010.
- [66] N. Silvis-Cividjian, C. W. Hagen, P. Kruit, M. A. J. Van der Stam, and H. B. Groen. Direct fabrication of nanowires in an electron microscope. *Applied Physics Letters*, 82(20):3514–3516, 2003.
- [67] N. Silvis-Cividjian and C. W. Hagen. *Electron-beam-induced nanometer-scale deposition*. Advances in Imaging and Electron Physics, Vol 143. Elsevier Academic Press, 2006.
- [68] N. Silvis-Cividjian, C. W. Hagen, L. H. A. Leunissen, and P. Kruit. The role of secondary electrons in electron-beam-induced-deposition spatial resolution. *Microelectronic Engineering*, 61-2:693–699, 2002.
- [69] N. Silvis-Cividjian, C. W. Hagen, and P. Kruit. Spatial resolution limits in electron-beam-induced deposition. *Journal of Applied Physics*, 98(8):12, 2005.
- [70] C. W. Hagen, N. Silvis-Cividjian, and P. Kruit. Resolution limit for electron beam-induced deposition on thick substrates. *Scanning*, 28(4):204–211, 2006.
- [71] J. D. Fowlkes and P. D. Rack. Fundamental electron-precursor-solid interactions derived from time-dependent electron-beam-induced deposition simulations and experiments. *ACS Nano*, 4(3):1619–1629, 2010.

- [72] R. W. Christy. Formation of thin polymer films by electron bombardment. *Journal of Applied Physics*, 31(9):1680–1683, 1960.
- [73] K. H. Müller. Speed-controlled electron-microrecorder 1. *Optik*, 33(3):296–311, 1971.
- [74] V. Scheuer, H. Koops, and T. Tschudi. Electron beam decomposition of carbonyls on silicon. *Microelectronic Engineering*, 5(1-4):423–430, 1986.
- [75] T. E. Allen, R. R. Kunz, and T. M. Mayer. Monte-Carlo calculation of low-energy electron-emission from surfaces. *Journal of Vacuum Science & Technology B*, 6(6):2057–2060, 1988.
- [76] D. Kunze, O. Peters, and Sauerbre.G. Polymerisation adsorbierter Kohlenwasserstoffe bei Elektronenbeschuss. *Zeitschrift für angewandte Physik*, 22(2):69, 1967.
- [77] C. Santschi, M. Jenke, P. Hoffmann, and J. Brugger. Interdigitated 50 nm Ti electrode arrays fabricated using XeF₂ enhanced focused ion beam etching. *Nanotechnology*, 17(11):2722–2729, 2006.
- [78] M. A. M. Gijs. Magnetic bead handling on-chip: new opportunities for analytical applications. *Microfluidics and Nanofluidics*, 1(1):22–40, 2004.
- [79] C. R. Tamanaha, S. P. Mulvaney, J. C. Rife, and L. J. Whitman. Magnetic labeling, detection, and system integration. *Biosensors & Bioelectronics*, 24(1):1–13, 2008.
- [80] M. Megens and M. Prins. Magnetic biochips: a new option for sensitive diagnostics. *Journal of Magnetism and Magnetic Materials*, 293(1):702–708, 2005.
- [81] W. F. Brown. Thermal fluctuations of a single-domain particle. *Physical Review*, 130(5):1677, 1963.
- [82] L. Néel. Théorie du traînage magnétique des ferromagnétiques en grains fins avec applications aux terres cuites. *Ann. Geophys.*, 5:99–136, 1949.
- [83] G. Fonnum, C. Johansson, A. Molteberg, S. Morup, and E. Aksnes. Characterisation of Dynabeads (R) by magnetization measurements and Mossbauer spectroscopy. *Journal of Magnetism and Magnetic Materials*, 293(1):41–47, 2005.

- [84] C. P. Bean and J. D. Livingston. Superparamagnetism. *Journal of Applied Physics*, 30(4):S120–S129, 1959.
- [85] G. Mihajlovic, K. Aledealat, P. Xiong, S. Von Molnar, M. Field, and G. J. Sullivan. Magnetic characterization of a single superparamagnetic bead by phase-sensitive micro-Hall magnetometry. *Applied Physics Letters*, 91, 2007.
- [86] S. Chikazumi and S. H. Charap. *Physics of magnetism*. Wiley series on the science and technology of materials. Wiley, 1966.
- [87] L. Ejsing, M. F. Hansen, A. K. Menon, H. A. Ferreira, D. L. Graham, and P. P. Freitas. Planar Hall effect sensor for magnetic micro- and nanobead detection. *Applied Physics Letters*, 84(23):4729–4731, 2004.
- [88] E. H. Hall. On a new action of the magnet on electric currents. *American Journal of Mathematics*, 2(3):287–292, 1879.
- [89] G. Boero, M. Demierre, P. A. Besse, and R. S. Popovic. Micro-Hall devices: performance, technologies and applications. *Sensors and Actuators a-Physical*, 106(1-3):314–320, 2003.
- [90] L. Berger and G. Bergmann. The Hall effect of ferromagnets. In Chia Ling Chien and C.R. Westgate, editors, *The Hall effect and its applications*. Plenum Press, 1980.
- [91] A. Fert and D. Lottis. Magnetotransport phenomena. In Jan Evetts, Robert W. Cahn, and Michael B. Bever, editors, *Concise encyclopedia of magnetic & superconducting materials*. Pergamon Press, 1992.
- [92] A. Gerber, A. Milner, M. Karpovsky, B. Lemke, H. U. Habermeier, J. Tuaillon-Combes, M. Négrier, O. Boisron, P. Mélinon, and A. Perez. Extraordinary Hall effect in magnetic films. *Journal of Magnetism and Magnetic Materials*, 242-245(Part 1):90–97, 2002.
- [93] R. C. O’Handley. *Modern magnetic materials*. John Wiley, 2000.
- [94] E. M. Pugh. Hall effect and magnetic induction in a bar of electrolytic iron. *Physical Review*, 32(5):0824–0828, 1928.
- [95] R. Karplus and J. M. Luttinger. Hall effect in ferromagnetics. *Physical Review*, 95(5):1154, 1954.
- [96] C.M. Hurd. *The Hall Effect in Metals and Alloys*. The international cryogenics monograph series. Plenum Press, New York - London, 1972.

- [97] M. Gabureac, L. Bernau, I. Utke, and G. Boero. Granular Co-C nano-Hall sensors by focused-beam-induced deposition. *Nanotechnology*, 21(11):115503, 2010.
- [98] D. K. Wood, K. K. Ni, D. R. Schmidt, and A. N. Cleland. Submicron giant magnetoresistive sensors for biological applications. *Sensors and Actuators a-Physical*, 120(1):1–6, 2005.
- [99] H. A. Ferreira, D. L. Graham, P. P. Freitas, and J. M. S. Cabral. Biodetection using magnetically labeled biomolecules and arrays of spin valve sensors. *Journal of Applied Physics*, 93(10):7281–7286, 2003.
- [100] L. Ejsing, M. F. Hansen, A. K. Menon, H. A. Ferreira, D. L. Graham, and P. P. Freitas. Magnetic microbead detection using the planar Hall effect. *Journal of Magnetism and Magnetic Materials*, 293(1):677–684, 2005.
- [101] W. F. Shen, X. Y. Liu, D. Mazumdar, and G. Xiao. In situ detection of single micron-sized magnetic beads using magnetic tunnel junction sensors. *Applied Physics Letters*, 86(25), 2005.
- [102] F. A. Cardoso, J. Germano, R. Ferreira, S. Cardoso, V. C. Martins, P. P. Freitas, M. S. Piedade, and L. Sousa. Detection of 130 nm magnetic particles by a portable electronic platform using spin valve and magnetic tunnel junction sensors. *Journal of Applied Physics*, 103(7):3, 2008.
- [103] M. Bando, T. Ohashi, M. Dede, R. Akram, A. Oral, S. Y. Park, I. Shibasaki, H. Handa, and A. Sandhu. High sensitivity and multi-functional micro-hall sensors fabricated using InAlSb/InAsSb/InAlSb heterostructures. *Journal of Applied Physics*, 105(7):07E909, 2009.
- [104] P. Kejik, G. Boero, M. Demierre, and R. S. Popovic. An integrated micro-Hall probe for scanning magnetic microscopy. *Sensors and Actuators a-Physical*, 129(1-2):212–215, 2006.
- [105] P. A. Besse, G. Boero, M. Demierre, V. Pott, and R. Popovic. Detection of a single magnetic microbead using a miniaturized silicon Hall sensor. *Applied Physics Letters*, 80(22):4199–4201, 2002.
- [106] S. Mouaziz, C. Imboden, C. Santschi, O. Vazquez Mena, R. Popovic, J. Brugger, and G. Boero. Integrated nickel micro-nano-Hall sensors on SU-8 cantilevers for scanning Hall probe microscopy. In *Digest of*

- Technical Papers*, pages 2589–2592, Lyon, France, 2007. Transducers 07.
- [107] K. Togawa, H. Sanbonsugi, A. Lapicki, M. Abe, H. Handa, and A. Sandhu. High-sensitivity InSb thin-film micro-Hall sensor arrays for simultaneous multiple detection of magnetic beads for biomedical applications. *IEEE Transactions on Magnetism*, 41(10):3661–3663, 2005.
- [108] A. Candini, G. C. Gazzadi, A. Di Bona, M. Affronte, D. Ercolani, G. Biasiol, and L. Sorba. Hall nano-probes fabricated by focused ion beam. *Nanotechnology*, 17(9):2105–2109, 2006.
- [109] A. Candini, G. C. Gazzadi, A. di Bona, M. Affronte, D. Ercolani, G. Biasiol, and L. Sorba. Focused ion beam patterned Hall nano-sensors. *Journal of Magnetism and Magnetic Materials*, 310(2):2752–2754, 2007.
- [110] A. Sandhu, H. Sanbonsugi, I. Shibusaki, M. Abe, and H. Handa. High sensitivity InSb ultra-thin film micro-Hall sensors for bioscreening applications. *Japanese Journal of Applied Physics Part 2-Letters & Express Letters*, 43(7A):L868–L870, 2004.
- [111] O. Kazakova, J. C. Gallop, P. See, D. Cox, G. K. Perkins, J. D. Moore, and L. F. Cohen. Detection of a micron-sized magnetic particle using InSb Hall sensor. *IEEE Transactions on Magnetism*, 45(10):4499–4502, 2009.
- [112] L. Ejsing, M.F. Hansen, and A.K. Menon. Planar Hall effect magnetic sensor for micro-bead detection. In *17th European Conference on Solid-State Transducers*. Eurosensors 2003, 2003.
- [113] Z. Z. Zhang, Y. W. Liu, Y. P. Yang, and Q. Y. Jin. Micromagnetic simulation for nanobeads detection using planar Hall sensors. *IEEE Transactions on Magnetism*, 41(10):3625–3627, 2005.
- [114] D. T. Bui, Q. H. Tran, T. T. Nguyen, M. D. Tran, H. D. Nguyen, and C. Kim. Planar Hall bead array counter microchip with NiFe/IrMn bilayers. *Journal of Applied Physics*, 104(7):4, 2008.
- [115] P. P. Freitas, F. Silva, N. J. Oliveira, L. V. Melo, L. Costa, and N. Almeida. Spin valve sensors. *Sensors and Actuators a-Physical*, 81(1-3):2–8, 2000.

- [116] D. L. Graham, H. Ferreira, J. Bernardo, P. P. Freitas, and J. M. S. Cabral. Single magnetic microsphere placement and detection on-chip using current line designs with integrated spin valve sensors: Biotechnological applications. *Journal of Applied Physics*, 91(10):7786–7788, 2002.
- [117] G. X. Li, V. Joshi, R. L. White, S. X. Wang, J. T. Kemp, C. Webb, R. W. Davis, and S. H. Sun. Detection of single micron-sized magnetic bead and magnetic nanoparticles using spin valve sensors for biological applications. *Journal of Applied Physics*, 93(10):7557–7559, 2003.
- [118] L. W. Y. Lui, Y. Y. Tan, K. B. Li, C. H. Sow, and S. J. O’Shea. Detection of ferromagnetic particles using spin valve sensors. *Journal of Applied Physics*, 100(4):6, 2006.
- [119] J. W. Roh, O. T. Son, Y. T. Lee, K. I. Lee, H. I. Jung, and W. Lee. Highly sensitive spin-valve devices for chip-cytometers. *Physica Status Solidi a-Applications and Materials Science*, 206(7):1636–1640, 2009.
- [120] D. L. Graham, H. A. Ferreira, N. Feliciano, P. P. Freitas, L. A. Clarke, and M. D. Amaral. Magnetic field-assisted DNA hybridisation and simultaneous detection using micron-sized spin-valve sensors and magnetic nanoparticles. *Sensors and Actuators B-Chemical*, 107(2):936–944, 2005.
- [121] H. A. Ferreira, N. Feliciano, D. L. Graham, L. A. Clarke, M. D. Amaral, and P. P. Freitas. Rapid DNA hybridization based on ac field focusing of magnetically labeled target DNA. *Applied Physics Letters*, 87(1), 2005.
- [122] H. A. Ferreira, F. A. Cardoso, R. Ferreira, S. Cardoso, and P. P. Freitas. Magnetoresistive DNA chips based on ac field focusing of magnetic labels. *Journal of Applied Physics*, 99(8):3, 2006.
- [123] X. J. A. Janssen, L. J. van Ijzendoorn, and M. W. Prins. On-chip manipulation and detection of magnetic particles for functional biosensors. *Biosensors & Bioelectronics*, 23(6):833–838, 2008.
- [124] B. M. de Boer, J. A. H. M. Kahlman, T. P. G. H. Jansen, H. Duric, and J. Veen. An integrated and sensitive detection platform for magnetoresistive biosensors. *Biosensors and Bioelectronics*, 22(9-10):2366–2370, 2007.

- [125] M. Julliere. Tunneling between ferromagnetic films. *Physics Letters A*, 54(3):225–226, 1975.
- [126] C. Albon, A. Weddemann, A. Auge, K. Rott, and A. Hutten. Tunneling magnetoresistance sensors for high resoluteive particle detection. *Applied Physics Letters*, 95(2):3, 2009.
- [127] T. Bret, I. Utke, A. Bachmann, and P. Hoffmann. In situ control of the focused-electron-beam-induced deposition process. *Applied Physics Letters*, 83(19):4005–4007, 2003.
- [128] S. Babin, M. Gaevski, D. Joy, M. Machin, and A. Martynov. Technique to automatically measure electron-beam diameter and astigmatism: BEAMETR. *Journal of Vacuum Science & Technology B*, 24(6):2956–2959, 2006.
- [129] V. Friedli and I. Utke. Optimized molecule supply from nozzle-based gas injection systems for focused electron- and ion-beam induced deposition and etching: simulation and experiment. *Journal of Physics D-Applied Physics*, 42(12):125305, 2009.
- [130] I. Horcas, R. Fernandez, J. M. Gomez-Rodriguez, J. Colchero, J. Gomez-Herrero, and A. M. Baro. WSXM: A software for scanning probe microscopy and a tool for nanotechnology. *Review of Scientific Instruments*, 78(1):013705–8, 2007.
- [131] H. Hiroshima, N. Suzuki, N. Ogawa, and M. Komuro. Conditions for fabrication of highly conductive wires by electron-beam-induced deposition. *Japanese Journal of Applied Physics*, 38(12B):7135–7139, 1999.
- [132] R. C. Che, M. Takeguchi, M. Shimojo, W. Zhang, and K. Furuya. Fabrication and electron holography characterization of FePt alloy nanorods. *Applied Physics Letters*, 87(22), 2005.
- [133] K. Jousten, editor. *Handbook of Vacuum Technology*. Wiley-VCH, 2008.
- [134] L. Bernau, M. Gabureac, R. Erni, and I. Utke. Tunable nanosynthesis of composite materials by electron-impact reaction. *Angewandte Chemie, International Edition*, 49(47):8880–8884, 2010.
- [135] C. J. Lobo, M. Toth, R. Wagner, B. L. Thiel, and M. Lysaght. High resolution radially symmetric nanostructures from simultaneous electron beam induced etching and deposition. *Nanotechnology*, 19(2), 2008.

- [136] M. Toth, C. J. Lobo, G. Hartigan, and W. R. Knowles. Electron flux controlled switching between electron beam induced etching and deposition. *Journal of Applied Physics*, 101(5), 2007.
- [137] H. Miyazoe, I. Utke, J. Michler, and K. Terashima. Controlled focused electron beam-induced etching for the fabrication of sub-beam-size nanoholes. *Applied Physics Letters*, 92(4), 2008.
- [138] R. Dobrozemsky, S. Menhart, and K. Buchtela. Residence times of water molecules on stainless steel and aluminum surfaces in vacuum and atmosphere. *Journal of Vacuum Science & Technology A*, 25(3):551–556, 2007.
- [139] T. Bret, S. Mauron, I. Utke, and P. Hoffmann. Characterization of focused electron beam induced carbon deposits from organic precursors. *Microelectronic Engineering*, 78-79:300–306, 2005.
- [140] T. Bret. *Physico-chemical study of the focused electron beam induced deposition process*. PhD Thesis, EPFL, 2005.
- [141] I. Utke, M. Purrucker, V. Friedli, and J. Michler. Shape simulation in focused electron beam (FEB) induced deposition. Micro- and Nano-Engineering conference (MNE), poster contribution, 2007.
- [142] I. W. Park, M. Yoon, Y. M. Kim, Y. Kim, H. Yoon, H. J. Song, V. Volkov, A. Avilov, and Y. J. Park. Magnetic properties and microstructure of cobalt nanoparticles in a polymer film. *Solid State Communications*, 126(7):385–389, 2003.
- [143] F. Porrati, R. Sachser, and M. Huth. The transient electrical conductivity of W-based electron-beam-induced deposits during growth, irradiation and exposure to air. *Nanotechnology*, 20(19), 2009.
- [144] A. B. Pakhomov, X. Yan, and B. Zhao. Giant Hall-effect in percolating ferromagnetic granular metal-insulator films. *Applied Physics Letters*, 67(23):3497–3499, 1995.
- [145] K. Togawa, H. Sanbonsugi, A. Sandhu, M. Abe, H. Narimatsu, K. Nishio, and H. Handa. Detection of magnetically labeled DNA using pseudomorphic AlGaAs/InGaAs/GaAs heterostructure micro-Hall biosensors. *Journal of Applied Physics*, 99(8):08P103, 2006.
- [146] P. P. Freitas, R. Ferreira, S. Cardoso, and F. Cardoso. Magnetoresistive sensors. *Journal of Physics-Condensed Matter*, 19(16):21, 2007.

- [147] V. N. Matveev, V. I. Levashov, V. T. Volkov, O. V. Kononenko, A. V. Chernyh, M. A. Knjazev, and V. A. Tulin. Fabrication and use of a nanoscale Hall probe for measurements of the magnetic field induced by MFM tips. *Nanotechnology*, 19(47), 2008.
- [148] O. Kazakova, V. Panchal, J. Gallop, P. See, D. C. Cox, M. Spasova, and L. F. Cohen. Ultrasmall particle detection using a submicron Hall sensor. *Journal of Applied Physics*, 107(9):09E708, 2010.
- [149] H.P.R. Frederikse. Properties of magnetic materials. In David R. Lide, editor, *CRC Handbook of Chemistry and Physics*. Taylor and Francis, 91st edition, 2010.
- [150] A. Millan, A. Urtizberea, N. J. O. Silva, F. Palacio, V. S. Amaral, E. Snoeck, and V. Serin. Surface effects in maghemite nanoparticles. *Journal of Magnetism and Magnetic Materials*, 312(1):L5–L9, 2007.
- [151] M.S. Gabureac, L. Bernau, I. Utke, A. Fernandez-Pacheco, and J.M. De Teresa. Focused ion and electron beam induced deposition of magnetic nanostructures. In P.E. Russell S. Moshkalev, I. Utke, editor, *Nanofabrication Using Focused Ion and Electron Beams: Principles and Applications*. Oxford University Press, 2011.
- [152] A. Gerber, A. Milner, A. Finkler, M. Karpovski, L. Goldsmith, J. Tuaillon-Combes, O. Boisron, P. Melinon, and A. Perez. Correlation between the extraordinary Hall effect and resistivity. *Physical Review B*, 69(22), 2004.
- [153] G. Mihajlovic, P. Xiong, S. von Molnar, K. Ohtani, H. Ohno, M. Field, and G. J. Sullivan. Detection of single magnetic bead for biological applications using an InAs quantum-well micro-Hall sensor. *Applied Physics Letters*, 87(11):3, 2005.
- [154] A. Pross, A. I. Crisan, S. J. Bending, V. Mosser, and M. Konczykowski. Second-generation quantum-well sensors for room-temperature scanning Hall probe microscopy. *Journal of Applied Physics*, 97(9):096105, 2005.
- [155] A. Sandhu, K. Kurosawa, M. Dede, and A. Oral. 50nm Hall sensors for room temperature scanning Hall probe microscopy. *Japanese Journal of Applied Physics*, 43(2):777–778, 2004.
- [156] C. Dolabdjian, A. Qasimi, D. Bloyet, and V. Mosser. Spatial resolution of SQUID magnetometers and comparison with low noise room

- temperature magnetic sensors. *Physica C-Superconductivity and Its Applications*, 368(1-4):80–84, 2002.
- [157] D. R. Baselt, G. U. Lee, M. Natesan, S. W. Metzger, P. E. Sheehan, and R. J. Colton. A biosensor based on magnetoresistance technology. *Biosensors & Bioelectronics*, 13(7-8):731–739, 1998.
- [158] R. Seidel and C. Dekker. Single-molecule studies of nucleic acid motors. *Current Opinion in Structural Biology*, 17(1):80–86, 2007.
- [159] EG&G Instruments Corp. Model 7260 DSP Lock-in Amplifier Instruction Manual, 1998.
- [160] R. Wirix-Speetjens, W. Fyen, J. De Boeck, and G. Borghs. Single magnetic particle detection: Experimental verification of simulated behavior. *Journal of Applied Physics*, 99(10):4, 2006.
- [161] M. Megens, F. de Theije, B. de Boer, and F. van Gaal. Scanning probe measurements on a magnetic bead biosensor. *Journal of Applied Physics*, 102(1), 2007.
- [162] R. Sultan, A. D. Avery, G. Stiehl, and B. L. Zink. Thermal conductivity of micromachined low-stress silicon-nitride beams from 77 to 325 K. *Journal of Applied Physics*, 105(4), 2009.
- [163] B. L. Zink and F. Hellman. Specific heat and thermal conductivity of low-stress amorphous Si-N membranes. *Solid State Communications*, 129(3):199–204, 2004.
- [164] S. Wang, Y. M. Sun, Q. Wang, and J. M. White. Electron-beam induced initial growth of platinum films using Pt(PF₃)₄. *Journal of Vacuum Science & Technology B*, 22(4):1803–1806, 2004.
- [165] A. Botman, C. W. Hagen, J. Li, B. L. Thiel, K. A. Dunn, J. J. L. Mulders, S. Randolph, and M. Toth. Electron postgrowth irradiation of platinum-containing nanostructures grown by electron-beam-induced deposition from Pt(PF₃)₄. *Journal of Vacuum Science & Technology B*, 27(6):2759–2763, 2009.
- [166] C. L. Hammill, R. J. Clark, C. W. Ross, A. G. Marshall, and J. Schmutz. Synthesis and characterization of the platinum cluster complex Pt₄(PF₃)₈. *Inorganic Chemistry*, 36(26):5973–5977, 1997.

- [167] X. L. Zhou and J.M. White. A comparative study of PF₃, PH₃ and P(CH₃)₃ on clean, k-covered, and Cl-covered Ag (111). *Surface Science*, 221(3):534, 1989.
- [168] R. Zhang and P.B. Comita. Deposition of platinum from Pt(PF₃)₄ on atomically clean platinum surfaces. *Chemical Physics Letters*, 200(3):297, 1992.
- [169] Y. Zhou, G. E. Mitchell, M. A. Henderson, and J. M. White. Comparative-study of PF₃ chemisorbed on Ru(001), Cu/Ru(001), and Pt(111). *Surface Science*, 214(1-2):209–226, 1989.
- [170] Th. Kruck and K. Baur. Über Trifluorosphinkomplexe von Palladium(0) und Platin(0). *Zeitschrift für anorganische und allgemeine Chemie*, 364(3-4):192–208, 1969.
- [171] S. A. Joyce, A. L. Johnson, and T. E. Madey. Methodology for electron-stimulated desorption ion angular-distributions of negative-ions. *Journal of Vacuum Science & Technology a-Vacuum Surfaces and Films*, 7(3):2221–2226, 1989.
- [172] K. A. G. Macneil and J. C. J. Thynne. Negative ion formation by boron trifluoride and phosphorus trifluoride. *Journal of Physical Chemistry*, 74(11):2257, 1970.
- [173] H. S. Tao, U. Diebold, N. D. Shinn, and T. E. Madey. Surface chemistry of PH₃, PF₃ and PCl₃ on Ru(0001). *Surface Science*, 312(3):323–344, 1994.
- [174] C. L. Lugez, K. K. Irikura, and M. E. Jacox. Experimental and ab initio study of the infrared spectra of ionic species derived from PF₅, PF₃, and F₃PO and trapped in solid neon. *Journal of Chemical Physics*, 108(20):8381–8393, 1998.
- [175] J. L. Roustan, Y. Lijour, and B. A. Morrow. Time-resolved FTIR study of the adsorption and reaction of Co(CO)₃NO on alumina. *Inorganic Chemistry*, 26(15):2509–2516, 1987.
- [176] A. R. Ivanova, G. Nuesca, X. M. Chen, C. Goldberg, A. E. Kaloyeros, B. Arkles, and J. J. Sullivan. The effects of processing parameters in the chemical vapor deposition of cobalt from cobalt tricarbonyl nitrosyl. *Journal of the Electrochemical Society*, 146(6):2139–2145, 1999.

- [177] R. S. McDowell, J. T. Yates, and W. D. Horrocks. Infrared spectrum of $\text{Co}(\text{CO})_3\text{NO}$. *Journal of Chemical Physics*, 34(2):530, 1961.
- [178] B. A. Morrow, M. I. Baraton, Y. Lijour, and J. L. Roustan. An FT-I.R. study of the deposition of $\text{Co}(\text{CO})_3\text{NO}$ on Zeolite-Y - influence of the support on the formation of isocyanates. *Spectrochimica Acta Part a-Molecular and Biomolecular Spectroscopy*, 43(12):1583–1587, 1987.
- [179] J. Opitz. Electron impact ionization of cobalt-tricarbonyl-nitrosyl, cyclopentadienyl-cobalt-dicarbonyl and biscyclopentadienyl-cobalt: appearance energies, bond energies and enthalpies of formation. *International Journal of Mass Spectrometry*, 225(2):115–126, 2003.
- [180] B. Sztaray and T. Baer. Consecutive and parallel dissociation of energy-selected $\text{Co}(\text{CO})_3\text{NO}^+$ ions. *Journal of Physical Chemistry A*, 106(35):8046–8053, 2002.

Nomenclature

Abbreviations

AFM	Atomic force microscope
AMR	Anisotropic magnetoresistance
BNC	Bayonet Neill-Concelman connector
BSE	Backscattered electron
CMOS	Complementary metal oxide semiconductor
CNT	Carbon nanotubes
COST	European cooperation in science and technology
CVD	Chemical vapor deposition
DNA	Deoxyribonucleic acid
EBL	Electron beam lithography
EDX	Energy-dispersive X-ray spectroscopy
EHE	Extraordinary Hall effect
ESD	Electrostatic discharge
FEB	Focused electron beam
FEBID	Focused electron beam induced deposition
FEG	Field emission gun
FEM	Finite element method
FIB	Focused ion beam
FIBID	Focused ion beam induced deposition
FSE	Forward scattered electron
FWHM	Full width at half maximum
GHE	Giant Hall effect
GIS	Gas injection system
GMR	Giant magnetoresistance
HREELS	High resolution electron energy loss spectroscopy
HV	High vacuum
IBICVD	Ion beam induced chemical vapor deposition
LCC	Leadless chip carrier
MFM	Magnetic force microscope

MC	Monte Carlo
ML	Monolayer
MTJ	Magnetic tunnel junction
OHE	Ordinary Hall effect
PCB	Printed circuit board
PE	Primary electron
PHE	Planar Hall effect
PMMA	Poly(methyl methacrylate)
PVD	Physical vapor deposition
RGA	Residual gas analyzer
SE	Secondary electron
SEM	Scanning electron microscope
STEM	Scanning transmission electron microscope
TEM	Transmission electron microscope
TMR	Tunnel magnetoresistance
TPD	Temperature programmed desorption
UHV	Ultrahigh vacuum
VSM	Vibrating sample magnetometer
XPS	X-ray photoelectron spectroscopy

Constants

e	Elementary charge: $e = 1.602 \times 10^{-19}$ C
h	Planck constant: $h = 6.626 \times 10^{-34}$ J s
k_B	Boltzmann constant: $k_B = 1.381 \times 10^{-23}$ J K ⁻¹
μ_0	magnetic permeability of vacuum: $\mu_0 = 4\pi \times 10^{-7}$ V s A ⁻¹ m ⁻¹
μ_B	Bohr magneton: $\mu_B = 9.274 \times 10^{-24}$ J T ⁻¹
ϕ_0	Flux quantum $\phi_0 = 2.07 \times 10^{-15}$ T m ²
N_A	Avogadro constant: $N_A = 6.022 \times 10^{23}$ mol ⁻¹
R	Ideal gas constant: $R = 8.314$ J mol ⁻¹ K ⁻¹

List of publications

Book chapter

- M. Gabureac, L. Bernau, I. Utke, A. Fernandez-Pacheco and J. M. De Teresa, Focused Ion and Electron beam induced deposition of magnetic nanostructures. In *Nanofabrication Using Focused Ion and Electron Beams: Principles and Applications* edited by S. Moshkalev, I. Utke and P. E. Russell, in press - Oxford University Press, Oxford, 2011.

Journal articles

- K. Landheer, H. Fairbrother, L. Bernau, P. Swiderek et al., Electron Stimulated Surface Reactions and Decomposition of Tetrakis(trifluorophosphine)platinum ($\text{Pt}(\text{PF}_3)_4$), *manuscript in preparation*, 2011.
- M. Gabureac, L. Bernau, G. Boero and I. Utke, Spatially-resolved single paramagnetic bead detection, *manuscript in preparation*, 2011.
- L. Bernau, M. Gabureac, R. Erni and I. Utke, Tunable Nanosynthesis of Composite Materials by Electron-Impact Reaction. *Angewandte Chemie, International Edition* 49(47): 8880-8884, 2010.
- I. Utke, M. Gabureac, V. Friedli, L. Bernau, J. Michler, In-situ monitoring of gas-assisted focused ion beam and focused electron beam induced processing. *Journal of Physics: Conference Series* 241(1): 012072, 2010.
- M. Gabureac, L. Bernau, I. Utke and G. Boero, Granular Co-C nano-Hall sensors by focused-beam-induced deposition. *Nanotechnology* 21(11): 115503, 2010.
- S. Vaucher, L. Bernau, M. Stir, K. Ishizaki, J.M. Catala-Civera and R. Nicula, Microwave-induced electromigration in multicomponent metal-

lic alloys. *IEEE Microwave Symposium Digest (MTT)*: 1440-1443, 2010.

Conference contributions

- L. Bernau, M. Gabureac, I. Utke, Electron-impact dissociation of $\text{Co}_2(\text{CO})_8$: Direct nano-scale patterning of high-sensitivity magnetic material using focused electrons beams. *Gordon Research Conference on Radiation Chemistry*, Andover NH, USA, July 18-23, 2010. (Talk)
- L. Bernau, M.N. Hedhili, I. Utke, P. Swiderek, Electron-impact dissociation of surface-adsorbed $\text{Pt}(\text{PF}_3)_4$: a HREELS study. *Gordon Research Conference on Radiation Chemistry*, Andover NH, USA, July 18-23, 2010. (Poster)
- L. Bernau, M. Gabureac, I. Utke, Controlled tuning of the Co:C ratio in planar deposits obtained from $\text{Co}_2(\text{CO})_8$ assisted FEBID. *FEBIP Workshop 2010*, Albany NY, USA, July 15-16, 2010. (Talk)
- L. Bernau, M.N. Hedhili, I. Utke, P. Swiderek, HREELS study of the electron-induced dissociation of $\text{Pt}(\text{PF}_3)_4$, *FEBIP Workshop 2010*, Albany NY, USA, July 15-16, 2010. (Poster)
- L. Bernau, M. Gabureac, I. Utke, O. Kazakova, G. Boero, J. Michler, Focused Electron Beam induced deposition of Cobalt Hall Sensors as a tool to monitor DNA-elongation. *NanoEurope 2008*, St. Gallen, Switzerland, September 16-17, 2008. (Poster)

Curriculum vitae

Personal data

Name: Laurent BERNAU
Date of Birth: 11.10.1981
Place of Birth: St. Aubin NE
Nationalities: Austrian, French

Professional experience

2006-2010 PhD project at the Laboratory for Mechanics of Materials and Nanostructures, Swiss Federal Laboratories for Materials Testing and Research (EMPA), Thun
2002-2006 Back office at Scout Windrösli, Berne (25% part-time)
2003 Internship at Haag-Streit AG, Köniz (1 month)
2002-2003 Freelance software development for Staar Surgical AG, Biel
2000-2001 Internship at Swisscom AG, Berne (9 months)
1999 Internship at Concept 1, Inc., Daytona Beach FL (1 month)

Education

2007- Bachelor of Law, Universitäre Fernstudien Schweiz
2006-2011 PhD in Materials Science & Engineering, Ecole polytechnique fédérale de Lausanne (EPFL), Lausanne
2001-2006 Master of Science in Microengineering, specialization Micro- and Nanosystems, Ecole polytechnique fédérale de Lausanne (EPFL), Lausanne
1993-2000 Matura Typus A (latin/greek), Gymnasium Köniz, Köniz